Thesis for a Ph. D. Degree

Evolution of the Planetary Waves and Polar Vortex Breakup in the Stratosphere

성층권에서의 행성파의 변화와 극와동의 붕괴

August 2022

School of Earth and Environmental Sciences
Graduate School
Seoul National University

Jihoon Seo

Evolution of the Planetary Waves and Polar Vortex Breakup in the Stratosphere

성층권에서의 행성파의 변화와 극와동의 붕괴

지도 교수 최 우 갑

이 논문을 이학박사 학위논문으로 제출함
2022년 7월

서울대학교 대학원
지구환경과학부
서 지 훈

서지훈의 이학박사 학위논문을 인준함
2022년 7월

위 원 장 ______________________ (인)

부위원장 ______________________ (인)

위 원 ______________________ (인)

위 원 ______________________ (인)

위 원 ______________________ (인)

Evolution of the Planetary Waves and Polar Vortex Breakup in the Stratosphere

By
Jihoon Seo

A Dissertation Submitted to the Faculty of the Graduate School of the Seoul National University in Partial Fulfillment of the Requirements for the Degree of Doctor of Philosophy

Degree Awarded:
August 2022

***Advisory Committee*:**

Professor	**Gyu-Ho Lim, Chair**
Professor	**Wookap Choi, Advisor**
Professor	**Seok-Woo Son**
Doctor	**Dong-Joon Kim**
Professor	**Baek-Min Kim**

Abstract

The polar vortex and planetary waves are important dynamical phenomena in the winter stratosphere, which dominate large-scale circulation, tracer distribution and ozone depletion, and stratosphere-troposphere coupling. This study explored the evolution and interannual variability of the polar vortex and planetary waves, focused on the seasonal transition period in the Northern Hemisphere (NH) spring, using the ERA-Interim reanalysis data for 1979–2018.

In terms of polar vortex and breakup in NH seasonal transition to spring, conventional diagnostics used threshold values of potential vorticity (PV) or zonal wind speed based on the lower stratospheric polar vortex. Those diagnostics cannot be applied to the upper stratospheric polar vortex, of which evolution of PV is more complicated and zonal wind speed is much higher to prescribe the threshold values. In this study, the dates of polar vortex formation and breakup could be newly defined without prescribing threshold PV or zonal wind speed, based on the temporal change in the new "edge-change" metric, which is the average of the rates of changes in area-equivalent latitude, PV, and zonal wind speed at the edge of the vortex.

By applying the new diagnostic, the formation and breakup dates of the polar vortex for the whole stratosphere were obtained and compared to the dates of the stratospheric final warming. To see if the new diagnostic is consistent with tracer transport near the vortex edge, the formation and breakup of the polar vortex were compared with the zonal standard deviation of the mixing ratios of long-lived trace species. It turned out that the newly

defined polar vortex breakup dates well match the changes in the mixing ratio of the trace gases in the stratosphere for the winter. Considering all the above observations, the new diagnostic for vortex formation and breakup appears to be applicable to the whole stratosphere.

In terms of interannual variability of the stratospheric planetary waves in NH spring, the development of large-amplitude planetary waves in March in the upper stratosphere was investigated. During the 10-hPa easterly QBO, the geopotential height wave number 1 (wave-1) amplitude at 3 hPa was significantly larger than that during the westerly QBO for cases of large-amplitude planetary waves. Case studies on an easterly QBO case in 1994 and a westerly QBO case in 1995 were conducted for individual events of the wave-1 planetary wave growth. During the easterly QBO in March 1994, a developing perturbation at middle latitudes moved rapidly northeastward to replace the decaying high-latitude wave. In the early stage, the zonal-mean-to-eddy kinetic energy conversion in the subtropical region was crucial for wave development. This energy conversion was related to the negative meridional shear of the zonal wind in the middle latitudes. Negative meridional zonal wind shear was produced by the secondary meridional circulation associated with the equatorial QBO. After the perturbation started to develop in the middle latitudes, it moved northeastward over a few days due to potential vorticity flux, and the growth of the high-latitude waves was enhanced.

Composite analyses indicate that the dynamical characteristics of wave-1 growth found in March 1994 can be found in March in the easterly QBO years. The composite analysis also showed that the meridional shear of the

zonal wind in the middle latitudes was negative during the easterly QBO in March and plays an important role in developing the high-latitude wave-1 planetary wave. The dynamic response of the planetary waves to different QBO profiles was further examined by the general circulation model (GCM) experiments. The result shows the larger wave-1 amplitude and a similar wave-1 growth pattern in the easterly QBO experiments in April instead of March, probably due to the longer and colder winter in the GCM climatology. This study implies an important role of internal dynamics related to the QBO in developing planetary waves in the seasonal transition period when the influence of the vertical propagation of planetary waves is relatively weak.

Keywords: Boreal spring stratosphere, Polar vortex diagnostic, Planetary wave development, Quasi-biennial oscillation, Eddy kinetic energy, Secondary meridional circulation

Student Number: 2008-20403

Table of Contents

Abstract.. i

Table of Contents.. iv

List of Figures.. vi

List of Tables xvi

1. Introduction..1

2. Data and Model...8

   2.1. Reanalysis Data...8

   2.2. Satellite Tracer Data...9

   2.3. General Circulation Model 11

3. Evolution and Breakup of Polar Vortex 12

   3.1. Conventional Diagnostics of Polar Vortex.......................................12

      3.1.1. Polar vortex in the lower stratosphere......................................12

      3.1.2. Polar vortex in the upper stratosphere......................................19

   3.2. Edge-change Diagnostic for Polar Vortex...23

      3.2.1. Edge-change metric..23

      3.2.2. Comparisons with conventional diagnostics...............................28

      3.2.3. Application of edge-change diagnostic 33

   3.3. Validation of Edge-change Diagnostic..36

      3.3.1. Breakup of polar vortex and SFW...36

      3.4.2. Tracer distributions...41

4. Stratospheric Planetary Waves in NH Spring 47

4.1. Interannual Variability in Planetary Waves....................................47

4.1.1. Climatological characteristics 47

4.1.2. Interannual variability in wave-1 amplitude and QBO 51

4.2. Case Study: Planetary Wave Development in March 1994 and 1995 57

4.2.1. Daily evolution of wave-1 growth 57

4.2.2. Eddy forcing...62

4.2.3. Potential vorticity and enstrophy..66

4.2.4. Eddy kinetic energy..72

4.3. Composite Analysis: Daily Evolution of Planetary Waves and QBO 77

4.3.1. Identification of wave-1 growth events................................77

4.3.2. Response of wave-1 growth to QBO....................................81

4.3.3. Kinetic energy conversion..89

4.4. Dynamic Mechanism of QBO Modulation on Planetary Waves in NH Spring...93

4.4.1. Secondary meridional circulation...93

4.4.2. General circulation model simulations...............................103

5. Summary and Conclusions 116

References 123

국문초록 132

List of Figures

Figure 3.1 Isolines of MPV (contours, PVU) and its meridional gradient (red shading) over EL and time on the 450 K isentropic surface in the NH for 1996–1997. The blue contour represents the average wind speed (m s^{-1}) along the MPV isoline. The black squares indicate the edge of the polar vortex. The red vertical lines A, B, and C denote 10 March, 10 May, and 20 May, respectively. 16

Figure 3.2 MPV gradient (red line) and wind speed (blue line) along the MPV isolines versus EL on the 450 K surface on (a) 10 March, 1997, (b) 10 May, 1997, and (c) 20 May, 1997, and in the right panel, their corresponding MPV fields (d), (e), and (f) for the same dates, respectively. The location of the vortex edge on each day is marked by a dotted line in the left panel and a thick black solid contour in the right panel...17

Figure 3.3 On the 450 K surface: (a) The black squares and line denote the values of MPV at the vortex edge and 80°N in EL, respectively. The horizontal dashed line represents 18.6 PVU, and the green vertical lines represent the 3-month winter period. (b) The maximum wind speed along the MPV isolines. The horizontal dashed line represents 15.2 m s^{-1}. (c) The zonal wind speed for which the contour encloses the area equivalent to 75°. The horizontal dashed line indicates 25 m s^{-1}.........18

Figure 3.4 (a) Isolines of MPV (contours, PVU) over EL and time on the 1260 K isentropic surface in the NH for 1996–1997. The green and blue contours represent 18.9 and 14.4 PVU, respectively. The black squares indicate the edge of the polar vortex. The red vertical lines A, B, C, and D denote 15 January, 10 February, 25 March, and 15 April, 1997, respectively. (b) The black squares show the MPV at the vortex edge. The two horizontal dashed lines represent 18.9 and 14.4 PVU, respectively. The green vertical lines represent the 3-month winter period. The blue vertical lines represent the period from 18 February to 10 April. 21

Figure 3.5 Same as in Figure 3.2 but on the 1260 K surface for (a) 15 January, (b) 10 February, (c) 25 March, and (d) 15 April, all in 1997, and (e)–(h) are their corresponding MPV fields. The location of the subtropical edge is marked by a dotted line in (d) and dotted contour in (h). 22

Figure 3.6 Isolines of MPV (contours, PVU) and its meridional gradient (red shading) in EL (10°S–80°N) and time on the 1260 K isentropic surface in the NH for 1996-1997. The blue contour represents the average wind speed (m s−1) along the MPV isoline. The black squares indicate the edge of the polar vortex. 26

Figure 3.7 Changes in time of (a) EL at the vortex edge, (b) MPV, and (c) average wind speed along the MPV isoline at the vortex edge on the 1260 K surface, and (d) normalized changes of EL (green line), MPV (red line), and wind speed (blue line) and their average (black line) at the vortex edge. 27

Figure 3.8 Comparison of polar vortex breakup dates in the NH on 510 K isentropic surfaces for the period 1979–2018 using the "PV and U," "U area," "PV area," and "edge-change" criteria. The red diamonds denote the years 2009 and 2013. 30

Figure 3.9 Isolines of MPV (contours, PVU) and its meridional gradient (red shading) in EL (10°S–80°N) and time on the 510 K isentropic surface (upper panels) and normalized changes of EL, MPV, and wind speed and their average in the NH (lower panels) for (a) 2008-2009 and (b) 2012-2013. The blue contour represents the average wind speed (m s^{-1}) along the MPV isoline. The black squares indicate the edge of the polar vortex. 30

Figure 3.10 Same as in Figure 3.2 but on the 510 K surface on (a) 22 January, 2009, (b) 10 February, 2009, (c) 28 February, 2009, (d) 10 April, 2009, and (e) 30 April, 2009, and in the right panel their corresponding MPV fields (f), (g), (h), (i), and (j) for the same dates, respectively. Location of the vortex edge on each day is marked by a dotted line in the left panel and a thick black solid contour in the right panel. Location of the subtropical edge is marked by a dotted line in (c) and (e) and dotted contour in (h). 31

Figure 3.11 Same as in Figure 3.2 but on the 510 K surface on (a) 3 January, 2013, (b) 20 January, 2013, (c) 5 February, 2013, (d) 20 April, 2013, and (e) 10 May, 2013, and in the right panel their corresponding MPV fields (f), (g), (h), (i), and (j) for the same dates, respectively. 32

Figure 3.12 The dates of the formation and breakup of the NH and SH polar vortex (orange line) and their average (thick black line) from 430 K to 1260 K for the period 1979–2018...35

Figure 3.13 The black solid lines denote the vortex breakup dates determined by the "edge-change" method at (a) 1260 K in NH, (b) 1260 K in SH, (c) 510 K in NH, and (d) 510 K in SH for the period 1979–2018. The red solid and dotted lines in (b) and (d) are the linear trends for 1979–2000 and 2000–2018, respectively. The red solid line is statistically significant at the 95% confidence level ($p = 0.018$)..35

Figure 3.14 Zonal-mean zonal wind (m s^{-1}) from 430 K to 1260 K averaged from 60°N to 80°N for the period 1979–2018. The red circles and green diamonds denote the dates of the vortex breakup obtained by the "edge-change" method and the SFW defined by the 10 m s^{-1} threshold, respectively. The yellow squares denote the SFW defined by the 5 m s^{-1} threshold. 38

Figure 3.15 CH_4 and O_3 mixing ratios observed by ILAS in EL and time on the 1260 K, 800 K, and 450 K isentropic surfaces in the NH from 1 November, 1996, to 30 June, 1997. The black square denotes the location of the vortex edge each day, and the vertical line represents the date of the polar vortex breakup using the "edge-change" method.................43

Figure 3.16 Standard deviation of the mixing ratios of (a) CH_4, (b) N_2O, (c) H_2O, and (d) O_3 following the latitude circle from the ILAS observations from 1 November, 1996, to 30 June, 1997. The gray isolines represent the potential temperature, and the red solid circle denotes the date of the polar vortex breakup on each isentropic surface using the "edge-change" method. 44

Figure 3.17 Standard deviation of the O_3 mixing ratio (denoted by color shading) following the latitude circle from the POAM II (October 1993–November 1996), ILAS (November 1996–June 1997), and POAM III (April 1998–November 2005) observations, and the daily maximum MPV (10^{-6} K m^2 kg^{-1} s^{-1}; denoted by contours) on each isentropic surface in the NH for the period 1992–2005. The red solid diamonds and circles denote the dates of the formation and breakup of the polar vortex, respectively. In the lower part of each panel, the latitudes of the POAM II, ILAS, and POAM III observations are represented by blue, yellow, and red lines, respectively. 45

Figure 3.18 Same as in Figure 3.17 but for the SH. The contour lines represent the daily minimum MPV on each isentropic surface. 46

Figure 4.1 Monthly climatological averages of the GPH wave-1 amplitude from December to March (color scale) and its coefficients of variation (standard deviation to the mean; contours with intervals of 0.05) for the period of 1979–2019. 49

Figure 4.2 (a), (c) Monthly mean wave-1 amplitude of the daily GPH in the NH, and (b), (d) zonal-mean zonal wind in the low-latitude region in March 1994 (upper panels) and 1995 (lower panels). 50

Figure 4.3 Scatter plots of the high-latitude Z_1 at 3 hPa versus equatorial u at 10 hPa in (a) January, (b) February, and (c) March for the period 1980–2019. The blue and red numbers denote QBOe and QBOw years, respectively. Horizontal dashed lines represent the climatological mean of Z_1 for each month. 54

Figure 4.4 Composite differences of Z_1 between QBOe and QBOw for (a) all years, and (b) large-amplitude years. Blue (negative) and red (positive) dotted and solid lines represent statistical significance at the 90% and 95% levels, respectively. 55

Figure 4.5 Scatter plots of the monthly mean high-latitude wave-1 amplitudes (averaged over 60–80°N) at 3 hPa versus the preceding three-month average of the Niño 3.4 indices. The numbers denote the year, and the colors of filled circles represent the QBO zonal-mean zonal winds (averaged over 5°S–5°N) at 10 hPa. The vertical and horizontal dashed lines with values are climatological averages of the Niño 3.4 indices and monthly mean high-latitude wave-1 amplitudes, respectively, for 1980–2019. 56

Figure 4.6 Daily evolution of the GPH zonal anomaly at 3 hPa shown by contours, and its wave-1 component (shown by color shading) for (a) 18–29 March, 1994, and (b) 11–22 March, 1995. The contour intervals are 200 m. 60

Figure 4.7 Daily evolution of zonal wave-1 at 3 hPa (amplitude indicated by shading), and the phase (shown by contours): (a) March 1994 and (b) March 1995. The blue and red vertical dotted lines denote the days with the minimum and maximum high-latitude amplitude, respectively. The thick dashed line between 30°N and 70°N in (a) represent the date of the maximum amplitude at each latitude during Event 94. See the manuscript for a description of red characters A–H. 61

Figure 4.8 Daily evolution of (a), (d) eddy momentum flux in contours (interval = 100 m^2 s^{-2}) and its meridional divergence (indicated by shading); (c), (d) eddy heat flux (indicated by contours; interval = 50 K m s^{-1}) and its vertical divergence (indicated by shading); and (e), (f) EPFD at 3 hPa in March. The left and right columns are for 1994 and 1995, respectively. See the manuscript for a description of red characters A–H. 64

Figure 4.9 Meridional section of the phase of the wave-1 (indicated by contours), EP flux (indicated by red arrows), and EPFD (indicated by shading) in March (a) 1994 and (b) 1995. (A)–(H) are the same dates as in Figure 4.7. Reference arrows represent 10^7 and 10^5 kg s^{-2} for the meridional and vertical components, respectively...............................65

Figure 4.10 Longitude-latitude distributions of (a) q' (left column), (b) $v'q'$ (central column), and (c) $v'q'$ (right column) at 3 hPa for 20–28 March, 1994 at 2-day intervals. 69

Figure 4.11 Schematic diagrams of the wave-1 amplification process through the wave-mean flow interaction that contributes to the increase in potential enstrophy. 70

Figure 4.12 Daily evolution of the (a), (d) potential enstrophy (10^{-9} s^{-2}), (b), (e) rate of change in potential enstrophy (10^{-15} s^{-3}), and (c), (f) wave–mean flow interaction term (10^{-15} s^{-3}), in March 1994 (left column) and March 1995 (right column). Blue and red vertical dotted lines denote the days with the minimum and maximum high-latitude amplitude, respectively. 71

Figure 4.13 Scatter plots of high-latitude Z_1 at 3 hPa versus high-latitude EKE at 3 hPa in (a) January, (b) February, and (c) March; the correlation coefficient r is shown. The blue and red numbers denote years with QBOe and QBOw phases, respectively. The horizontal dotted line represents the climatological mean Z_1 for each month. 75

Figure 4.14 Daily evolution of (a), (e) EKE (K') (J m^{-3}); (b), (f) $\partial K' \partial t$ (10^{-6} W m^{-3}); (c), (g) conversion of ZKE to EKE (10^{-6} W m^{-3}); and (d), (h) u (indicated by color shading) and $\partial u \partial y$ (indicated by contours) at intervals of 5 × 10^{-6} s^{-1} in March 1994 (left column) and March 1995 (right column). Blue and red vertical dotted lines denote the days with the minimum and maximum high-latitude amplitude, respectively. 76

Figure 4.15 Histograms of the (a) amplitude growth (ΔZ), (b) amplification period (Δt), and (c) wave-1 amplitude (Z_1) for a total of 746 events of the high-latitude wave-1 amplification. The red vertical dotted line in (a) denotes the median values of the amplitude growth (275 m). The solid triangles in red and blue with dotted lines in (b) and (c) show distributions of the significant amplification events ($\Delta Z > 275$ m) and the minor events ($\Delta Z < 275$ m), respectively. 79

Figure 4.16 Time series of the high-latitude wave-1 amplitude (averaged over 60–80°N) for 40 winter seasons of 1979/1980 to 2018/2019. The periods shaded by orange are the significant amplification events ($\Delta Z > 275$ m). 80

Figure 4.17 Composite averages of the zonal-mean geopotential height anomaly (contours plotted at 200 m intervals) and wave-1 geopotential height (color scale) for the significant wave-1 amplification events (ΔZ > 275 m) in March. (a) QBOe events (N = 19), (b) QBOw events (N = 18), and (c) composite difference between the QBOe and QBOw events. Areas enclosed by red and blue lines represent that the difference is statistically significant at the 95% level. 83

Figure 4.18 The same as in Figure 4.17, but for the QBOe events (N = 49) and QBOw events (N = 14) in January...84

Figure 4.19 Composite averages of the climatological anomalies of geopotential height wave-1 and wave-2 amplitudes at 3 hPa on time-latitude sections for the (a) QBOe events (N = 19) and (b) QBOw events (N = 18) in March. (c) Composite differences between the QBOe and QBOw events. Areas enclosed by red and blue lines represent that the difference is statistically significant at the 95% level. 85

Figure 4.20 The same as in Figure 4.19, but for the QBOe events (N = 49) and QBOw events (N = 14) in January...86

Figure 4.21 The same as in Figures 4.19 and 4.20, but for the climatological anomalies of zonal-mean temperature (T), zonal-mean zonal wind (u), eddy momentum flux ($u'v'$), eddy heat flux ($v'T'$), and divergence of the EP flux ($\mathbf{\nabla} \cdot \mathbf{F}$) in March. 87

Figure 4.22 The same as in Figure 4.21, but in January. 88

Figure 4.23 Composite averages of the climatological anomalies of eddy kinetic energy (EKE) and rate of change in EKE ($\partial K'\partial t$) on time-latitude sections at 3 hPa for the (a) QBOe events (N = 19) and (b) QBOw events (N = 18) in March. (c) Composite differences between the QBOe and QBOw events. Areas enclosed by red and blue lines represent that the difference is statistically significant at the 95% level. 90

Figure 4.24 Composite averages of the climatological anomalies of zonal-mean kinetic energy (ZKE) to eddy kinetic energy (EKE) conversion ($-u'v'\partial u\partial y$), and meridonal zonal wind shear ($\partial u\partial y$) on time-latitude sections at 3 hPa for the (a) QBOe events (N = 19) and (b) QBOw events (N = 18) in March. (c) Composite differences between the QBOe and QBOw events. Areas enclosed by red and blue lines represent that the difference is statistically significant at the 95% level. 91

Figure 4.25 The same as in Figures 4.22 and 4.23, but for the QBOe events (N = 49) and QBOw events (N = 14) in January. 92

Figure 4.26 Composite mean of monthly (a) wave-1 amplitude, (b) EKE, (c) conversion of ZKE to EKE, (d) u, and (e) $\partial u \partial y$ for January, March, and large-amplitude March. The blue and red curves denote QBOe and QBOw composites, respectively. Open and solid circles indicate that the difference is statistically significant at the 90% and 95% levels, respectively. 98

Figure 4.27 Differences in composite monthly means between QBOe and QBOw of (a) zonal wind, (b) RMC (indicated by arrows) and zonal-mean temperature (indicated by shading), (c) meridional shear of zonal-mean zonal wind, and (d) EP flux (indicated by arrows) and EPFD (indicated by shading). The left, center, and right columns are for January, March, and large-amplitude March, respectively. Dotted and solid lines indicate that the differences are statistically significant at the 90% and 95% levels, respectively. The black arrows indicate a statistical significance at the 95% level; gray arrows indicate significance at 90%. The reference arrow scales are (a) 0.5 m s^{-1} for $v*$ and 0.5 × 10^{-3} m s^{-1} for $w*$, and (c) 10^{6} and 10^{4} kg s^{-2} for the meridional and vertical EP flux components, respectively. 99

Figure 4.28 Composite averages of the column ozone distribution at each pressure layer derived from the SBUV ozone data sets from 1979 to 2018 for the QBOe and QBOw years in (a) January and (b) March. The filled and open circles represent that the composite difference between QBOe (blue) and QBOw (red) is statistically significant at the 90% and 95% levels, respectively. 101

Figure 4.29 Differences in composite monthly means between QBOe and QBOw of the (a) vertical EP flux (F$_{z}$; indicated by shading with an interval of 10^4 kg s^{-2}) and (b) F_z normalized by the climatological average of the vertical EP flux ($F_{z\ CLM}$) ($F_z/F_{z\ CLM}$). The left, center, and right columns are for January, March, and large-amplitude March, respectively. The dotted and solid lines in (a) indicate that the differences were statistically significant at the 90% and 95% levels, respectively. 102

Figure 4.30 (a) Climatological equatorial zonal-mean zonal wind profiles (averaged over 5°S–5°N) in January (blue lines) and March (red lines) derived from the ERA-Interim (dotted lines) and the SPARC climatology (solid lines). (b) Winter-average (November–March) of climatological equatorial zonal wind anomalies for the easterly QBO phase (QBOe) and westerly QBO phase (QBOw) from the ERA-Interim. (c, d) Composite mean of equatorial zonal-mean zonal wind profiles for QBOe and QBOw in ERA-Interim (dotted lines) and zonal-mean zonal wind profiles that relaxed toward in the WACCM experiments (solid lines) for January (blue lines) and March (red lines). 107

Figure 4.31 Comparisons of climatological time series of (a) polar cap height (GPH averaged over 65–90°N) and (b) high-latitude wave-1 amplitude (averaged over 60–80°N) at 3 hPa from the ERA-Interim reanalysis (1979/1980–2018/2019) and the SC-WACCM simulation results with four different QBO profiles (49 winters)..108

Figure 4.32 Distribution of the monthly mean high-latitude wave-1 amplitudes at 3 hPa from the SC-WACCM experiments. 109

Figure 4.33 Composite averages of the zonal-mean geopotential height anomaly (contours plotted at 200 m intervals) and wave-1 geopotential height (color scale) for the significant wave-1 amplification events ($\Delta Z > 275$ m) in March from the SC-WACCM experiments. (a) QBOe-M profile (N = 70), (b) QBOw-M profile (N = 52), and (c) composite difference between the QBOe-M and QBOw-M events. Areas enclosed by red and blue lines represent that the difference is statistically significant at the 95% level. 112

Figure 4.34 Composite averages of the zonal-mean geopotential height anomaly (contours plotted at 100 m intervals) and wave-1 geopotential height (color scale) for the significant wave-1 amplification events (ΔZ > 275 m) in April from the SC-WACCM experiments. (a) QBOe-M profile (N = 21), (b) QBOw-M profile (N = 14), and (c) composite difference between the QBOe-M and QBOw-M events. Areas enclosed by red and blue lines represent that the difference is statistically significant at the 95% level. 113

Figure 4.35 Differences in composite monthly mean temperature between (a) QBOe-M and QBOw-M experiments and (b) QBOe-J and QBOw-J experiments. Areas enclosed by red and blue lines represent that the difference is statistically significant at the 95% level. 114

Figure 4.36 The same as Figure 4.35, but for the monthly mean zonal wind. 115

Figure 5.1 Schematic diagram representing changes in dynamic variables in each latitude band during Event 94. In the low latitudes (20–30°N), the maximum EKE occurred on 21 March. In the middle latitudes (30–40°N), the energy conversion reached a maximum on 23 March. In the 40–60°N latitude band, the negative $v'q'$ had gradually increased by 25 March, 1994. In the high latitudes (60–80°N), the sign of $v'q'$ changed from positive to negative on the minimum Z_1 day (24 March, 1994) and reached its negative maximum on 26 March, 1994. Finally, the maximum Z_1 appeared on 28 March, 1994. 121

Figure 5.2 Schematic diagram of the equator-to-pole interaction between the QBO and interannual variability of the high-latitude planetary waves in the upper stratosphere in March. 122

List of Tables

Table 4.1 Averages of the high-latitude monthly mean wave-1 amplitude at 3 hPa for the large-amplitude group (L), small-amplitude group (S), and total years for QBOe and QBOw. Climatological averages of the high-latitude wave-1 amplitude and numbers of years for each group (N) are additionally represented in the table. Composite difference between QBOe and QBOw is statistically significant only for the large-amplitude groups in March ($p < 0.001$; denoted by the bold characters). 53

Table 4.2 The numbers of the significant wave-1 amplification events (N) and the averages and standard deviations of the wave-1 amplitude growth (ΔZ), wave-1 amplification period (Δ*t*), and high-latitude amplitude (averaged over 60–80°N) of wave-1 (Z_1) and wave-2 (Z_2) for the QBOe and QBOw years for the period of 1979/1980–2018/2019. 82

Table 4.3 Designs of the WACCM experiments. 106

Table 4.4 Number of the significant wave-1 amplification events (N), that wave-1 amplitude growths are larger than median value from the ERA-Interim reanalysis ($\Delta Z > 275$ m), and the average and standard deviation of wave-1 amplitude growth (ΔZ), wave-1 amplification period (Δ*t*), high-latitude (averaged over 60–80°N) wave-1 and -2 amplitudes (Z_1 and Z_2) for the 49-year WACCM simulations with 4 scenarios of the QBOe-M, QBOw-M, QBOe-J, and QBOw-J. 110

1. Introduction

Stratospheric circulation in winter is mainly determined by radiative cooling and eddy transports. In the absence of solar heating in the polar night region, the meridional temperature gradient in the winter stratosphere induces strong zonal-mean westerly wind by the thermal wind balance. The strong circumpolar westerly wind in the winter stratosphere is often called the polar vortex. The westerly zonal wind in the winter hemisphere provides waveguides for the vertical propagation of planetary waves, particularly in the Northern Hemisphere (NH). Stratospheric planetary waves with a large amplitude are quasi-stationary and originate from tropospheric sources such as large-scale topography, planetary-scale heat sources and sinks, and averaged effects of synoptic-scale eddies (Plumb, 2010). Breaking of the vertically propagated planetary waves generates the zonal force that causes eddy-driven meridional circulation in the stratosphere. The eddy-driven meridional circulation plays a role in maintaining significant departures of the zonal-mean temperature distribution from its radiatively-determined state by adiabatic cooling and heating at the tropics and high latitudes.

The polar vortex and planetary waves significantly affect the distribution and chemistry of stratospheric trace gases. In the high latitudes, strong westerly wind at the boundary of the polar vortex generates steep meridional gradients in potential vorticity (PV) and isolates an extremely cold air mass with high PV. Therefore, the edge of the polar vortex acts as a barrier for mixing between the inside and outside air of the vortex (Hartmann et al., 1989; Schoeberl et al., 1992). The polar vortex plays an important role not only in large-scale circulation, distribution of trace gases, formation of the polar stratospheric cloud, and polar ozone depletion (Solomon, 1999; Choi et al., 2002a; Karpetchko et al., 2005) but also in the stratosphere-troposphere coupling on intraseasonal and interannual timescales through the annular mode (Baldwin and Dunkerton, 2001; Baldwin et al., 2003). The polar vortex can modulate tropospheric storm tracks and weather patterns via the northern annular mode (Baldwin and Dunkerton, 2001; Thompson et al., 2002). In the middle latitudes, planetary-scale eddy drives both slow meridional tracers transport by residual mean circulation (RMC) and rapid quasi-isentropic transport and mixing of tracers by breaking planetary waves. Therefore, both polar vortex and planetary waves play important dynamical and chemical roles in maintaining large-scale circulation in the winter stratosphere.

During the seasonal transition in spring, characteristics of the polar vortex and planetary waves are rapidly changed. Seasonal changes of the solar zenith angle reduce the meridional temperature gradient and thus zonal-mean westerly wind. In addition, the planetary waves breaking and dissipation further contribute deceleration of westerlies (Charney and Drazin, 1961). The final transition of zonal wind from westerly to easterly in the extratropical stratosphere is known as the stratospheric final warming (SFW). Since SFWs are often accompanied by the abrupt breaking of the polar vortex, SFWs are regarded as the same as the polar vortex breakup in several studies (Black et al., 2006; Black and McDaniel, 2007; Hardiman et al., 2011). Similar to the sudden stratospheric warming (SSW) events, SFW events also affect the tropospheric circulation by rapid deceleration of the high-latitude circumpolar westerlies in both the stratosphere and troposphere (Black et al., 2006; Black and McDaniel, 2007). Meanwhile, interannual variability in polar vortex persistence and timing of SFW in spring are sensitive to the intensity of vertically propagated planetary waves (Waugh et al., 1999; Wang et al., 2019). The seasonal transition of the stratospheric polar vortex and planetary waves are, therefore, significant factors in understanding interannual and decadal variability both in stratospheric dynamics and tropospheric weather.

In terms of interannual variability in the stratospheric seasonal transition, diagnostics of the polar vortex breakup are important. In previous studies, diagnostics of the polar vortex were generally based on two parameters, zonal wind and PV. The zonal-mean zonal wind at certain latitudes and heights with a wind velocity criterion has been widely used to identify the onset of spring (Black et al., 2006; Black and McDaniel, 2007; Hardiman et al., 2011; Hu and Ren, 2014). For example, SFWs are usually defined at the time when the zonal-mean zonal wind at a specific altitude and latitude falls below zero without returning to a threshold value until the subsequent autumn. The reason for the threshold value is that the zonal wind sometimes recovers from zero wind to a certain extent after a midwinter SSW before it completely falls below zero. However, the date of the SFW can be sensitive to the choice of the threshold value.

Although defining the polar vortex using the zonal winds is simple and easy and provides useful information in the zonal-mean sense, diagnosis using PV is more appropriate for quantifying the day-to-day variations in the polar vortex as well as its breakup events. Defining the edge of the vortex with PV distribution and identifying the polar vortex breakup with the threshold criterion of the prescribed parameters are useful (Nash et al., 1996;

Waugh et al., 1999). Prescribing the necessary parameter values is relatively easy in the lower stratosphere. In the upper stratosphere, however, it is hard to choose the right values for these parameters, and this is why an exact breakup date is not available for the upper-stratospheric polar vortex. Dynamical features in the upper stratosphere are usually more complicated than those in the lower stratosphere. One reason is midwinter SSW; following SSWs, recovery of the westerly jet varies year-to-year. A lack of reliability of the upper-stratospheric dataset can also be another reason for difficulty in the breakup diagnosis at this level. The number of temperature observations is limited in the upper stratosphere due to the height limitations of the radiosonde, which induces bias in the reanalysis dataset (Marlton et al., 2021). Thus, determining the criteria for the upper-stratospheric vortex breakup is not easy compared to that for the lower stratospheric vortex.

The stratospheric planetary waves are significant in NH winter and spring. The planetary waves in NH are dominated by the wavenumber 1 component (wave-1), and the maximum amplitude of wave-1 occurs in the high-latitude upper stratosphere. Previously, Lee (1999) investigated the planetary waves at 3 hPa in NH during 1993–1996. In March, the stratospheric wave-1 amplitudes at 3 hPa were larger in 1994 and 1996 than those in 1993 and 1995. However, no significant differences were found between January and February. Interestingly, the equatorial stratospheric zonal winds in the mid-stratosphere (~10 to 30 hPa) were easterly in 1994 and 1996, and westerly in 1993 and 1995.

Since the planetary waves in the stratosphere are transported from the troposphere, its interannual variability is known to be related to the tropospheric forcing like the El Niño–Southern Oscillation (ENSO) (e.g., Garfinkel and Hartmann, 2007). Another important source of interannual variability in planetary waves is the quasi-biennial oscillation (QBO), which is the quasi-periodic (~28 months on average) downward propagation of easterly and westerly winds in the equatorial stratosphere (~16–50 km) (Baldwin et al., 2001). Holton and Tan (1980) reported that the high-latitude geopotential height (GPH) at 50 hPa in winter was larger during the easterly QBO at 50 hPa; this is known as the "Holton-Tan relationship." They hypothesized that the meridional shift of the zero-wind line induced by the QBO modulates the vertically propagating planetary waves and their interaction with the stratospheric polar vortex. However, the Eliassen-Palm (EP) flux and amplitudes of the planetary waves show small differences between QBO phases (Holton and Tan, 1980; Dunkerton and Baldwin, 1991).

The Holton-Tan relationship is sensitive to the magnitude of the tropospheric planetary wave forcing (Holton and Austin, 1991; O'Sullivan and Young, 1992). Therefore, isolating QBO-related signals in the stratosphere from the tropospheric variability like ENSO is difficult (Garfinkel and Hartmann, 2007; Wei et al., 2007). In some studies, the conventional Holton-Tan explanation is not applicable to either the reanalysis data or model simulations (e.g., Naoe and Shibata, 2010; Yamashita et al., 2011; Garfinkel et al., 2012). As an alternative explanation of the Holton-Tan relationship, modulation of planetary wave propagation by the QBO-induced meridional circulation has been proposed (e.g., Ruzmaikin et al., 2005). The vertical wind shear of the QBO generates a secondary meridional circulation to maintain thermal wind balance (Plumb and Bell, 1982; Baldwin et al., 2001;

Choi et al., 2002b), and induces a horseshoe-shaped downward arching zonal wind anomaly in the subtropics (Crooks and Gray, 2005; Garfinkel et al., 2012; Hansen et al., 2013; Rao et al., 2021). The QBO-induced meridional circulation can modulate the refractive index for planetary wave propagation, and thus the EP flux and its convergence in the middle-to-upper stratosphere at high latitudes, while the shift of the critical line by the QBO still plays a role in the subtropical lower stratosphere (Garfinkel et al., 2012; Lu et al., 2014). In the most studies, the zonal wind at 50 hPa is used to determine the phase of the QBO. In some studies, however, the upper level QBO is focused on. For example, Gray et al. (2001) and Gray (2003) suggested the possible influence of a Holton-Tan type relationship due to the vertically deep equatorial zonal wind anomaly, i.e., the upper-stratospheric QBO and mesospheric semiannual oscillation. This result was supported by Watson and Gray (2014), who examined the transient response of the polar stratosphere to forcing by the QBO using a global circulation model (GCM). Most studies have focused on the winter season when investigating the interannual variation of planetary waves induced by QBO modulation. However, there have been relatively few studies on the influence of QBO on the planetary waves in spring.

Based on the aforementioned backgrounds, this study aimed to explore the evolution and interannual variability of the polar vortex and planetary waves particularly focused on the upper stratosphere in NH spring. In Chapter 2, the reanalysis and satellite data and the model simulations utilized in this study are described. In Chapter 3, the formation, evolution, and breakup of the polar vortex are investigated with a new diagnostic that does not require prescribing parameters and can be used in the upper stratosphere as well as in the lower stratosphere. The formation and breakup dates of the polar vortices are compared to the mixing ratios of methane (CH_4), nitrous oxide (N_2O), water vapor (H_2O), and ozone (O_3) observed by satellite instruments. By observing tracer concentrations, the usefulness of the new definition of vortex formation and breakup can be evaluated. The breakup dates of the polar vortex obtained by this method are additionally compared with the dates of SFWs. In Chapter 4, the interannual variability in the stratospheric planetary waves is investigated concerning the equatorial QBO. Differences in the wave-1 amplitude in March dependent on the QBO are discussed with a case study, composite analysis, and general circulation model (GCM) simulations on wave developments in each QBO phase in terms of various dynamical variables, including eddy forcing, enstrophy, and eddy kinetic energy (EKE). The role of changes in secondary meridional circulation by the phases of the QBO is further examined and discussed. Finally, the results and key findings of this study are summarized in Chapter 5.

2. Data and Model

2.1. Reanalysis Data

Dynamic variables of GPH, air temperature, horizontal and vertical wind data for the period January 1979 to August 2019 were obtained from the European Center for Medium-Range Weather Forecasts (ECMWF) Re-Analysis Interim (ERA-Interim; Dee et al., 2011). Data were provided four times per day at 37 pressure levels (from the surface to 1 hPa) with a horizontal resolution of 1.5° × 1.5°. Daily mean GPH, temperature, zonal and meridional winds, and vertical motion were calculated and used in this study.

Isentropic PV is generally used for the polar vortex diagnosis. In this study, the isobaric variables from the ERA-Interim were interpolated onto 22 isentropic levels from 380 K (~ 15 km altitude) to 1260 K (~ 41 km altitude) with 1.2-km vertical spacing for calculating the isentropic PV. Since the isentropic PV increases exponentially with height, the modified PV (MPV) was produced following Lait (1994) by multiplying a scaling factor of $(\theta/\theta_0)^{-9/2}$, where θ_0 is the reference potential temperature of 420 K. The unit for MPV is the PV unit (PVU), where 1 PVU is 10^{-6} K m^2 kg^{-1} s^{-1}. The two-dimensional spatial distribution of PV can be simplified by conversion into a monotonic one-dimensional function of the area enclosed by each MPV isoline or equivalent latitude (EL), that is, a latitude equivalent to the area within the PV isoline (Butchart and Remsberg, 1986).

The phase of the QBO was determined based on the ERA-Interim data. The equatorial stratosphere in the ECMWF reanalysis data, including ERA-40 and ERA-Interim data, is better-represented up to 2–3 hPa (Baldwin and

Gray, 2005; Dee et al., 2011) in comparison with the long-term rocketsonde and rawinsonde observations of tropical in-situ observatories (Naujokat, 1986). In this study, the phase of the QBO was defined by equatorial zonal-mean zonal wind at 10 hPa (averaged over 5°S–5°N) from the ERA-Interim. To examine probable influence of the El Niño–Southern Oscillation (ENSO) on the relationship between the high-latitude planetary waves in the upper stratosphere and the QBO, the Niño 3.4 (5°S–5°N, 170°–120°W) sea surface temperature (SST) anomaly was additionally used in this study.

2.2. Satellite Tracer Data

The boundary of the strong polar vortex plays the role of a transport barrier (Hartmann et al., 1989; Schoeberl et al., 1992), and hence, the concentrations of trace species that are rich in the subtropics have large differences across the vortex boundary. As shown in Choi et al. (2002a), the concentration of long-lived chemical species is a good indicator of the evolution of the polar vortex. In this study, the formation and breakup dates of the polar vortices were compared to the mixing ratios of stratospheric tracer gases observed by satellite instruments.

The Improved Limb Atmospheric Spectrometer (ILAS) is an instrument onboard the Advanced Earth Observing Satellite and provides mixing ratios of CH_4, N_2O, H_2O, and O_3 (Sasano et al., 1999; Yokota et al., 2002). ILAS uses the solar occultation method and observes only the high-latitude regions. Although the solar occultation measurements have disadvantages of low sampling frequency and limited latitudinal coverage compared to the limb emission sounding, they give the most accurate concentration data. During the 8 months of operation from November 1996 through June 1997, ILAS observations covered the high latitudes in NH (57–72°N) and Southern Hemisphere (SH; 64–89°S). During any day, observations took place up to 14 times following the latitude circle.

In addition to the ILAS data, O_3 mixing ratio data from the Polar Ozone and Aerosol Measurement (POAM) II and POAM III (Glaccum et al., 1996; Lucke et al., 1999) were used in this study. POAM II and III were onboard the Satellite Pour l'Observation de la Terre (SPOT) 3 and SPOT 4 satellites, respectively. Similar to ILAS, POAM II and III also used the solar occultation technique and covered the periods from November 1993 to November 1996 and from April 1998 to December 2005, respectively. The mixing ratio of O_3 was used for these periods, since long-lived chemical species, such as CH_4 and N_2O, were not observed by POAM II and III. O_3 was observed up to 14 times a day following the latitude bands of 54–71°N and 63–88°S.

The QBO impact on the secondary meridional circulation in tropics and subtropics were compared with the long-term satellite-based stratospheric O_3 data. The Solar Backscatter Ultraviolet (SBUV) Merged Ozone Data Set (MOD) version 8.6 (Firth et al., 2014) is an integrated total and profile O_3 (in Dobson unit; DU) retrieved from the ten independent satellite-onboard instruments, including the BUV, SBUV, and SBUV/2, which share the fundamental measurement technique, and a next-generation instrument, the Ozone Mapping Profiler Suite (OMPS) Nadir Profiler onboard the Suomi NPP satellite. The data span 49-year period from May 1970 to December 2018 (except intermittent missing in mid-1970s). In this study, six layers of monthly 5° zonal-mean profile ozone from the layer 10 (16.06 hPa to 10.13

hPa) to the layer 15 (1.606 hPa to 1.013 hPa) for the period of 1980–2018 were employed.

2.3. General Circulation Model

To examine the response of the stratospheric dynamic fields to different QBO profiles at the equator, the Community Earth System Model (CESM) version 1.2.2 with the Whole Atmosphere Community Climate Model (WACCM) as an atmospheric component was employed in this study. The WACCM includes all the physical parameterizations from the Community Atmosphere Model version 4 (CAM4) (Marsh et al., 2013; Neale et al., 2013) and has a horizontal resolution of 1.9° × 2.5° with 66 hybrid pressure-sigma levels up to approximately 140 km above the surface. The model was run with fixed sea surface temperature (SST) and sea ice data as a lower boundary condition. For the chemistry, the configurations of perpetual AD 2000 emission inventory with specified chemistry (SC) were applied to reduce the computational cost. The SC-WACCM is known to be highly cost-effective despite the no significant differences in the surface, tropospheric, and stratospheric climate simulations (Smith et al., 2014).

3. Evolution and Breakup of Polar Vortex

3.1. Conventional Diagnostics of Polar Vortex

3.1.1. Polar vortex in the lower stratosphere

In this section, the evolution of the polar vortex in the lower stratosphere was described to reveal the characteristic features and how they differ from those in an upper-stratospheric polar vortex. For the case study, the year 1996–1997 is chosen, when the ILAS tracer data are available to be compared to the evolution and breakup of the polar vortex. Note that the variables on the time-EL domain are smoothed three times by 1-2-1 smoothing (3-point moving average using 0.25:0.5:0.25 weighting) in EL and by a 5-day running mean in time to reduce the noises in PV and EL.

Figure 3.1 shows the evolution of the polar vortex on the 450 K (~ 17 km) isentropic surface, represented by MPV, gradient of MPV over EL, and average wind speed along the MPV isolines. The location of the vortex edge is defined by the maximum of the average wind multiplied by the meridional gradient of the MPV in EL following Nash et al. (1996). From January to April in 1997, the maximum MPV gradient is located near 65°N and is in good agreement with the maximum wind speed. The edge of the polar vortex is also located near the maximum MPV gradient during the same period. In May, the polar vortex decays rapidly. To observe the characteristic features of the vortex more clearly, three days are selected and denoted by A, B, and C. These days represent the mature vortex (10 March 1997) and before (10 May 1997) and after (20 May 1997) the breakup of the polar vortex, respectively.

Figure 3.2 shows the MPV gradient and wind speed over EL as well as the isentropic distribution of MPV on the days of A, B, and C. In the mature stage of the polar vortex on 10 March 1997, the edge of the polar vortex with 20.1 PVU (Figure 3.1) corresponds to distinct peaks in both MPV gradient and wind speed at the EL of 65°N (Figure 3.2a). The edge is also clearly discernible by the color contrast in the MPV distribution in Figure 3.2d. As the season progresses toward summer, the polar vortex weakens and both the maximum MPV value and the area of the polar vortex decrease. On 10 May 1997, the edge of the vortex with 17.4 PVU (Figure 3.1) at 69°N has a much smaller MPV gradient and wind speed, and the vortex has broken into two parts (Figure 3.2e). On 20 May 1997, the peaks in both the MPV gradient and wind speed are not found anymore (Figure 3.2c), and the vortex shape does not appear in the isentropic distribution (Figure 3.2f). Therefore, the polar vortex must have broken up sometime in the period 10–20 May 1997.

To determine the exact vortex breakup date, three conventional diagnostics, which are summarized and discussed by Waugh et al. (1999), can be used; following their notation, these are "PV area," "PV and U," and "U area."

(1) In the "PV area" method, the vortex breakup is defined when the area within a specific PV isoline, which represents the boundary of the polar vortex, becomes less than a minimum area (Manney et al., 1994; Waugh and Randel, 1999). Waugh and Randel (1999) used the average PV at the daily boundary of the polar vortex for wintertime (December to February; DJF) for this specific PV value and used the

80°-latitude circle for the minimum area.

(2) In the "PV and U" method suggested by Nash et al. (1996), the edge of the vortex is found using the maximum PV gradient constrained by strong nearby zonal wind, and the vortex breakup is defined to be when the average wind speed along the vortex edge becomes smaller than a critical value. Nash et al. (1996) used the criterion of 15.2 m s^{-1} for the breakup dates at 450 K.

(3) In the "U area" method by Waugh et al. (1999), the vortex breakup is defined to occur when the total area within which the zonal wind exceeds a specific value falls below a minimum value. Waugh et al. (1999) used 25 m s^{-1} as the criterion and the region within the 75°-latitude circle as the minimum area.

Figure 3.3 shows that the three methods are applied to obtain the breakup date of the polar vortex on the 450 K isentropic surface. All of the three diagnostic methods can be easily applied to the above case since the polar vortex evolution in the lower stratosphere is relatively simple.

To apply the "PV area" method (Figure 3.3a), the value of MPV is needed to represent the location of the edge, and the average MPV during DJF is used following Waugh and Randel (1999). As shown in Figures 3.1 and 3.3a, MPV has small variability during DJF at the vortex edge. Since the MPV value at the vortex edge does not change much, using the average winter value of 18.6 PVU seems reasonable. Using this value and the MPV at 80°N in EL, the vortex breakup date is determined to be 17 May, 1997. In the "PV and U" method (Figure 3.3b), the date of the vortex breakup is defined as the date when the maximum wind speed averaged along the MPV isolines falls below 15.2 m s^{-1} (Nash et al., 1996). The choice of the value 15.2 m s^{-1} in the lower stratosphere is somewhat arbitrary, but it looks to be applicable for the case in Figure 3.3b. This method determines the date of the polar vortex breakup to be 13 May, 1997. Using the "U area" method in Figure 3.3c, when the zonal wind speed at 75°N becomes smaller than the threshold value of 25 m s^{-1}, following Waugh et al. (1999), the polar vortex breakup date is determined to be 3 May, 1997.

The dates of the 1996–1997 NH polar vortex breakup at 450 K defined by three different methods are dependent on the choice of parameters. Although choosing these parameters is subjective, the vortex dates can be determined after proper "tuning" of the parameters, as suggested by Waugh et al. (1999), particularly for the study of the interannual variations.

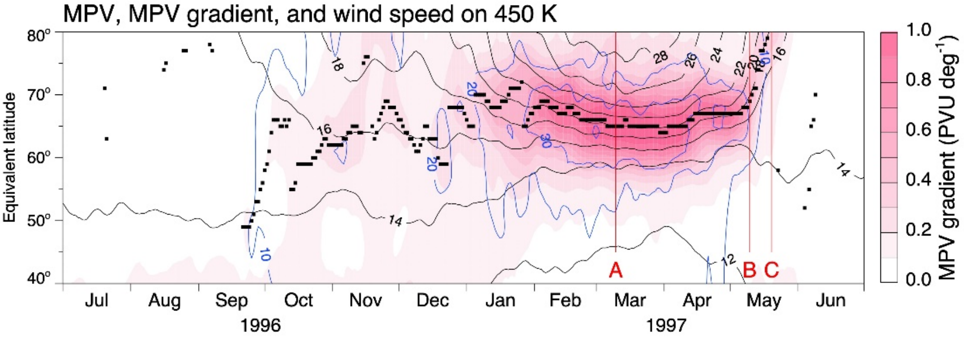

Figure 3.1 Isolines of MPV (contours, PVU) and its meridional gradient (red shading) over EL and time on the 450 K isentropic surface in the NH for 1996–1997. The blue contour represents the average wind speed (m s^{-1}) along the MPV isoline. The black squares indicate the edge of the polar vortex. The red vertical lines A, B, and C denote 10 March, 10 May, and 20 May, respectively.

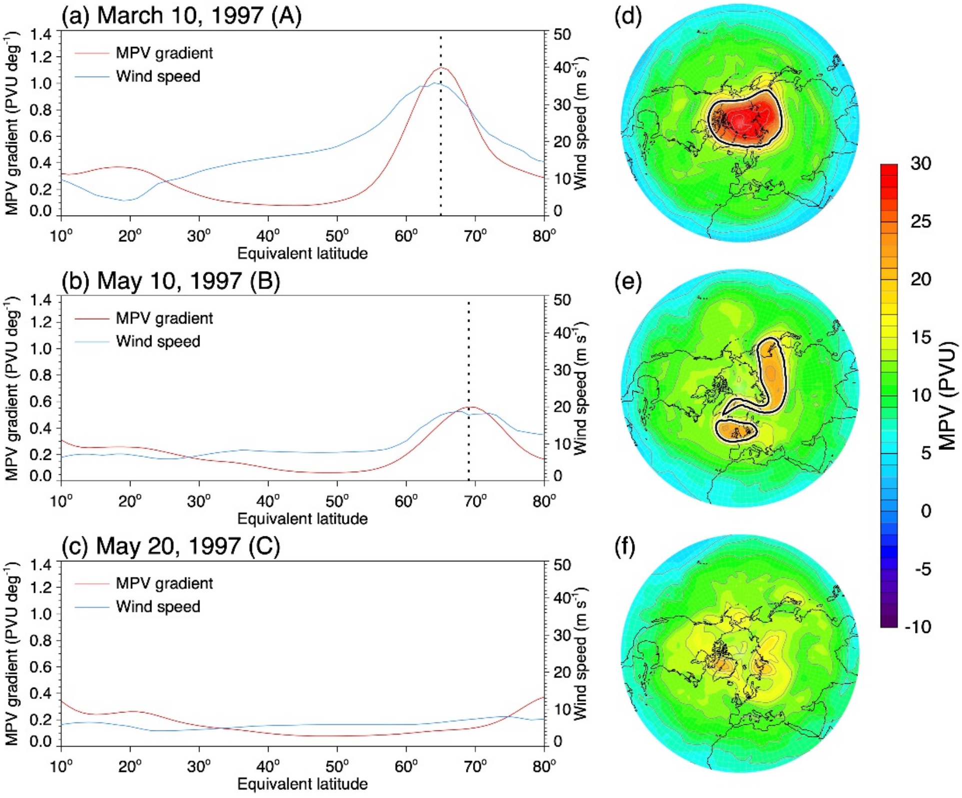

Figure 3.2 MPV gradient (red line) and wind speed (blue line) along the MPV isolines versus EL on the 450 K surface on (a) 10 March, 1997, (b) 10 May, 1997, and (c) 20 May, 1997, and in the right panel, their corresponding MPV fields (d), (e), and (f) for the same dates, respectively. The location of the vortex edge on each day is marked by a dotted line in the left panel and a thick black solid contour in the right panel.

(a) MPV at the edge (PV area)

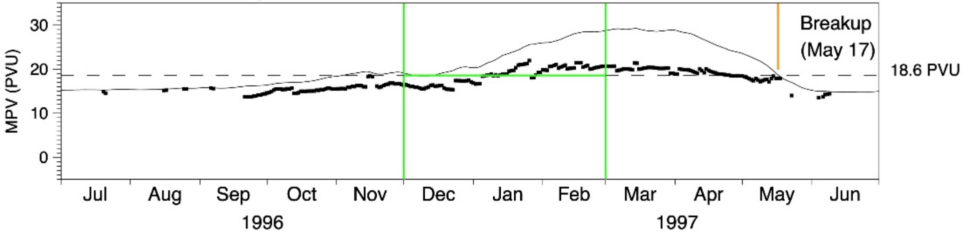

(b) Maximum wind speed along MPV isolines in NH (PV and U)

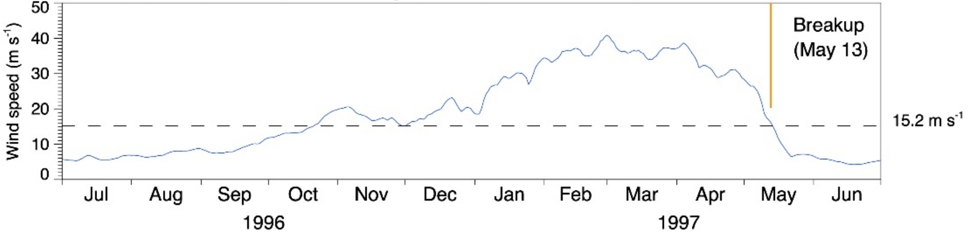

(c) Zonal wind speed of the area equivalent to 75° (U area)

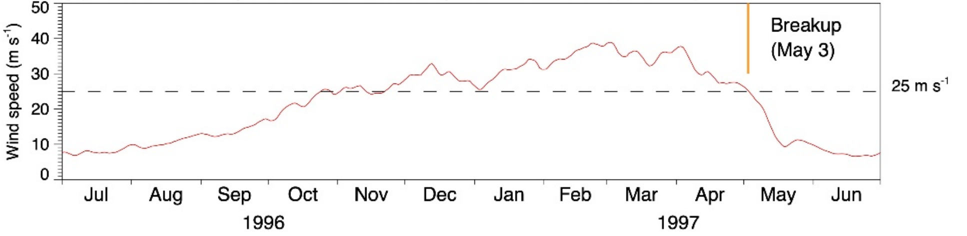

Figure 3.3 On the 450 K surface: (a) The black squares and line denote the values of MPV at the vortex edge and 80°N in EL, respectively. The horizontal dashed line represents 18.6 PVU, and the green vertical lines represent the 3-month winter period. (b) The maximum wind speed along the MPV isolines. The horizontal dashed line represents 15.2 m s^{-1}. (c) The zonal wind speed for which the contour encloses the area equivalent to 75°. The horizontal dashed line indicates 25 m s^{-1}.

3.1.2. Polar vortex in the upper stratosphere

To investigate whether the same approaches used in the lower stratosphere are applicable for determining the vortex breakup in the upper stratosphere, the NH polar vortex in 1996–1997 in the upper stratosphere is analyzed. Figure 3.4 exhibits the evolution of the polar vortex within the same time period at 1260 K (~ 41 km). In contrast to the lower stratosphere, MPV isolines show more complex behavior, which is due to the occurrence of the midwinter breakup of the polar vortex.

To use the "PV area" method, a MPV value representing the vortex edge is required. In this case, the DJF mean of the MPV at the daily vortex edge is 18.9 PVU (green line in Figure 3.4a) and appears to represent the seasonal vortex boundary only until late February. The vortex breakup date obtained using 18.9 PVU is 5 April 1997. Following this, another vortex, which formed in late February, is still present (Figure 3.4a) near 60°N in EL. In contrast to the lower stratosphere (Figure 3.1), the upper stratosphere in 1997 experiences significant variability in MPV during the winter; thus, defining the vortex edge by the winter-average MPV is not plausible. If a different MPV value are considered instead of the DJF mean, it could be found using Figure 3.4b. From 18 February through 10 April during the late stages of the polar vortex, the value of MPV does not change much at the edge, and its average for the 52-day period is 14.4 PVU. If this value is selected to define the vortex edge, then the vortex breakup date would be diagnosed as 28 April 1997. Without selecting the appropriate MPV value, which is applicable to the upper stratosphere each year, the "PV area" method cannot be used for the whole stratosphere. To use the other two methods, "PV and U" and "U area," the wind speed criteria require the threshold value. Since the wind speed increases with height in the winter stratosphere, it is difficult to choose a threshold value applicable to the whole stratosphere. For these reasons, all three diagnostic methods are unsuitable for defining the vortex breakup in the upper stratosphere.

To observe the evolution of the upper-stratospheric polar vortex more closely, 4 days are selected to represent the important phases, 15 January, 10 February, 25 March, and 15 April, marked by red lines A–D, respectively, in Figure 3.4a. Their MPV distributions and gradients are exhibited in Figure 3.5. The edge of the vortex at 59°N on 15 January (Figures 3.5a, e) rapidly moves poleward and is located at 79°N on 10 February (Figures 3.5b, f). There is another maximum in the MPV gradient at 50°N (Figure 3.5b), and it moves poleward (Figure 3.4a). This second maximum in Figure 3.5b is not a vortex edge by the new definition at the present time, but it could grow to become a vortex edge. This second maximum also moved poleward and finally became an edge found at 61°N on 25 March (Figures 3.5c, g). By observing the absence of the vortex on 15 April (Figures 3.5d, h), the vortex broke up between 25 March and 15 April. If this is indeed the case, the breakup date of 28 April estimated using the "PV area" method would be too late. The subtropical edge shown in Figures 3.5d and 3.5h is discussed in the next section.

(a) MPV on 1260 K

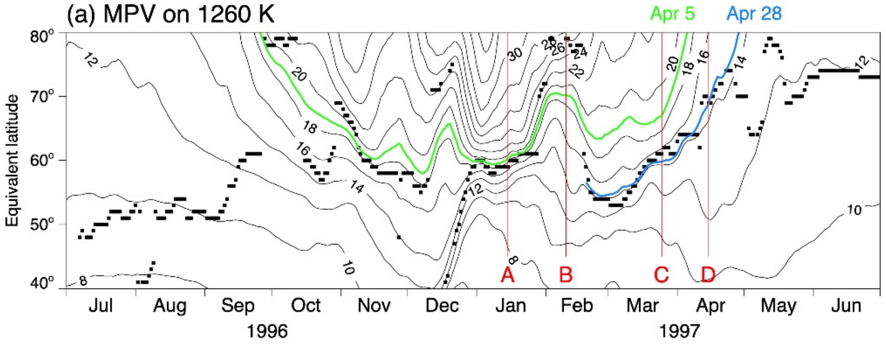

(b) MPV at the edge

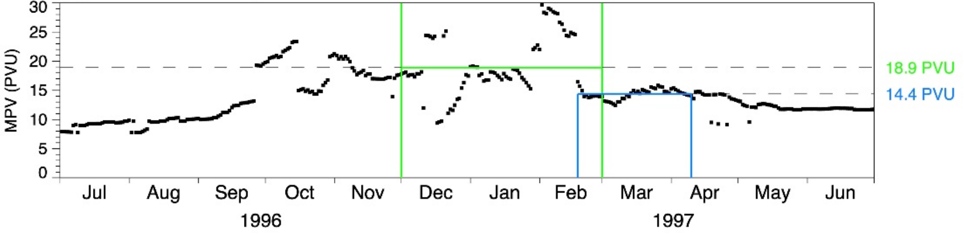

Figure 3.4 (a) Isolines of MPV (contours, PVU) over EL and time on the 1260 K isentropic surface in the NH for 1996–1997. The green and blue contours represent 18.9 and 14.4 PVU, respectively. The black squares indicate the edge of the polar vortex. The red vertical lines A, B, C, and D denote 15 January, 10 February, 25 March, and 15 April, 1997, respectively. (b) The black squares show the MPV at the vortex edge. The two horizontal dashed lines represent 18.9 and 14.4 PVU, respectively. The green vertical lines represent the 3-month winter period. The blue vertical lines represent the period from 18 February to 10 April.

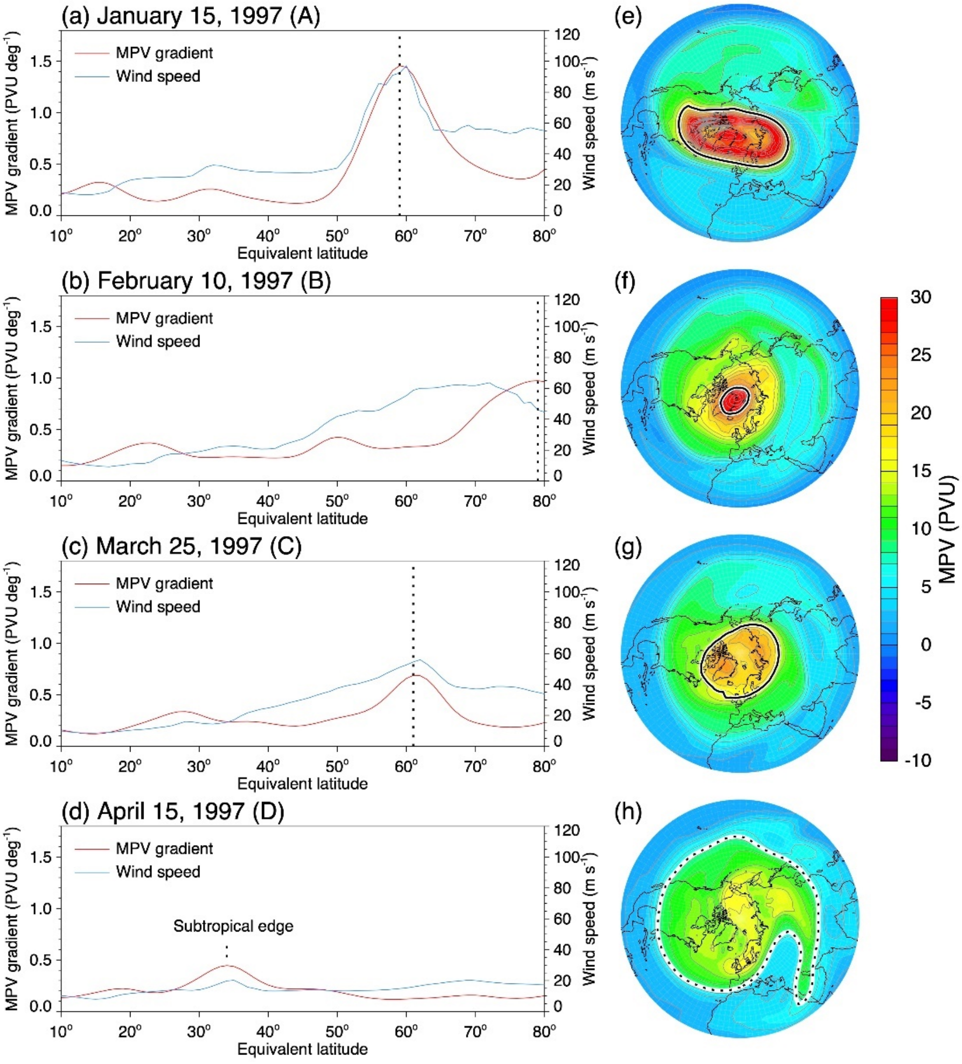

Figure 3.5 Same as in Figure 3.2 but on the 1260 K surface for (a) 15 January, (b) 10 February, (c) 25 March, and (d) 15 April, all in 1997, and (e)–(h) are their corresponding MPV fields. The location of the subtropical edge is marked by a dotted line in (d) and dotted contour in (h).

3.2. Edge-change Diagnostic for Polar Vortex

3.2.1. Edge-change metric

Difficulties in the application of the diagnostics described in previous section to the upper-stratospheric vortex generally arise from the varying dynamical properties of the polar vortex with respect to altitude. To find an alternative diagnostic for vortex breakup regardless of the altitude, features common to the polar vortex in both the lower and upper stratosphere need to be identified. In a similar sense, the features commonly observed during both the formation and breakup stages of the vortex should be considered. The mid-to-high latitudes are targeted here, since this study focuses on the breakup of the vortex. To see the vortex formation, its temporal evolution in the lower latitudes also needs to be observed.

Figure 3.6 shows the characteristic features of the vortex evolution, as in Figure 3.1 (same smoothing), but over the extended latitudinal range of 10°S–80°N in EL on the 1260 K isentropic surface. In addition to the vortex edge appearing in the polar region in winter, distinguishable edges are also seen in the subtropical region near 30°N in July 1996 and April–July 1997. These summertime edges are mainly determined by the maximum MPV gradient rather than by strong zonal winds. In general, quasi-horizontal mixing by wave breaking in winter strengthens the horizontal PV gradients at both the poleward and subtropical edges of the stirring zone (Polvani et al., 1995). The remnant of a wintertime subtropical edge could remain until summer (Nakamura and Ma, 1997; Neu et al., 2003). For example, a minor edge exhibited by the MPV gradient at 28°N on 25 March (Figures 3.5c, g) still remains on 15 April at 34°N (Figures 3.5d, h), and it appears in Figure 3.6 as a major edge after the polar vortex vanishes.

The EL of the daily vortex edge in Figure 3.6 shifts rapidly between the low and high latitudes, and this is more clearly seen in Figure 3.7a. The rapid shift from high to low latitudes in spring is associated with the vortex breakup, and the shift from low to high latitudes in autumn is associated with the vortex formation. Since the MPV and zonal wind speed at the polar vortex edge in Figures 3.7b and 3.7c are significantly greater than those at the tropical or subtropical edge, the MPV and wind speed at the edge in winter can be clearly distinguished from those in summer. Therefore, considering the parameters that are important for the existence of the polar vortex, such as high EL, large PV, and strong wind speed, the formation and breakup of the polar vortex could be characterized by the rapid increase and decrease of each variable at the edge, respectively. In other words, the formation and breakup of the polar vortex could be determined by detecting the peaks in the rate of temporal changes in EL, MPV, and wind speed at the edge. Therefore, here the temporal changes of these three parameters at the edge are utilized to define the dates of the polar vortex formation and breakup.

In calculations, the temporal change in the variables at the edge is obtained after using the 10-day running mean to reduce large day-to-day noise of each variable. The rate of change of each variable is normalized by its standard deviation for the entire period of data. Figure 3.7d shows the normalized rates of temporal changes of EL by the green line, MPV by the red line, and wind speed by the blue line at the edge. The dates of positive and negative peaks of each variable are generally in good agreement with each other. In Figure 3.7d, however, the opposite signs of peaks are observed between the wind speed and other variables in midwinter. In January and February 1997, the sign of peak wind speed is opposite to those of EL and MPV. The reason is that the maximum wind speed appears in middle latitudes in contrast to MPV, which increases with the latitude. As shown in Figure 3.6, wind speed decreases while the MPV increases during the poleward movement of the vortex edge in January, and that is the reason for the opposite signs of the variables in Figure 3.7d. During the vortex formation (breakup), however, the wind speed increases (decreases) rapidly; thus, all three variables show a common sign of the peaks. Since the size of the peaks is different depending on the variable, the three variables are combined together to detect the meaningful peaks in the time series rather than considering them all individually. Therefore, the values from three lines are averaged to obtain the dates of the maximum peaks (black line).

The positive and negative maximum peaks of the black line appear on 22 September, 1996, and 7 April, 1997, and these days are defined as the formation and breakup of the polar vortex, respectively. Considering the observations in Figure 3.5d, 7 April seems to be acceptable as a breakup date. Here the new method is named as the “edge-change” method and define the term “edge-change metric” as the values of the black line in Figure 3.7d. There are also several minor peaks in the average change rate that are due to intraseasonal variability in the strength and area of the polar vortex, associated with the upward propagation and breaking of the planetary waves. However, these minor peaks generally appear in midwinter and are distinguishable from the maximum peaks related to the formation and breakup of the vortex.

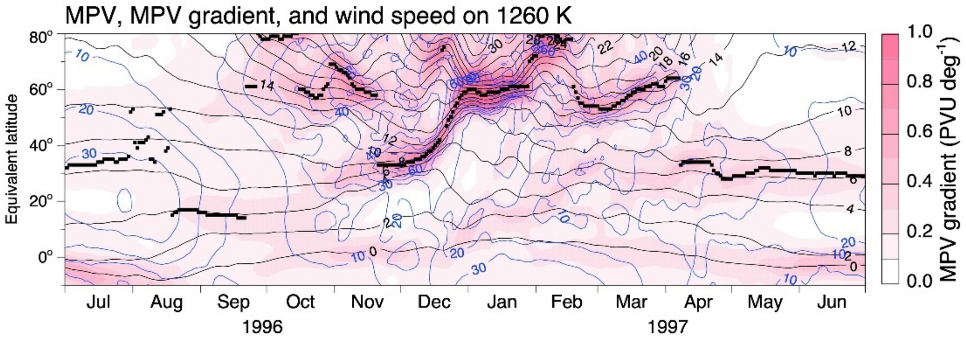

Figure 3.6 Isolines of MPV (contours, PVU) and its meridional gradient (red shading) in EL (10°S–80°N) and time on the 1260 K isentropic surface in the NH for 1996-1997. The blue contour represents the average wind speed (m s−1) along the MPV isoline. The black squares indicate the edge of the polar vortex.

(a) Equivalent latitude of the edge on 1260 K

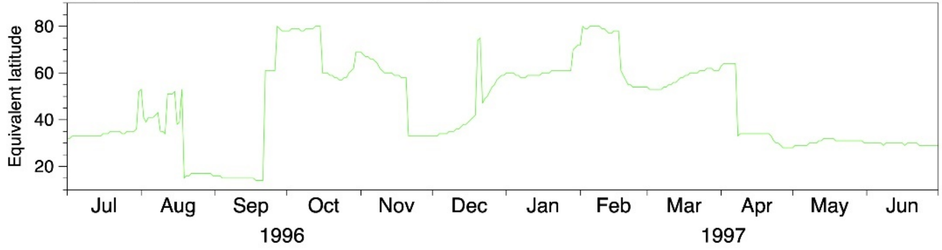

(b) MPV at the edge on 1260 K

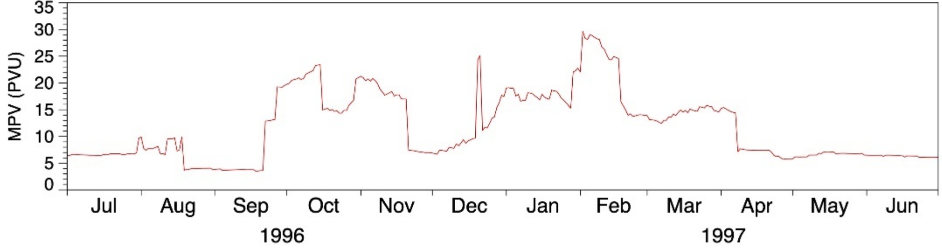

(c) Wind speed at the edge on 1260 K

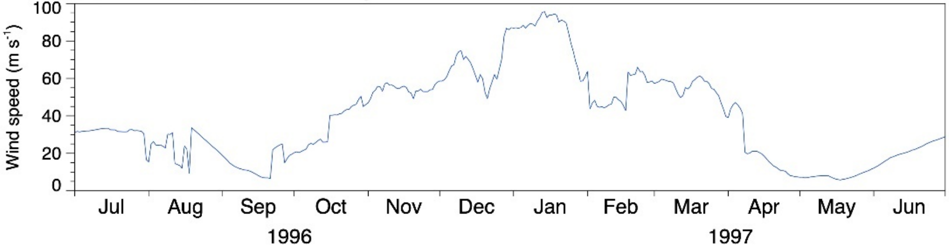

(d) Normalized rate of changes

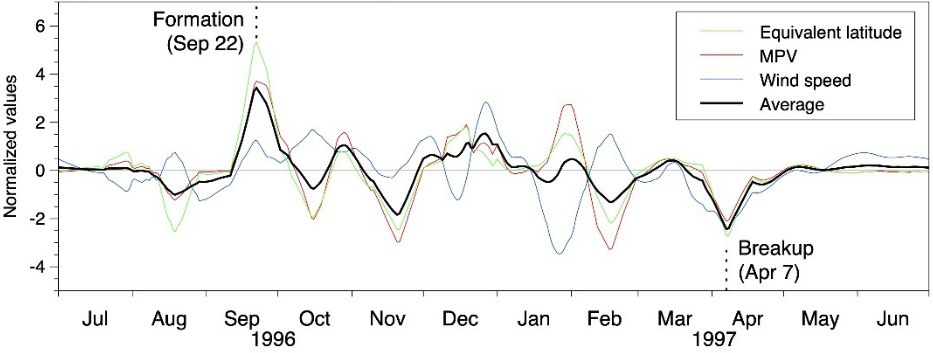

Figure 3.7 Changes in time of (a) EL at the vortex edge, (b) MPV, and (c) average wind speed along the MPV isoline at the vortex edge on the 1260 K surface, and (d) normalized changes of EL (green line), MPV (red line), and wind speed (blue line) and their average (black line) at the vortex edge.

3.2.2. Comparisons with conventional diagnostics

Determining the dates of the vortex formation and breakup by the “edge-change” method is possible for the lower stratosphere, where other diagnostics have been applied previously. Figure 3.8 shows a comparison of breakup dates of the NH polar vortices from 1979 to 2018, determined by the “edge-change” method defined in this study and the “PV area,” “PV and U,” and “U area” methods on the 510 K (~ 21 km) isentropic level. The interannual variability in the breakup dates in Figure 3.8 generally agrees well with Waugh et al. (1999) and Waugh and Polvani (2010), who showed the breakup dates of the NH polar vortices at 500 K. In addition, there are generally good agreements between the breakup dates from the “edge-change” method and the dates from the other three methods. Therefore, the “edge-change” method may be considered as providing similar results to those obtained by the other methods, for the lower stratosphere.

Note that there are some cases showing significant differences between the breakup dates. The years 2009 and 2013 are among them (red diamonds in Figure 3.8), and the major SSWs occurred in these two years (Harada et al., 2010; Nath et al., 2016). In these years, observing the evolution of the MPV distribution and the vortex edge, such as in Figure 3.9, would be useful to find the appropriate breakup date. The maximum negative peaks in the “edge-change” metric are found on 16 February in 2009 and 31 January in 2012, which are obviously associated with the SSW. In Figures 3.10 and 3.11, the polar vortex, which is split and weakened after the day of the maximum negative “edge-change” metric, recovers again and remains until the second negative peak days of 26 April 2009 and 3 May 2013. Therefore, choosing the next dates of the maximum rate of change, 26 April in 2009 and 3 May in 2012, would be more appropriate for determining the breakup dates, and those two dates are shown in Figure 3.8. To identify the NH vortex breakup day in an objective manner, the vortex breakup day is defined as the date of the negative peak “edge-change” metric after 1 March based on the observations in Figures 3.8 and 3.9. If there was no vortex edge after 1 March, the last day of the negative peak “edge-change” metric before March 1 would have been defined as the breakup date.

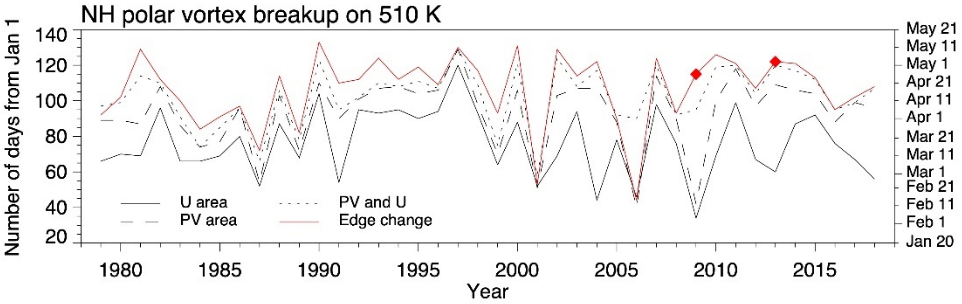

Figure 3.8 Comparison of polar vortex breakup dates in the NH on 510 K isentropic surfaces for the period 1979–2018 using the "PV and U," "U area," "PV area," and "edge-change" criteria. The red diamonds denote the years 2009 and 2013.

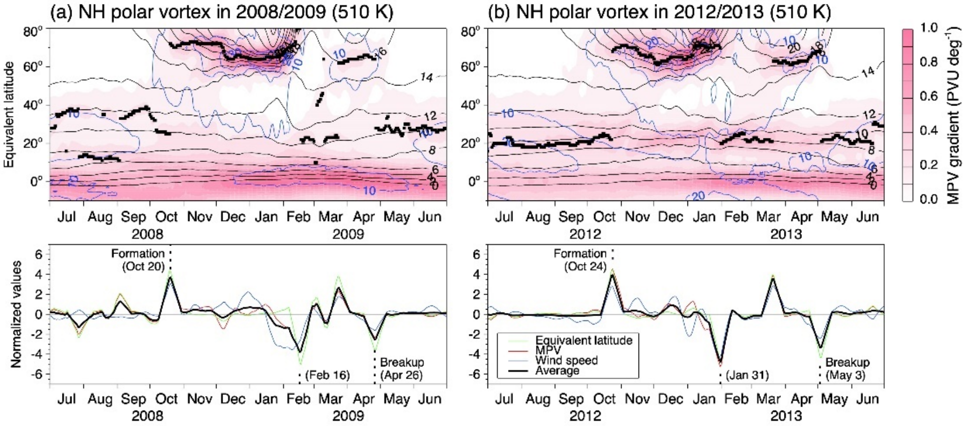

Figure 3.9 Isolines of MPV (contours, PVU) and its meridional gradient (red shading) in EL (10°S–80°N) and time on the 510 K isentropic surface (upper panels) and normalized changes of EL, MPV, and wind speed and their average in the NH (lower panels) for (a) 2008-2009 and (b) 2012-2013. The blue contour represents the average wind speed (m s^{-1}) along the MPV isoline. The black squares indicate the edge of the polar vortex.

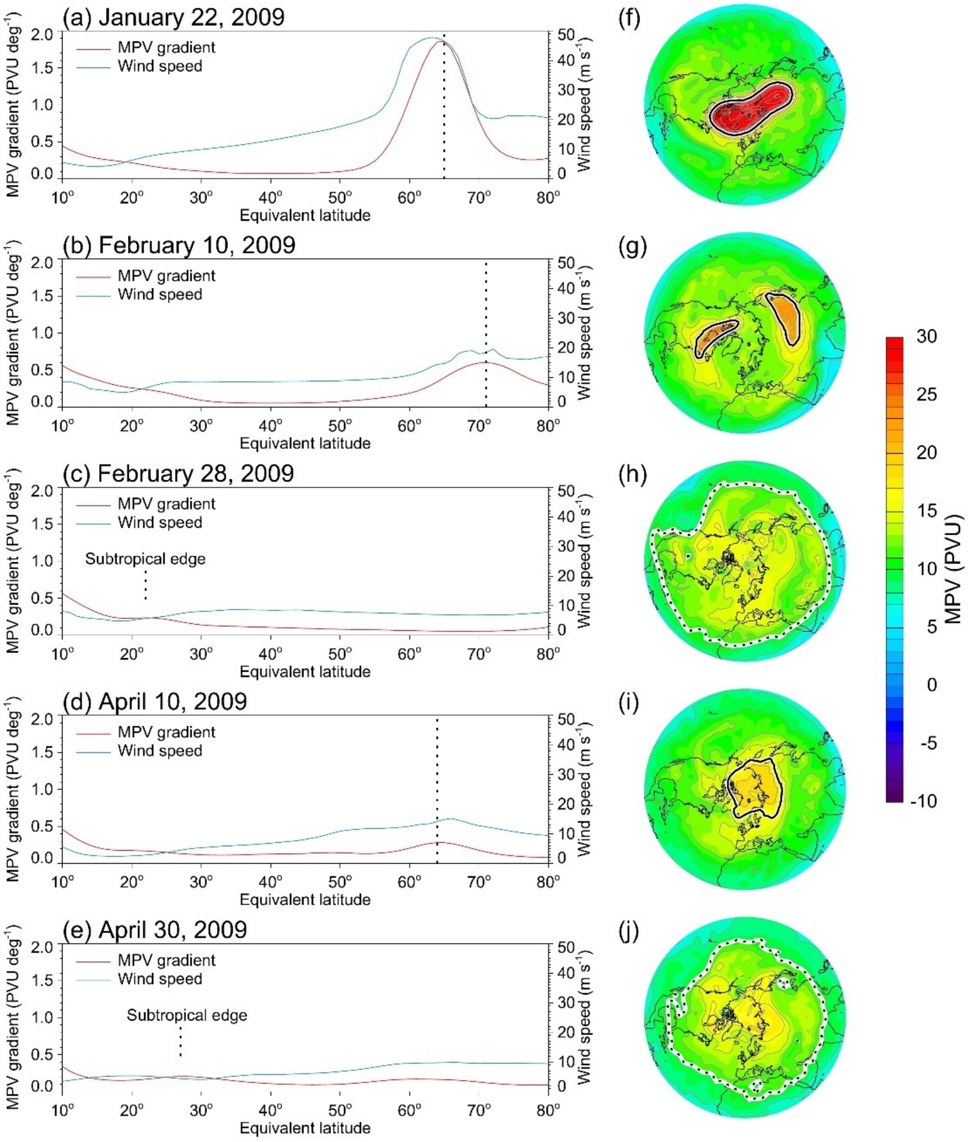

Figure 3.10 Same as in Figure 3.2 but on the 510 K surface on (a) 22 January, 2009, (b) 10 February, 2009, (c) 28 February, 2009, (d) 10 April, 2009, and (e) 30 April, 2009, and in the right panel their corresponding MPV fields (f), (g), (h), (i), and (j) for the same dates, respectively. Location of the vortex edge on each day is marked by a dotted line in the left panel and a thick black solid contour in the right panel. Location of the subtropical edge is marked by a dotted line in (c) and (e) and dotted contour in (h).

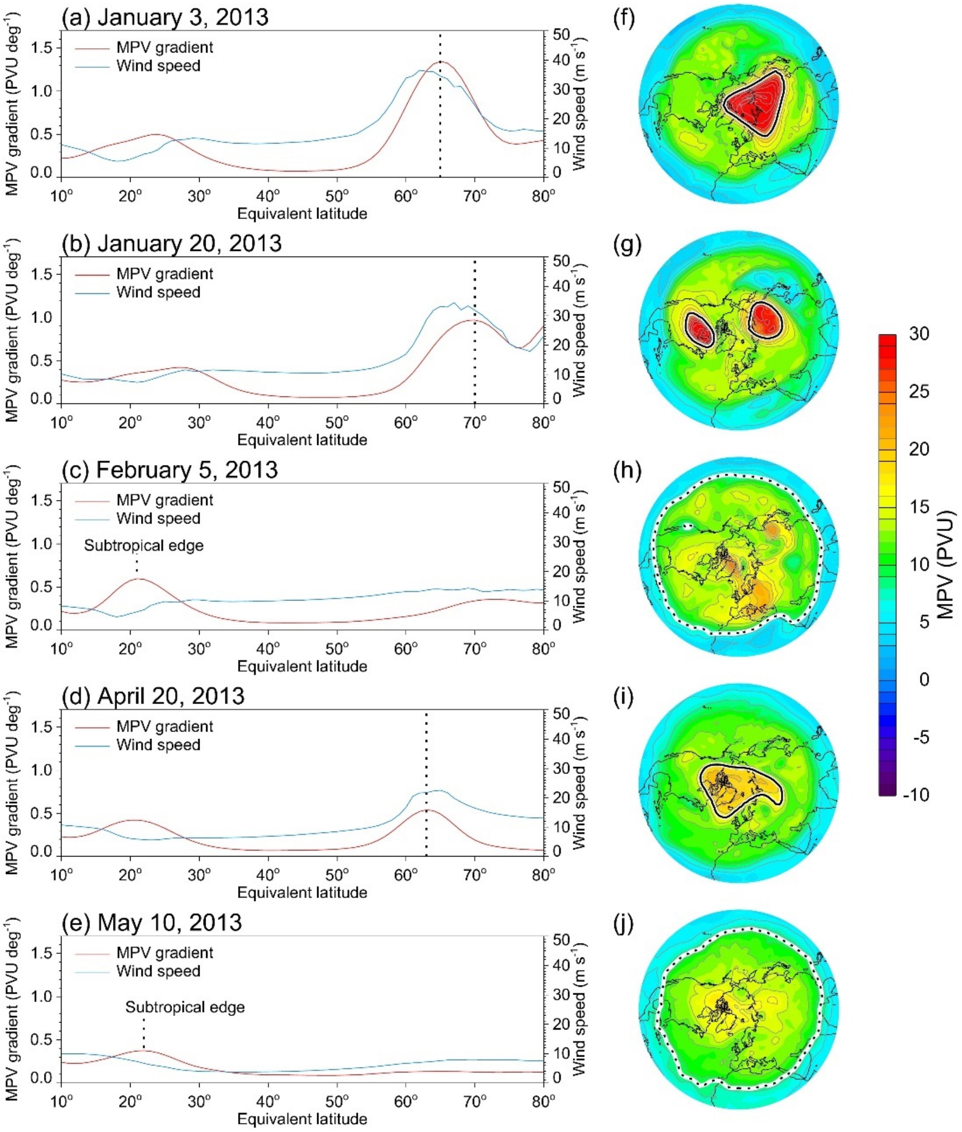

Figure 3.11 Same as in Figure 3.2 but on the 510 K surface on (a) 3 January, 2013, (b) 20 January, 2013, (c) 5 February, 2013, (d) 20 April, 2013, and (e) 10 May, 2013, and in the right panel their corresponding MPV fields (f), (g), (h), (i), and (j) for the same dates, respectively.

3.2.3. Application of edge-change diagnostic

An advantage of the “edge-change” method is that a consistent determination can be made for the formation and breakup dates of the polar vortex regardless of altitude. Figure 3.12 shows the vertical profiles of the formation and breakup dates from 430 K (~ 16 km) to 1260 K (~41 km) of the NH and SH polar vortex for the period 1979–2018. In general, the formation and breakup of the polar vortex occur earlier in the upper stratosphere and later in the lower stratosphere. This downward propagation of the formation- and breakup-timing of the polar vortex has been reported in several studies (Manney and Sabutis, 2000; Choi et al., 2002a; Hardiman et al., 2011). The formation and breakup dates show different characteristics in each hemisphere. In the NH, the polar vortex first formed late in September at 1260 K, and the formation took about 116 days until it arrived in mid-January at 430 K (Figure 3.12a). The breakup of the NH polar vortex, however, took only approximately 35 days on average with large year-to-year variability in its vertical profiles (Figure 3.12b). In the SH, the vortex formation from 1260 K to 430 K took 92 days on average between early March and mid-April, which is much shorter than that in the NH (Figure 3.12c). The breakup of the SH polar vortex (Figure 3.12d) took about 67 days covering the same altitude range. This is longer than the breakup of the NH vortex, and it also shows less interannual variability.

Figure 3.13 shows the time series of the polar vortex breakup dates determined by the “edge-change” method for two isentropic levels, 1260 K and 510 K, for the period 1979–2018. In the SH, linear trends are drawn before and after 2000 in Figures 3.13b and 3.13c. The year 2000 is subjectively chosen. Vortex breakup in the SH has been delaying in the lower stratosphere until around 2000, with a statistically significant linear trend at a 95 % confidence level (p = 0.018). After 2000, a small and statistically insignificant trend is exhibited in the vortex breakup date in Figure 3.13d. The trends before and after 2000 may be associated with the depletion and recovery of the Antarctic ozone layer. In their Figure 6, Langematz and Kunze (2006) showed a significant change in the trend of the spring changeover around 2000 in the SH. Zambri et al. (2021) reported that the Antarctic column ozone in November decreased during 1979–2001 (−47 DU decade^{-1}) but started to recover after 2001 (+24 DU decade^{-1}). The trend in the upper stratosphere is of the opposite sign until around 2000, although it is statistically insignificant. There is no significant decadal trend in the NH vortex breakup dates.

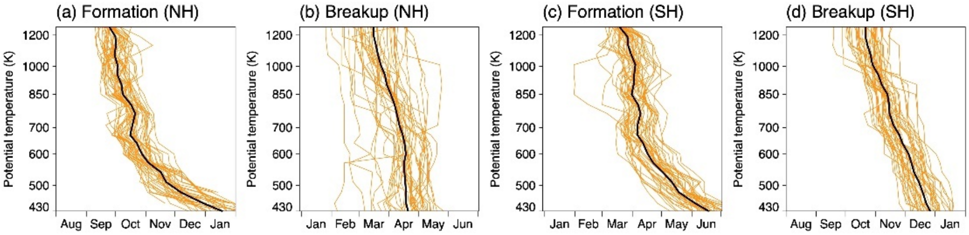

Figure 3.12 The dates of the formation and breakup of the NH and SH polar vortex (orange line) and their average (thick black line) from 430 K to 1260 K for the period 1979–2018.

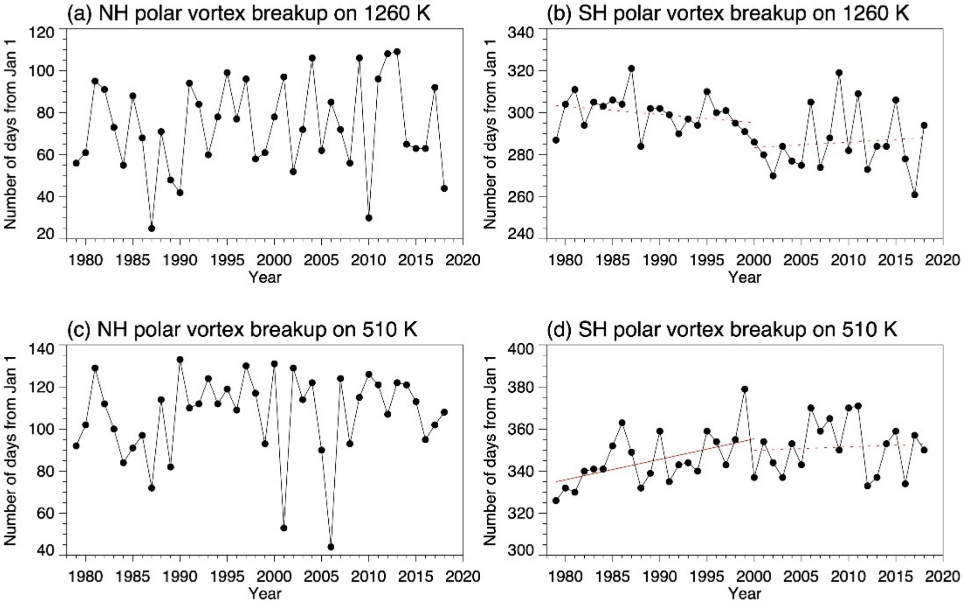

Figure 3.13 The black solid lines denote the vortex breakup dates determined by the "edge-change" method at (a) 1260 K in NH, (b) 1260 K in SH, (c) 510 K in NH, and (d) 510 K in SH for the period 1979–2018. The red solid and dotted lines in (b) and (d) are the linear trends for 1979–2000 and 2000–2018, respectively. The red solid line is statistically significant at the 95% confidence level ($p = 0.018$).

3.3. Validation of Edge-change Diagnostic

3.3.1. Breakup of polar vortex and SFW

Dates of the polar vortex breakup constitute a good diagnostic for studying interannual climate change, specifically by analyzing the vortex evolution. Another diagnostic for understanding the vortex evolution is the SFW. As was stated in the Introduction, the SFW is defined as the event followed by the transition from the usual winter to the summer stratospheric conditions (Andrews et al., 1987). The date of the SFW is easier to define than the breakup date, particularly in the upper stratosphere, since only the zonal wind is used for defining the SFW. The vortex breakup dates defined in this study are shown in Figure 3.14 along with the SFW dates, for 430 K to 1260 K. The date of the SFW is defined when the zonal-mean zonal wind falls below zero without returning above a threshold value until the subsequent autumn (Black et al., 2006). The threshold value must be prescribed, and Black et al. (2006) used 5 m s^{-1} at 50 hPa and 10 m s^{-1} at 10 hPa. The zonal-mean zonal wind in Figure 3.14 was smoothed using a 5-day running mean and averaged between 60°N and 80°N.

The dates of the SFW in NH using both the 5 m s^{-1} and 10 m s^{-1} threshold values are shown in Figure 3.14. In Figure 3.14, the SFW date by the 10 m s^{-1} threshold is represented by a green diamond. The SFW date by the 5 m s^{-1} threshold is shown by a yellow square only when the two SFW dates by the different thresholds are not identical. The date of the SFW is generally not very sensitive to the choice of the threshold value. When the SSW occurs, however, determining the SFW date can be significantly affected by the threshold value, e.g., for the case in 2001 and 2002 (See the list of the SSW events in Table 1 of Choi et al., 2019). In 2001, on the 760 K surface, the estimated SFW date with the 10 m s^{-1} threshold is found to be 2 February, while the date would be 13 May if the threshold were 5 m s^{-1}. In 1999 and 2000, the SFW dates in the upper stratosphere are also sensitive to the choice of the threshold value.

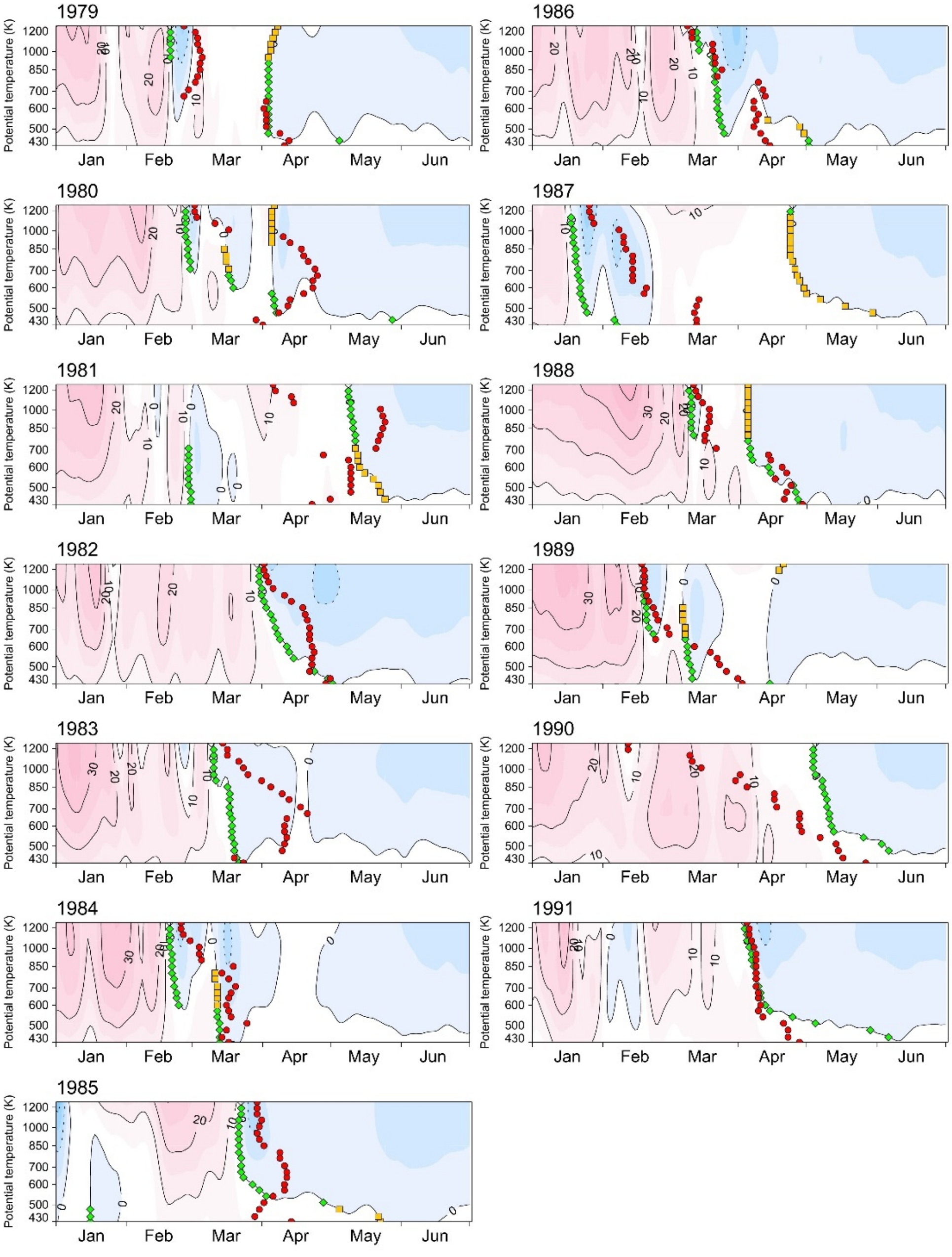

Figure 3.14 Zonal-mean zonal wind (m s^{-1}) from 430 K to 1260 K averaged from 60°N to 80°N for the period 1979–2018. The red circles and green diamonds denote the dates of the vortex breakup obtained by the "edge-change" method and the SFW defined by the 10 m s^{-1} threshold, respectively. The yellow squares denote the SFW defined by the 5 m s^{-1} threshold.

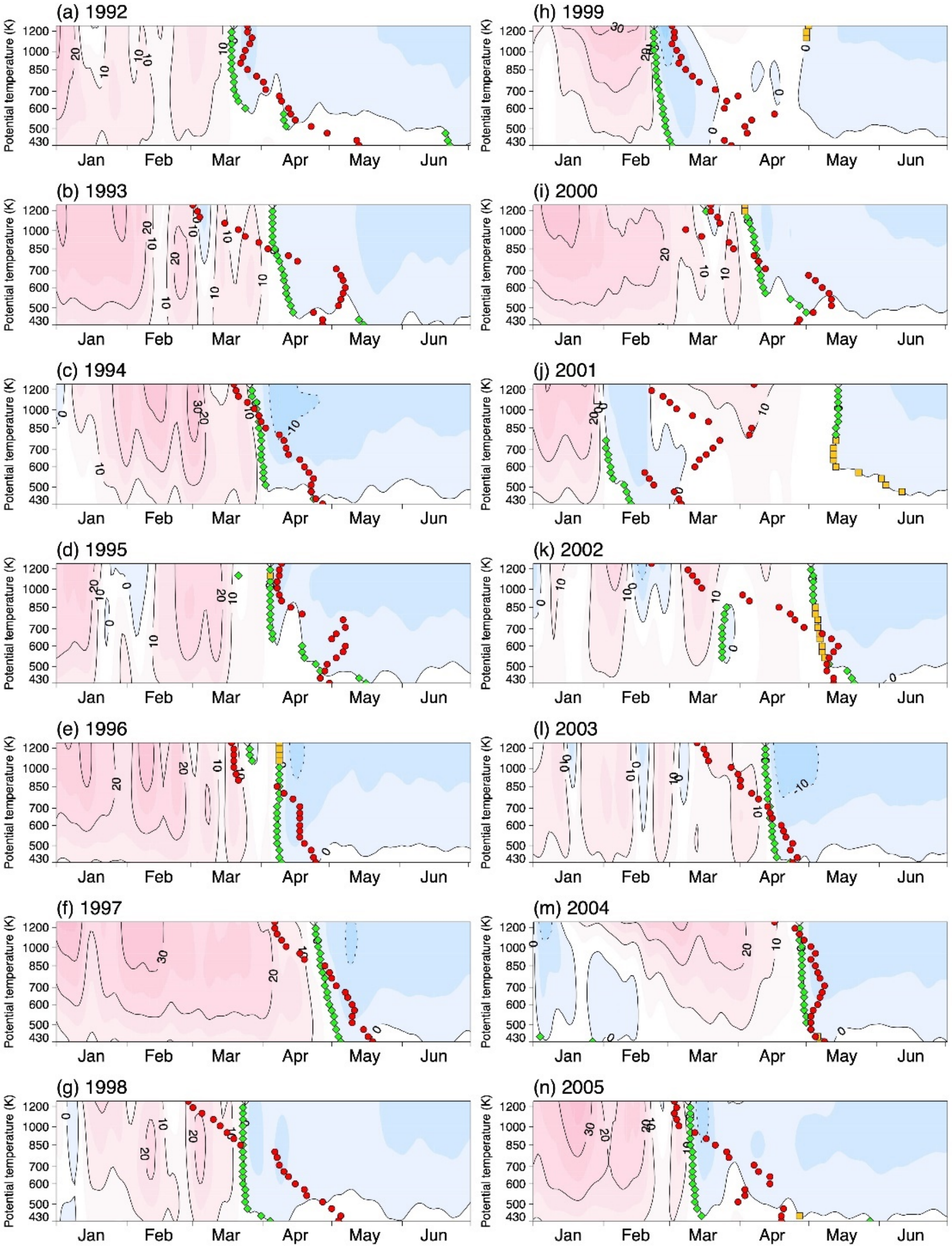

Figure 3.14 (Continued)

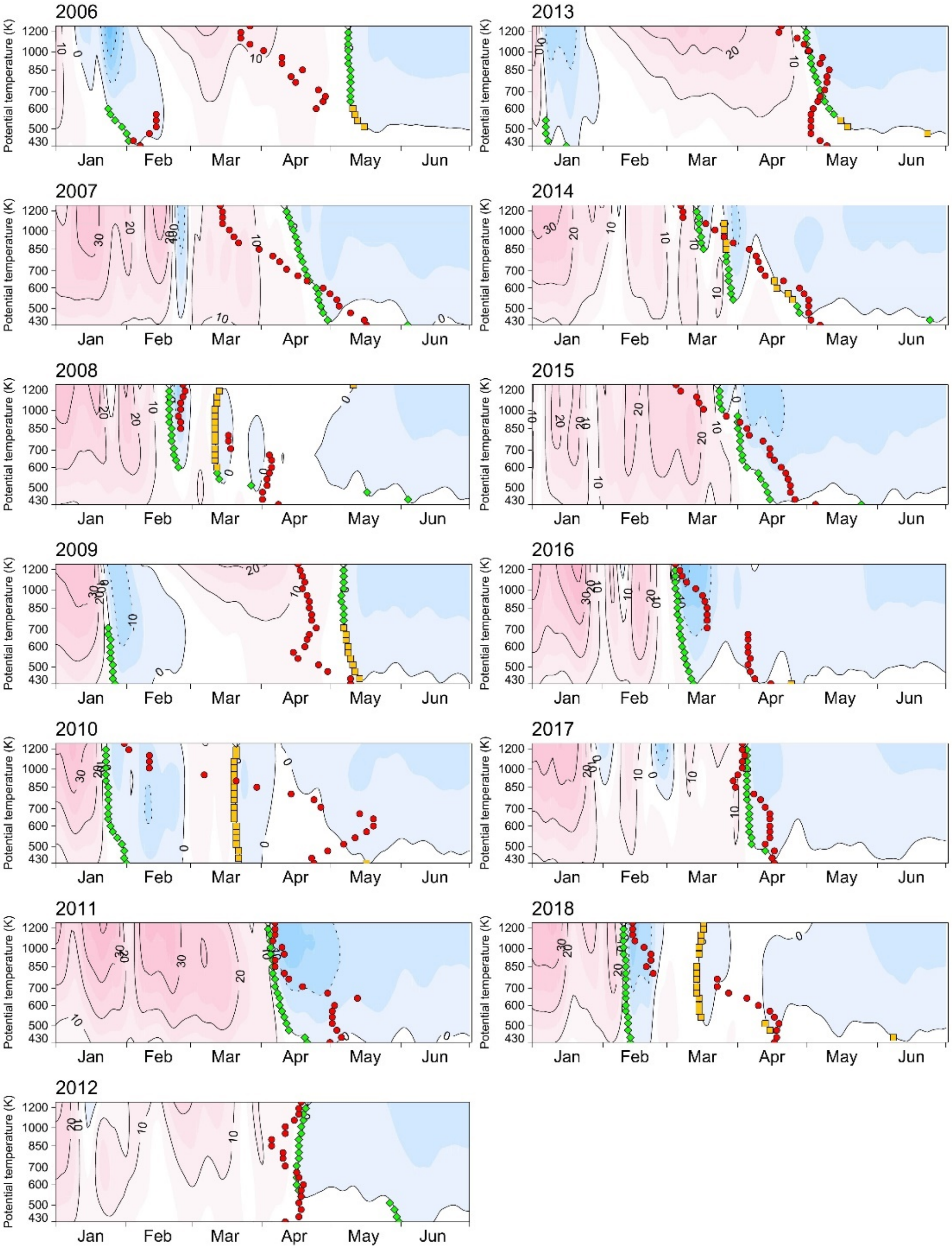

Figure 3.14 (Continued)

3.4.2. Tracer distributions

Mixing ratios of long-lived tracers, such as CH_4 and N_2O, exhibit large differences before and after the vortex breakup (Choi et al., 2002a), associated with irreversible mixing. Thus, the new definition of the vortex breakup date can be evaluated using the evolution of the tracer concentrations. Figure 3.15 shows the temporal evolution of the CH_4 and O_3 mixing ratios observed by ILAS from 1 November 1996 through 30 June 1997 on the isentropic levels of 1260 K (~ 41 km), 800 K (~ 32 km), and 450 K (~ 17 km). High and low mixing ratios of CH_4 and O_3, represented by the color scale, exhibit the boundary of the polar vortex fairly well. In the lower stratosphere (at the 450 K level), significantly high mixing ratios are observed inside the vortex. This is due to a weaker transport barrier in the lower stratosphere than in the mid-stratosphere (800 K), as shown by Haynes and Shuckburgh (2000) using the effective diffusivity. The EL at which the mixing ratio discontinuity appears generally agrees well with the vortex edge defined dynamically, even in the upper stratosphere. These distinctive differences in CH_4 and O_3 across the edge of the polar vortex do not appear after the breakup date, and the tracers have a uniformly well-mixed distribution from low to high latitudes.

Significant discontinuities of tracer concentrations across the vortex edge in EL (Figure 3.15) can also be observed on the same latitude circle (Choi et al., 2002a), which show large and small mixing ratios outside and inside the vortex, respectively. After the vortex breakup, the tracer mixing ratio has relatively similar values following the latitude circle due to the absence of the vortex edge. Thus, another diagnostic for the vortex breakup might be the standard deviation of the tracer mixing ratio following the latitude circle, which decreases significantly afterwards. The date of the vortex breakup at each level is shown by red dots in Figure 3.16, along with the standard deviations of the CH_4, N_2O, H_2O, and O_3 mixing ratios. The breakup dates distinguish between the high and low standard deviations before and after, and this implies the mixing of air from inside and outside the vortex and subsequent disappearance of the vortex edge.

To observe vortex formations and breakups over a longer time period, the O_3 mixing ratio was obtained from POAM II and POAM III in addition to the ILAS data. The standard deviation of the O_3 mixing ratio from the combined POAM II, ILAS, and POAM III data is shown in order in Figures 3.17 and 3.18. The formation and breakup dates are generally in good agreement with the high and low daily maximum MPV as well as the high and low zonal standard deviation of O_3, respectively. In Figure 3.14, an exceptionally early breakup date in February 2001 is estimated in the lower stratosphere. When comparing with the O_3 standard deviation in Figure 3.17, the early vortex breakup date appears to be consistent with the evolution of the O_3 concentration. Considering the observed features of tracer concentrations discussed in this section, the definition of vortex formation and breakup using the “edge-change” method seems to be well supported by their distribution and evolution.

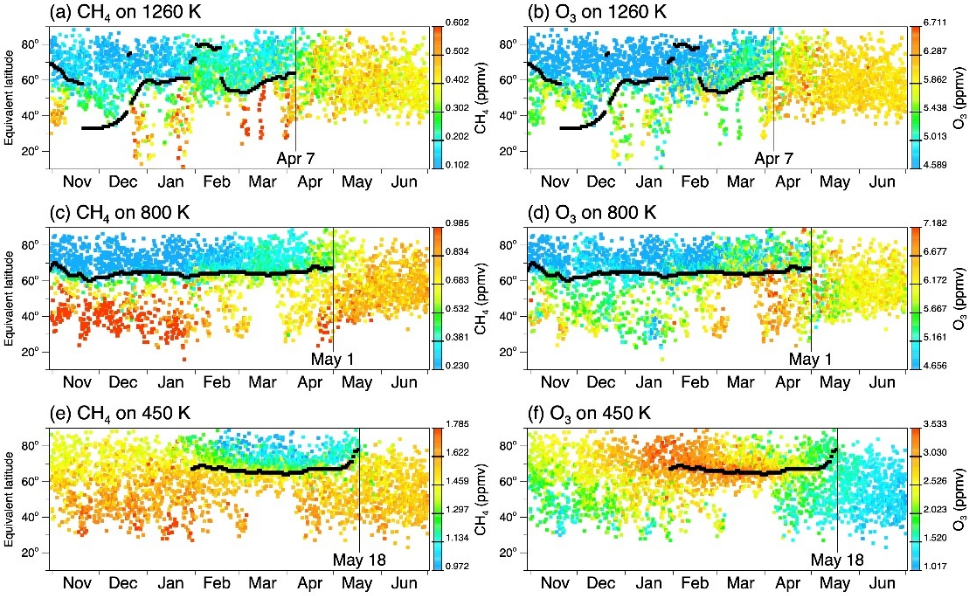

Figure 3.15 CH$_4$ and O$_3$ mixing ratios observed by ILAS in EL and time on the 1260 K, 800 K, and 450 K isentropic surfaces in the NH from 1 November, 1996, to 30 June, 1997. The black square denotes the location of the vortex edge each day, and the vertical line represents the date of the polar vortex breakup using the "edge-change" method.

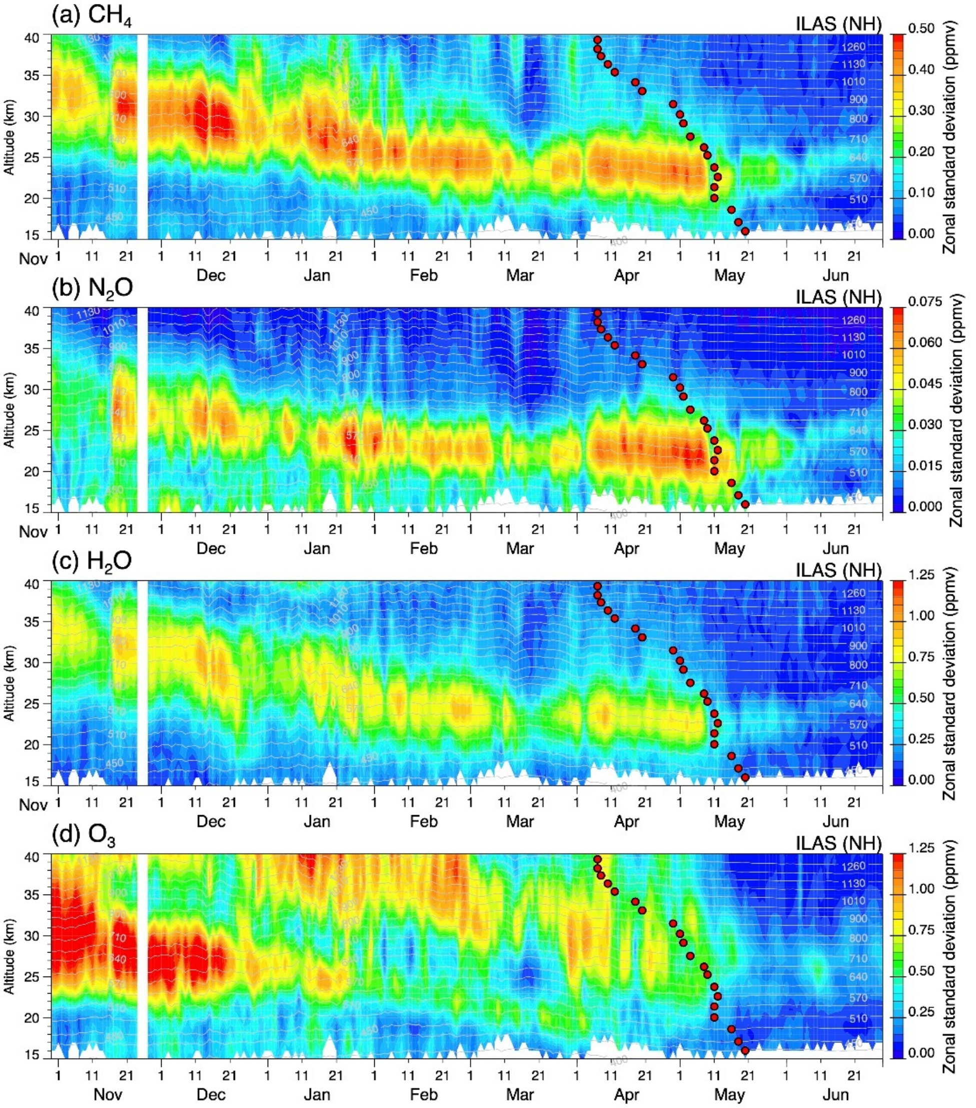

Figure 3.16 Standard deviation of the mixing ratios of (a) CH$_4$, (b) N$_2$O, (c) H$_2$O, and (d) O$_3$ following the latitude circle from the ILAS observations from 1 November, 1996, to 30 June, 1997. The gray isolines represent the potential temperature, and the red solid circle denotes the date of the polar vortex breakup on each isentropic surface using the “edge-change” method.

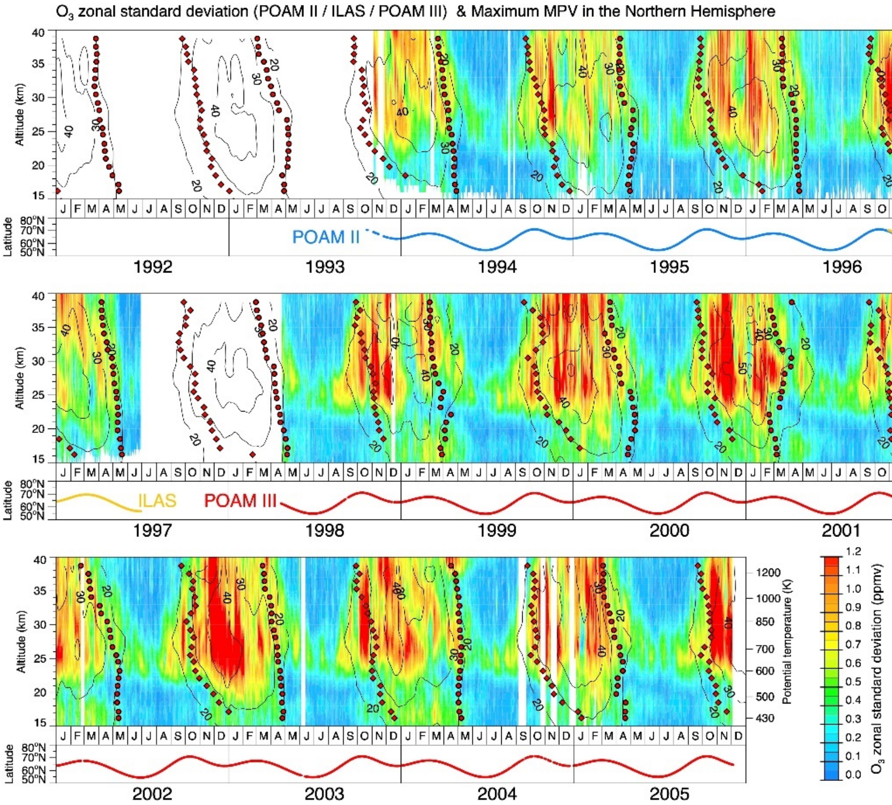

Figure 3.17 Standard deviation of the O$_3$ mixing ratio (denoted by color shading) following the latitude circle from the POAM II (October 1993–November 1996), ILAS (November 1996–June 1997), and POAM III (April 1998–November 2005) observations, and the daily maximum MPV (10^{-6} K m^2 kg^{-1} s^{-1}; denoted by contours) on each isentropic surface in the NH for the period 1992–2005. The red solid diamonds and circles denote the dates of the formation and breakup of the polar vortex, respectively. In the lower part of each panel, the latitudes of the POAM II, ILAS, and POAM III observations are represented by blue, yellow, and red lines, respectively.

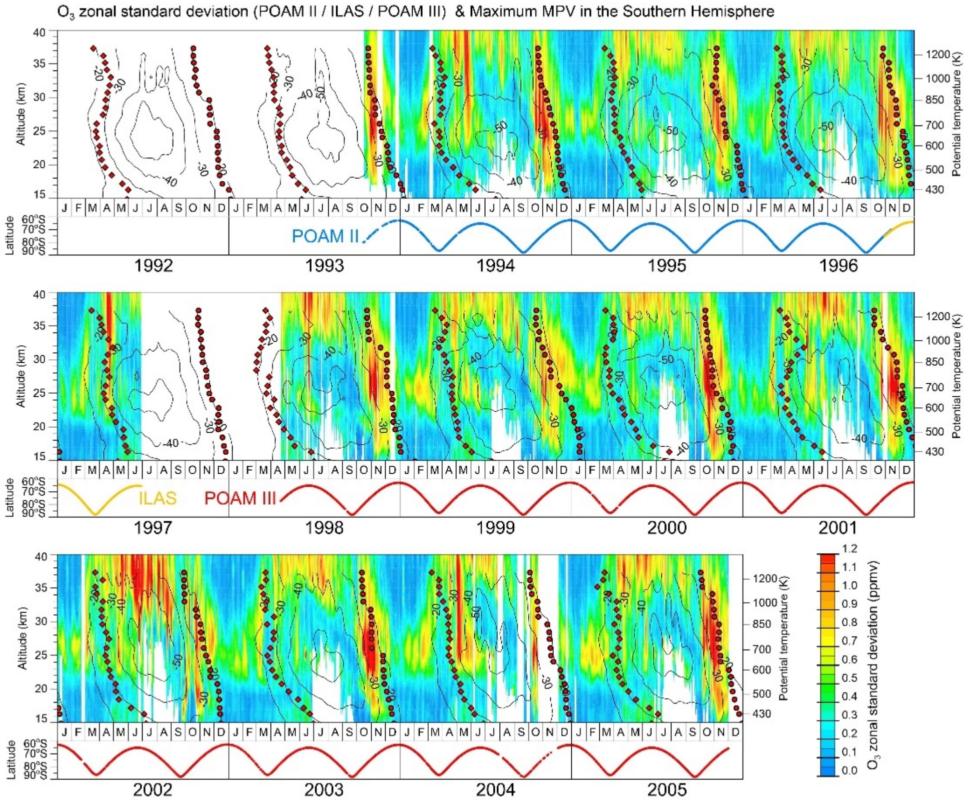

Figure 3.18 Same as in Figure 3.17 but for the SH. The contour lines represent the daily minimum MPV on each isentropic surface.

4. Stratospheric Planetary Waves in NH Spring

4.1. Interannual Variability in Planetary Waves

4.1.1. Climatological characteristics

In terms of planetary wave analysis, zonal asymmetry of dynamic fields is represented by perturbation fields from the zonal-mean. The GPH zonal anomaly (Z') from the zonal-mean GPH ($\bar{Z}$) at a given latitude and level can be expanded in zonal Fourier harmonics up to a certain wavenumber s that is limited by the resolution of data as follows (Andrews et al., 1987):

$$Z'(\lambda, t) = Z(\lambda, t) - \bar{Z}(t) = \sum_{s=1}^{S} Z_s(t)\cos[s\lambda + \alpha_s(t)]$$

where λ is longitude, and Z_s and α_s are amplitude and phase of the wavenumber s, respectively. Vertically propagating planetary waves can only exist in the westerly winds weaker than the Rossby critical velocity, which is inversely proportional to the squared zonal wavenumber. Therefore, the stationary disturbance in the winter stratosphere is dominated by the ultra-long planetary waves. In this study, the GPH wave-1 amplitude (Z_1) was mainly investigated.

Monthly climatological averages of the wave-1 amplitudes of GPH are represented in Figure 4.1. The wave-1 show their maximum at the high-latitude upper stratosphere (~70°N for wave-1, above 5 hPa). Since the monthly maximum wave-2 amplitudes are more or less than one-third of the monthly maximum wave-1 amplitudes, this study focused on the wave-1 component of the planetary waves in the high-latitudes (cosine-weighted average over 60–80°N) upper stratosphere (3 hPa). It should be noted that the coefficient of variation (ratio of the interannual standard deviation to the climatological mean) of the wave-1 amplitude in the high-amplitude region is the largest in March (larger than 40%), albeit the much smaller amplitude compared to the mid-winter months (DJF).

Figures 4.2a and 4.2c show the monthly mean wave-1 amplitude of the GPH, denoted by Z_1, in the NH (20–90°N). The maximum amplitude of wave-1 was located at 70°N, between 3 and 10 hPa vertically. The wave-1 amplitudes in March were much larger in 1994 than 1995. Zonal-mean zonal winds (Figures 4.2b and 4.2d) are shown in the tropical region from 35°S to 35°N in March 1994 and 1995. Significant differences in the zonal wind were found between 1994 and 1995 in the tropical stratosphere. In the mid-stratosphere from 30 to 10 hPa, the equatorial zonal winds were easterlies in March 1994 and westerlies in March 1995 due to the presence of the QBO. Figure 4.2 shows the relationship between the equatorial zonal wind at 10 hPa and high-latitude Z_1 at 3 hPa, in which the large amplitude Z_1 was associated with the equatorial easterly in March, at least for these 2 years. Although many studies have used the equatorial wind at 50 hPa for studying the relationship between the high latitudes and QBO, other studies reported QBO-related changes in high latitudes due the influence of the middle and upper-stratospheric equatorial zonal wind (Gray et al., 2001; Gray, 2003; Yamashita et al., 2011). Because the aim of this study was to investigate upper-stratospheric planetary waves, 10 hPa was chosen to represent the phase of the QBO instead of 50 hPa.

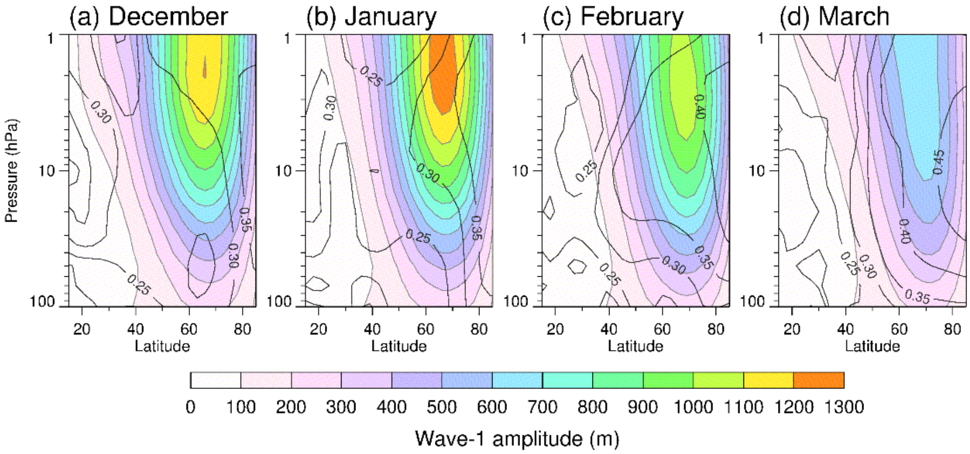

Figure 4.1 Monthly climatological averages of the GPH wave-1 amplitude from December to March (color scale) and its coefficients of variation (standard deviation to the mean; contours with intervals of 0.05) for the period of 1979–2019.

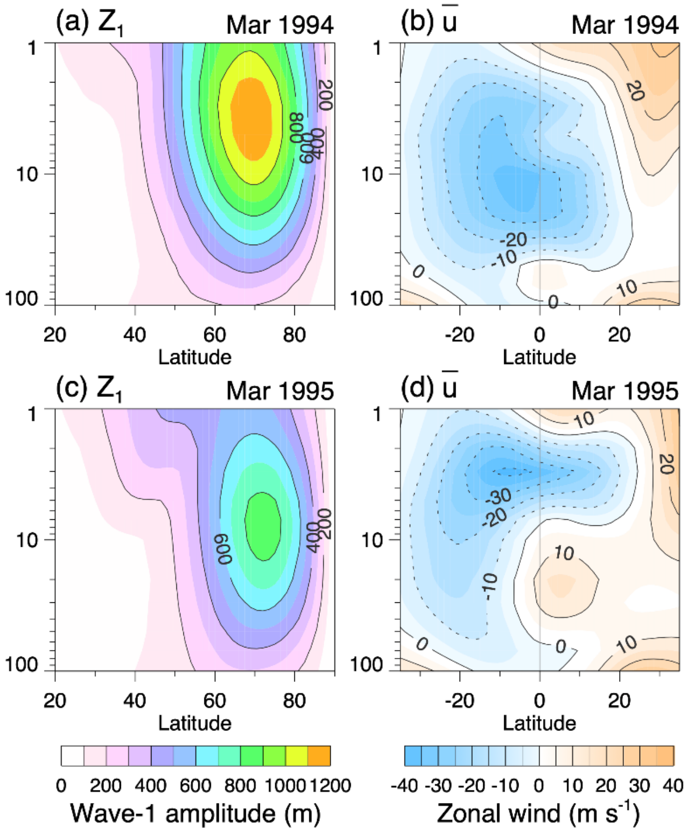

Figure 4.2 (a), (c) Monthly mean wave-1 amplitude of the daily GPH in the NH, and (b), (d) zonal-mean zonal wind in the low-latitude region in March 1994 (upper panels) and 1995 (lower panels).

4.1.2. Interannual variability in wave-1 amplitude and QBO

To determine if the above relationship was present in other years, scatter plots of Z_1 in high latitudes (averaged over 60–80°N at 3 hPa) versus the equatorial zonal-mean zonal wind (averaged over 5°S–5°N at 10 hPa) were created (Figure 4.3). Hereafter, the easterly and westerly phase of the QBO at 10 hPa are referred to as QBOe and QBOw, respectively. In Figure 4.3, during the whole study period, there was no significant difference in Z_1 between the QBO phases in all 3 months. When the data were grouped based on the magnitude of the Z_1 amplitude compared to the climatological mean, a significant difference appeared in March. Because this study was interested in the development of wave amplitude, grouping the data into large and small Z_1 amplitude years, denoted by (L) and (S), respectively, was a reasonable approach. The climatological means are summarized in Table 4.1. In January, the large-amplitude group, with a climatological mean of 1,420 m for QBOe and 1,412 m for QBOw, displayed small differences between QBO phases. In February, the large-amplitude averages were 1,285 and 1,231 m for QBOe and QBOw, respectively; this was a statistically insignificant difference. In March, however, as shown in Figure 4.3d, the amplitude for the large-amplitude groups displayed large differences between QBO phases. The average amplitudes were 918 and 698 m for QBOe and QBOw, respectively (Table 4.1).

The average amplitudes for all years in December, January, and February were 1,072 m, 1,151 m, and 989 m, respectively, which were much larger than the 622 m in March. Therefore, it seems that the upward-propagating planetary wave activities are much higher in DJF than March. A similar QBO influence on the high-latitude planetary waves during the 3 months might have been masked by stronger planetary wave activities propagating upward in DJF. Only in March, in which there was no strong background wave activities, could the effect of forcing induced by the QBO on planetary wave activities be observed.

To examine the differences in wave amplitudes more closely, Figure 4.4 shows the composite difference of wave-1 amplitude between QBOe and QBOw years. The composite difference in wave-1 amplitude was large in January compared to February and March, as expected from Table 4.1. The amplitude difference in January was mostly attributable to the difference in small-amplitude years. In large-amplitude years (Figure 4.4b), statistically significant differences were found over a wide area of the extratropical stratosphere in March.

Previous studies indicated that the interannual variability in tropospheric forcing like the ENSO also has a large effect on the polar stratosphere (e.g., Garfinkel and Hartmann, 2007). However, scatter plots between the monthly mean high-latitude wave-1 amplitude at 3 hPa and the preceding three-month averages of Niño 3.4 SST anomalies do not show any statistically significant linear relationships nor the asymmetric distribution to the phase of the QBO (Figure 4.5). Therefore, this study could exclude the potential effect of the ENSO on the QBO-extratropical relationship in the upper stratosphere.

Table 4.1 Averages of the high-latitude monthly mean wave-1 amplitude at 3 hPa for the large-amplitude group (L), small-amplitude group (S), and total years for QBOe and QBOw. Climatological averages of the high-latitude wave-1 amplitude and numbers of years for each group (N) are additionally represented in the table. Composite difference between QBOe and QBOw is statistically significant only for the large-amplitude groups in March ($p <$ 0.001; denoted by the bold characters).

Months	January (Clim. Avg. = 1151 m)		February (Clim. Avg. = 989 m)		March (Clim. Avg. = 622 m)	
	QBOe	QBOw	QBOe	QBOw	QBOe	QBOw
Large-amplitude groups	1420 m (N = 16)	1412 m (N = 7)	1285 m (N = 14)	1231 m (N = 8)	**918 m** (N = 12)	**698 m** (N = 10)
Small-amplitude groups	893 m (N = 8)	702 m (N = 9)	701 m (N = 11)	576 m (N = 7)	379 m (N = 13)	398 m (N = 5)
Total averages	1244 m (N = 24)	1012 m (N = 16)	1028 m (N = 25)	925 m (N=15)	638 m (N = 25)	598 m (N = 15)

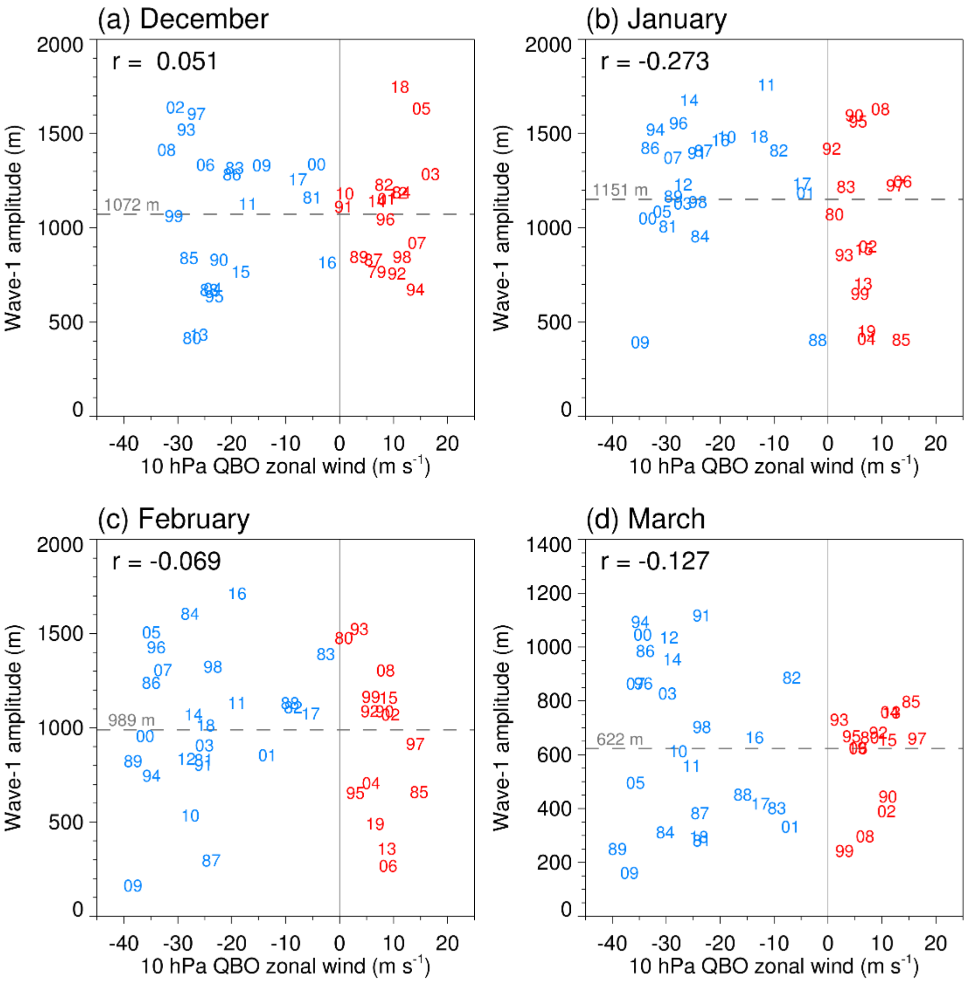

Figure 4.3 Scatter plots of the high-latitude Z_1 at 3 hPa versus equatorial $\bar{u}$ at 10 hPa in (a) January, (b) February, and (c) March for the period 1980–2019. The blue and red numbers denote QBOe and QBOw years, respectively. Horizontal dashed lines represent the climatological mean of Z_1 for each month.

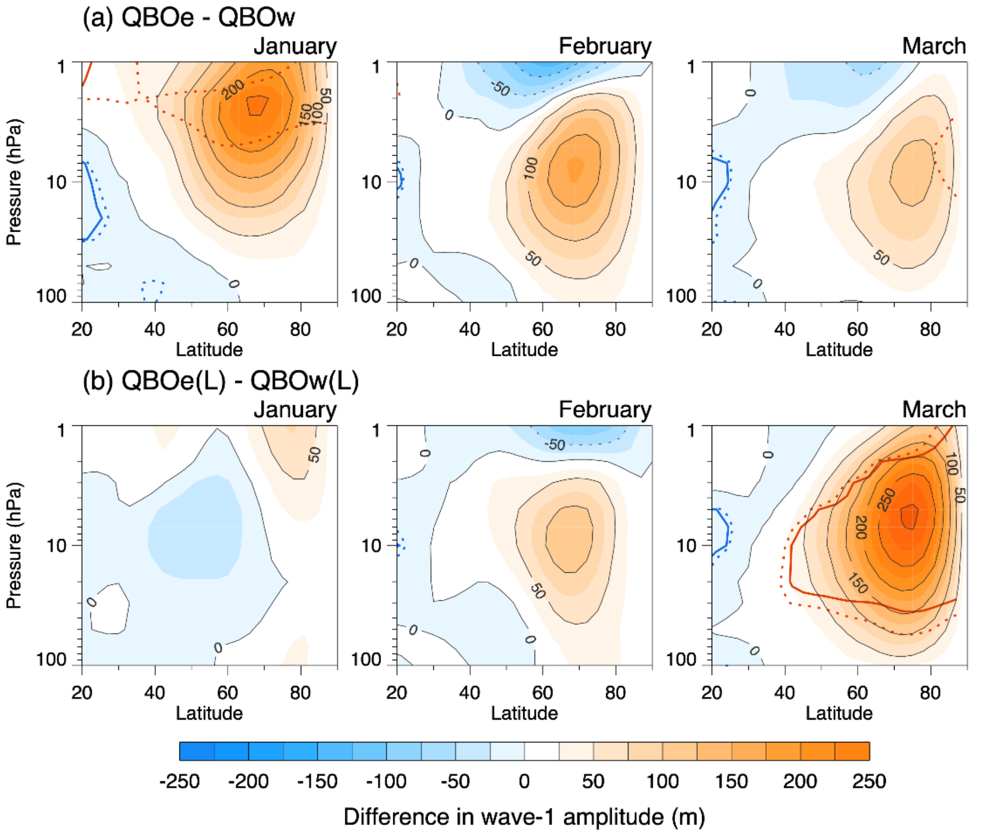

Figure 4.4 Composite differences of Z_1 between QBOe and QBOw for (a) all years, and (b) large-amplitude years. Blue (negative) and red (positive) dotted and solid lines represent statistical significance at the 90% and 95% levels, respectively.

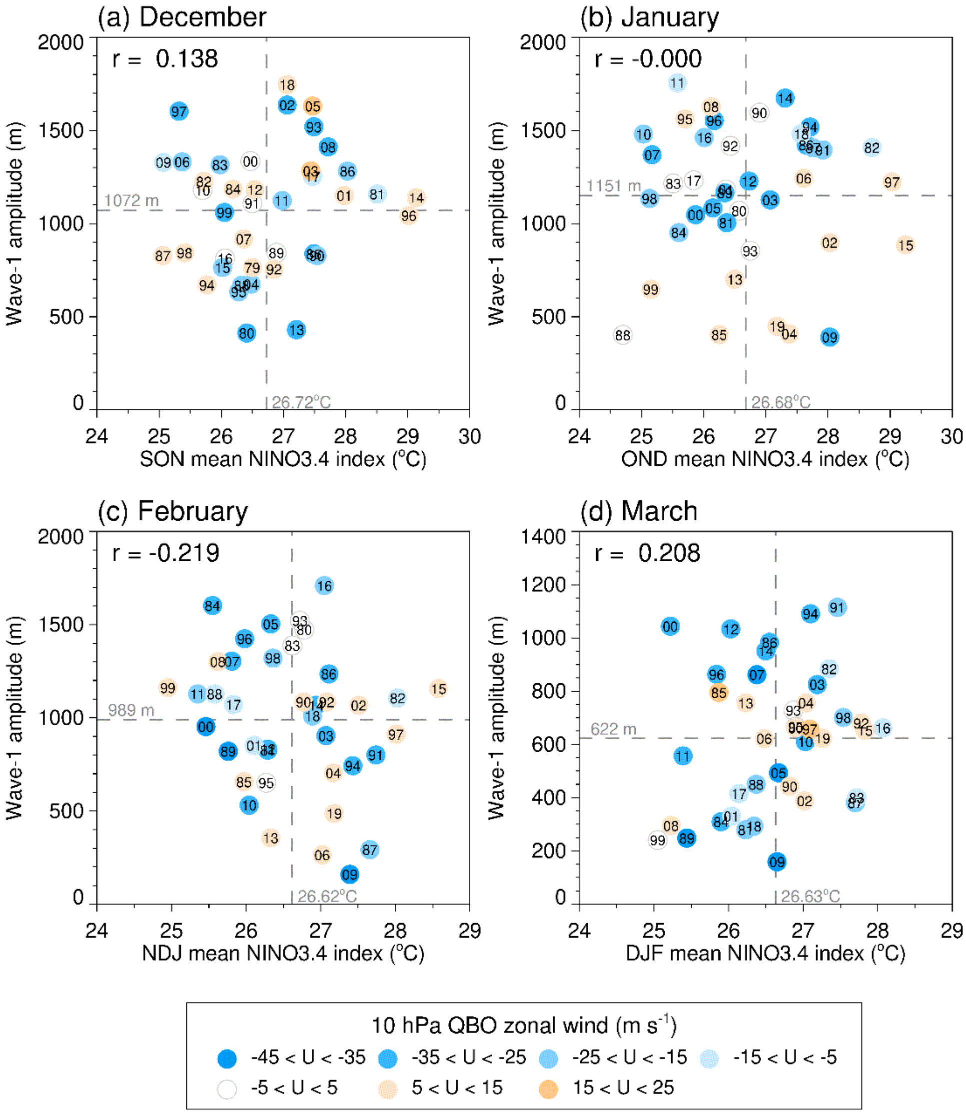

Figure 4.5 Scatter plots of the monthly mean high-latitude wave-1 amplitudes (averaged over 60–80°N) at 3 hPa versus the preceding three-month average of the Niño 3.4 indices. The numbers denote the year, and the colors of filled circles represent the QBO zonal-mean zonal winds (averaged over 5°S–5°N) at 10 hPa. The vertical and horizontal dashed lines with values are climatological averages of the Niño 3.4 indices and monthly mean high-latitude wave-1 amplitudes, respectively, for 1980–2019.

4.2. Case Study: Planetary Wave Development in March 1994 and 1995

4.2.1. Daily evolution of wave-1 growth

The amplitudes of planetary waves described in the previous section were composed of individual planetary wave events, which included the wave growth and decay processes. To investigate the dynamical processes underlying typical wave development during each phase of the QBO, two events were selected (one in March 1994 in QBOe phase and the other in March 1995 in QBOw phase). These two events are referred as Events 94 and 95, respectively.

The daily evolution of the wave-1 perturbation of the GPH at 3 hPa during Events 94 and 95 is shown in Figure 4.6. The periods 18–29 March for Event 94 and 11–22 March for Event 95 were analyzed based on subjective observation of the daily maps. During Event 94 (Figure 4.6a), on 18 March a ridge was located at 70°N and 240°E. On the same day, another ridge with a smaller magnitude was found at 35°N and 30°E. That middle-latitude ridge gradually grew and moved northeastward to 55°N and 70°E, but the high-latitude ridge moved slightly westward to 210°E and weakened by 23 March. At this time, the phase of the wave-1 pattern clearly showed a northeastward tilt. Then, from 24 to 28 March, the ridge that originated from the middle latitude rapidly developed and finally replaced the original high-latitude perturbation by 29 March. The phase of the high-latitude wave-1 kept moving eastward, and thus returned to nearly the original longitude of 210°E on 18 March. Another wave-1 event also occurred on 2–8 March in 1994 (not shown here). Event 94 was therefore characterized by growth of the middle-latitude perturbation with northeastward movement, which replaced the high-latitude perturbation.

Event 95 displayed a different pattern of high-latitude wave-1 growth (Figure 4.6b). On 11 March, a high-latitude ridge was located at 70°N and 60°E, and another ridge was located at 40°N and 270°E. Both the high- and middle-latitude ridges dissipated without interaction during the following days (12–13 March). On 14 March, a signal of the northeastward phase tilt was observed, and the high-latitude ridge had started to develop at 70°N and 180°E by 21 March. The high-latitude ridge did not return to the same longitude after Event 95. The longitude of the wave-1 ridge on 21 March was 120° out of phase with that on 21 March.

In Figure 4.7, the evolution of the wave-1 perturbation discussed above is shown in terms of the change of amplitude and phase in the time-latitude domain. The dates of the minimum and maximum wave-1 amplitude at high latitudes, averaged over 60–80°N, are denoted by the blue and red vertical dotted lines, respectively. During Event 94 (Figure 4.7a), wave-1 exhibited a middle-latitude maximum amplitude on 23 March (A), which was before the high-latitude minimum on 24 March (B). This middle-latitude wave grew and moved northward with time, as shown by the black dashed line in Figure 4.7a, and seemed to enhance the growth of the high-latitude wave. The location of the amplitude moved gradually (C) toward high latitudes and reached its maximum on 28 March (D). With regard to the phase change, the northeastward tilting pattern appeared before wave-1 development. On 23 March, 1994 (A), the wave-1 phase was around 180° at 70°N but was 30°E at 30°N. During the growth of high-latitude wave-1, the strong northeastward phase tilt was rapidly reduced. For example, on 27 March, 1994, wave-1 at 40–80°N was nearly stationary around 150°E.

The characteristic features associated with the amplitude and phase change seen during wave growth for Event 94 were not observed during Event 95 (Figure 4.7b). The movement of the growing wave-1 from middle to high latitudes did not occur before the minimum amplitude was reached on 12 March, 1995 (E, F). In addition, the positive meridional phase gradient, which appeared in the middle of the event on 14 March, 1995, did not significantly change even after the date of the maximum amplitude, i.e., 21 March, 1995 (H).

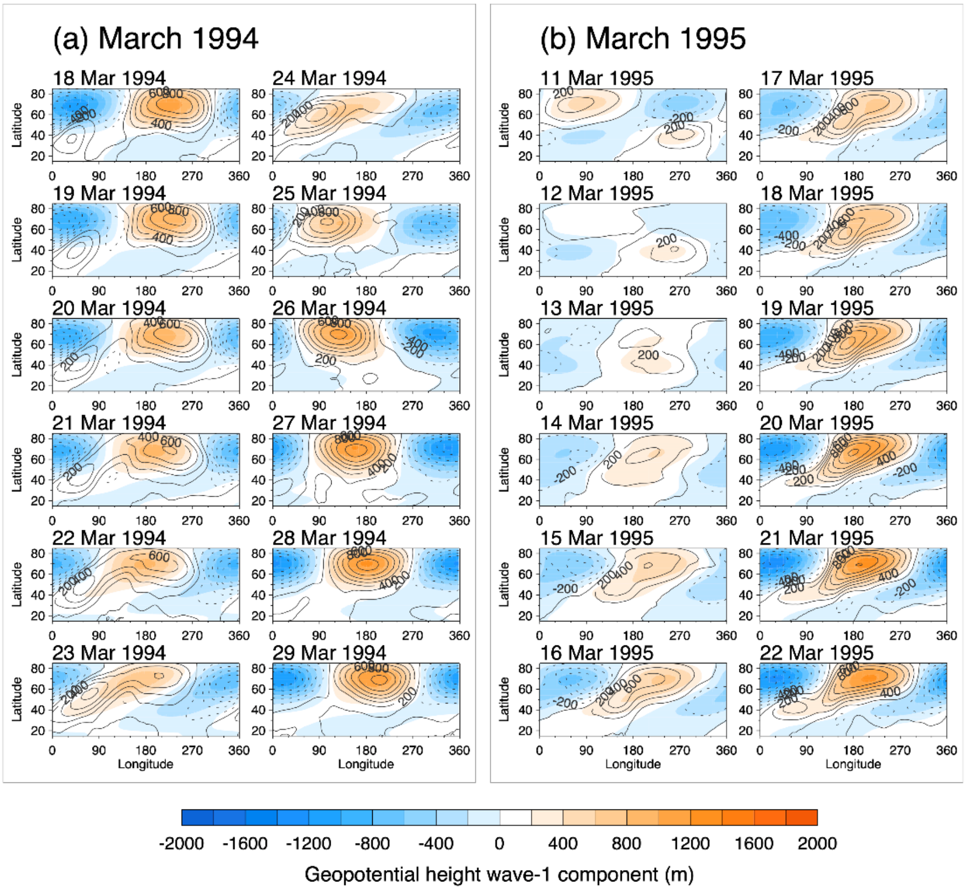

Figure 4.6 Daily evolution of the GPH zonal anomaly at 3 hPa shown by contours, and its wave-1 component (shown by color shading) for (a) 18–29 March, 1994, and (b) 11–22 March, 1995. The contour intervals are 200 m.

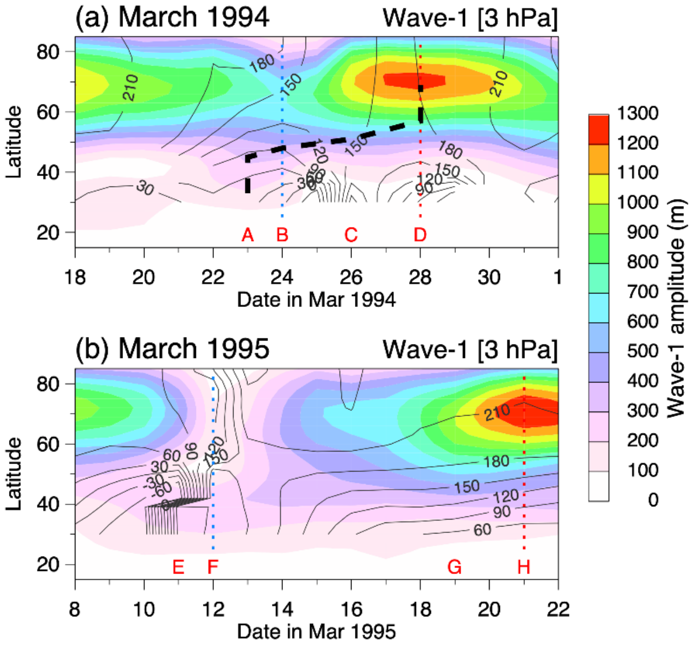

Figure 4.7 Daily evolution of zonal wave-1 at 3 hPa (amplitude indicated by shading), and the phase (shown by contours): (a) March 1994 and (b) March 1995. The blue and red vertical dotted lines denote the days with the minimum and maximum high-latitude amplitude, respectively. The thick dashed line between 30°N and 70°N in (a) represent the date of the maximum amplitude at each latitude during Event 94. See the manuscript for a description of red characters A–H.

4.2.2. Eddy forcing

To understand the role of eddy forcing in wave development, the eddy momentum flux ($\overline{u'v'}$), eddy heat flux ($\overline{v'T'}$), and EP flux divergence (EPFD) were calculated and displayed in Figure 4.8. During Event 94, the eddy momentum flux increased over time during 20–23 March, with the latitude of the maximum eddy momentum flux increasing from 40°N to 55°N (Figure 4.8a). After 24 March, 1994 (B), the eddy momentum flux decreased rapidly (Figure 4.8a), while the eddy heat flux continued to increase in high latitudes and reached a maximum on 26 March, 1994 (C) (Figure 4.8b).

The region of EPFD in 1994 (Figure 4.8c) moved from 30°N on 21 March into the high-latitude region at 70°N on 26 March. In the high latitudes before 26 March, the divergence of the meridional flux canceled out the convergence of the heat flux, while convergences of both the horizontal and vertical EP flux components contributed to the total EP flux convergence in middle latitudes before 24 March, 1994 (B). Therefore, the wave-1 event in March 1994 can be characterized as the propagation of eddy momentum forcing from middle to high latitudes. Before 24 March, the role of the eddy momentum flux was important at middle latitudes. After 24 March, however, the heat flux was dominant at the high-latitude wave growth stage (B–D).

For Event 95, both the eddy momentum and heat fluxes started to increase on 15 March and remained at similar levels even after the maximum amplitude was reached on 21 March (H) (Figures 4.8d and 4.8e). Although the components of the meridional EPFD and vertical EP flux were significant, the total EP flux convergence (Figure 4.8f) during high-latitude wave-1 development (12–21 March, 1995) was weaker compared to that in Event 94

(Figure 4.8f).

Meridional cross-sections of the EP flux and its divergence are shown with the wave-1 phase in Figure 4.9. At each stage, the dynamical process of Event 94 had a deep vertical pattern through the middle-to-upper stratosphere (Figure 4.9a). At the early stage (A and B), the middle-latitude upper stratosphere was relatively barotropic, as shown by the vertically oriented phase lines. The EP flux vectors perpendicular to the phase lines indicated equatorward propagation and concentration of the wave activity over 30–60°N, while divergence of wave activity occurred at high latitudes (north of 60°N). At the wave growth stage (C), the poleward focusing of vertically propagating planetary waves north of 50°N in the upper stratosphere was consistent with the strong EP flux convergence. For Event 95, the wave activity over the upper stratosphere was generally weak in the early stage (E and F), and the structure during wave growth (G and H) was similar to that of the early stage in Event 94 wave growth stage.

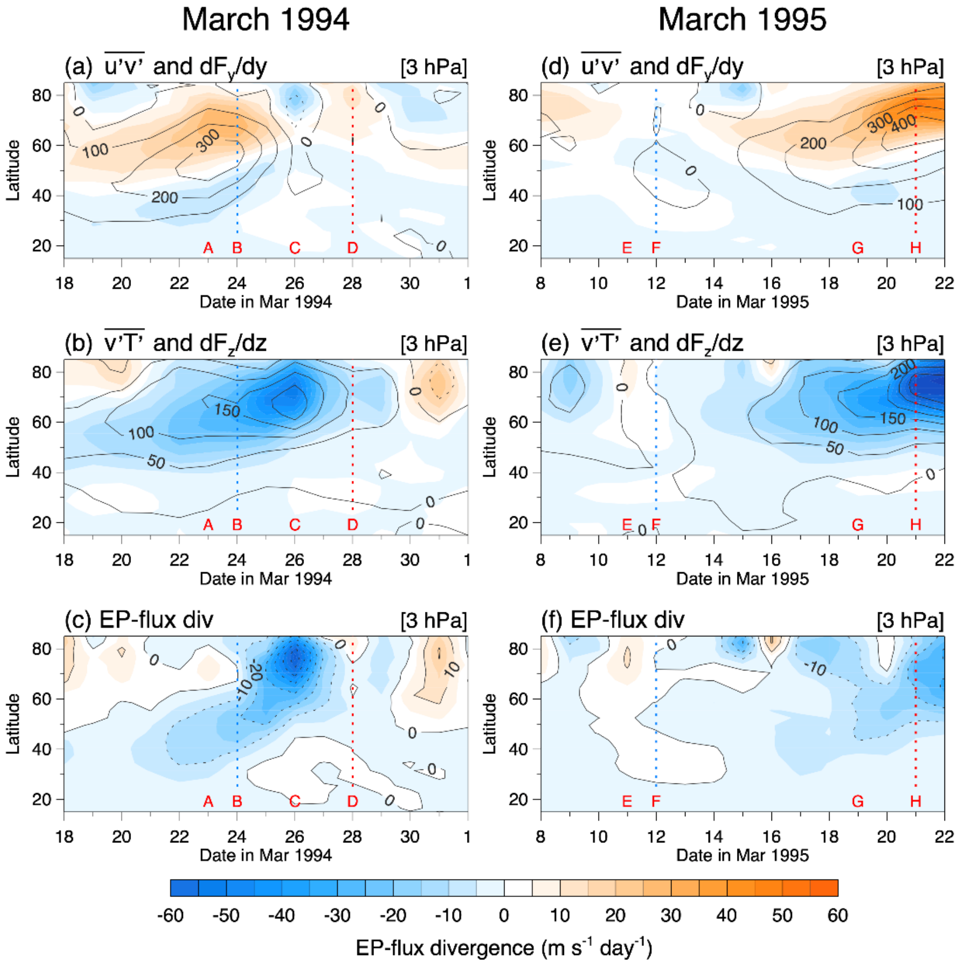

Figure 4.8 Daily evolution of (a), (d) eddy momentum flux in contours (interval = 100 m^2 s^{-2}) and its meridional divergence (indicated by shading); (c), (d) eddy heat flux (indicated by contours; interval = 50 K m s^{-1}) and its vertical divergence (indicated by shading); and (e), (f) EPFD at 3 hPa in March. The left and right columns are for 1994 and 1995, respectively. See the manuscript for a description of red characters A–H.

(a) March 1994

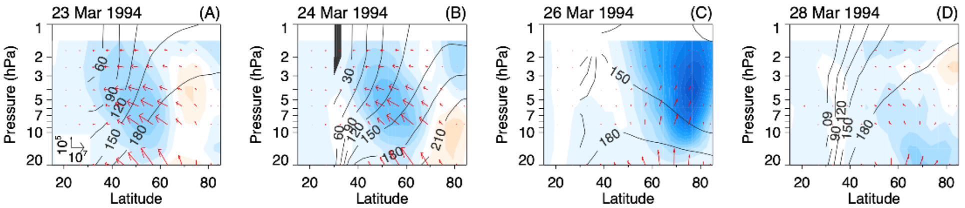

(b) March 1995

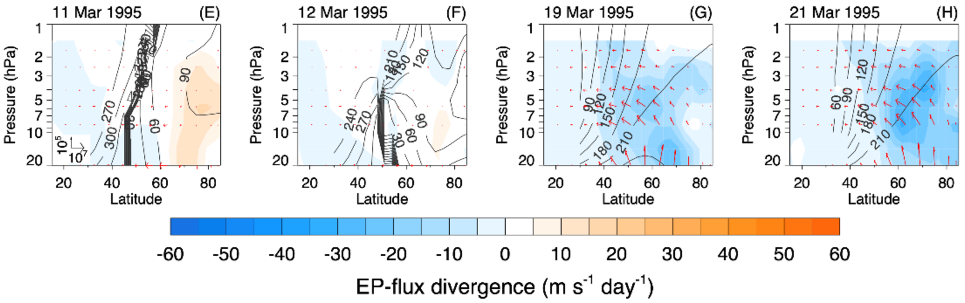

Figure 4.9 Meridional section of the phase of the wave-1 (indicated by contours), EP flux (indicated by red arrows), and EPFD (indicated by shading) in March (a) 1994 and (b) 1995. (A)–(H) are the same dates as in Figure 4.7. Reference arrows represent 10^7 and 10^5 kg s^{-2} for the meridional and vertical components, respectively.

4.2.3. Potential vorticity and enstrophy

Quasi-geostrophic potential vorticity (QGPV) was used to examine the dynamical mechanism of wave development. Figure 4.10a shows the temporal evolution of the perturbation QGPV (q') at 3 hPa during Event 94. On 20 March, the middle-latitude negative maximum q' (in blue) was located at 45°E and 45°N, which was approximately 180° out of phase from the high-latitude negative maximum q' (located at 240°E and 75°N). From 20 March, the middle-latitude negative q' gradually moved northeastward to 70°N (26 March) with the increase in its magnitude. From 26 to 28 March, the high-latitude negative q' moved eastward with a slight decrease in its magnitude. The general pattern of the longitude-latitude distributions of q' from 20 to 28 March was similar to that of the perturbation GPH (Figure 4.6a), although the high-latitude maximum amplitude of GPH appeared on 28 March.

Figures 4.10b and 4.10c show the perturbation QGPV flux ($v'q'$) and zonal-mean eddy QGPV flux ($\overline{v'q'}$), respectively. An area with a particularly strong negative $v'q'$ appeared at high latitudes on 26 March, resulting in a large negative $\overline{v'q'}$. The flux of the large negative $\overline{v'q'}$ in the middle-latitudes enhanced the transport of the middle-latitude perturbation into the high latitudes. The large negative value of $\overline{v'q'}$ was consistent with the northeastward phase tilt of the PWs. The phase tilts appeared in the daily distributions of the perturbation GPH (20–24 March, Figure 4.6a) and QGPV (22–26 March, Figure 4.8a). As shown in Figure 4.10c, the small $\overline{v'q'}$ at 40°N moved northward with rapid development until reaching a maximum on 26 March at 70°N. By 28 March, the magnitude of $\overline{v'q'}$ was rapidly reduced, consistent with the diminishing phase tilt.

Figure 4.11 shows a schematic representation of the relationship between the northeastward phase tilt and the negative $\overline{v'q'}$. The negative perturbation q' in the middle latitudes and high latitudes produce northeastward-tilting and generate large negative $v'q'$ in the northwest of the maximum perturbation q'. As a result, the negative maximum $\overline{v'q'}$ appears north of the maximum perturbation q' and induces northward growth of the middle-latitude perturbation.

The dynamical mechanism of wave amplification may be interpreted according to the wave activity density, i.e., the conserved quantity in the generalized EP theorem (Andrews and McIntyre, 1976; Edmon et al., 1980). In this study, the potential enstrophy used followed Smith et al. (1984). Using the potential enstrophy was more practical because the $\partial\bar{q}/\partial y$ term in the denominator of the wave activity density sometimes changes the sign in the stratosphere. Potential enstrophy is defined as $\overline{q'^2}/2$, and its temporal change is assumed to be as follows:

$$\frac{\partial}{\partial t}\left(\overline{q'^2}/2\right) \sim -\,\overline{v'q'}(\partial\bar{q}/\partial y)$$

In the above equation, the change in potential enstrophy is mainly determined by the wave-mean flow interaction. The wave-wave interactions and diabatic heating terms on the right-hand side are neglected.

The daily evolution of the potential enstrophy, temporal changes, and wave–mean flow interaction terms are shown in Figure 4.12 for Events 94 and 95. In 1994, the maximum potential enstrophy appeared at 75°N on 26 March (Figure 4.12a). This was 2 days before the date of the maximum wave-

1 amplitude on 28 March (Figure 4.7a). In Figure 4.12b, in the early stage (20–24 March, 1994), the temporal change at about 40–50°N increased over time with increasing latitude, with the maximum change occurring on 25 March at high latitudes. Throughout Event 94, the pattern of enstrophy change shown in Figure 4.12b was close to that of the wave–mean flow interaction term in Figure 4.12c. The wave-mean flow interaction term was the multiplication of $\overline{v'q'}$ and $\partial\bar{q}/\partial y$. The daily distribution of $\overline{v'q'}$ (not shown here) was similar to that of the EPFD (Figure 4.8c). The EPFD exhibited maximum convergence on 26 March, 1994 at 70°N, while the wave-mean flow interaction term displayed a positive-to-negative sign change on the same day. The sign of $\partial\bar{q}/\partial y$ (not shown here) changed before and after 26 March, which produced the sign change in the wave–mean flow interaction term. Through this change, the potential enstrophy decreased after 26 March, 1994.

In 1995, the high-latitude maximum wave enstrophy appeared after maximum wave-1 amplitude on 21 March, 1995 (Figure 4.12d). Unlike Event 94, the contribution of the wave–mean flow interaction term to the temporal change was insignificant (Figures 4.12e and 4.12f). The positive $\partial\bar{q}/\partial y$ over 30–60°N and negative $\overline{v'q'}$ after 14 March, 1995 induced a positive wave–mean flow interaction at middle latitudes (Figure 4.12f), but this effect was not apparent in the enstrophy change (Figure 4.12e).

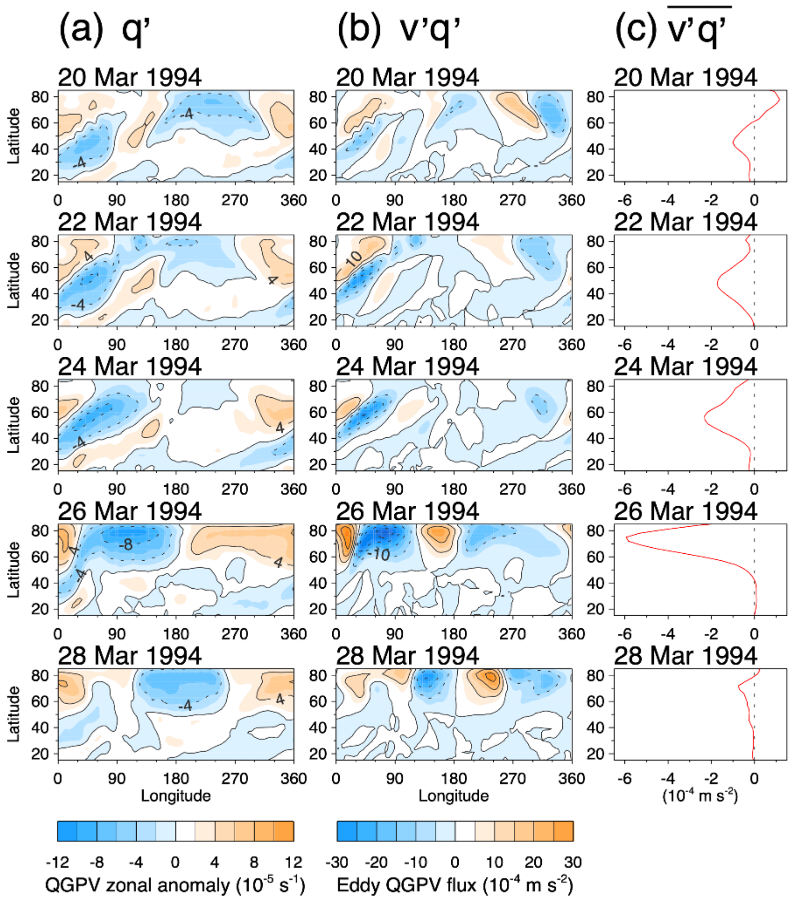

Figure 4.10 Longitude-latitude distributions of (a) q' (left column), (b) $v'q'$ (central column), and (c) $\overline{v'q'}$ (right column) at 3 hPa for 20–28 March, 1994 at 2-day intervals.

(a) Stage 1

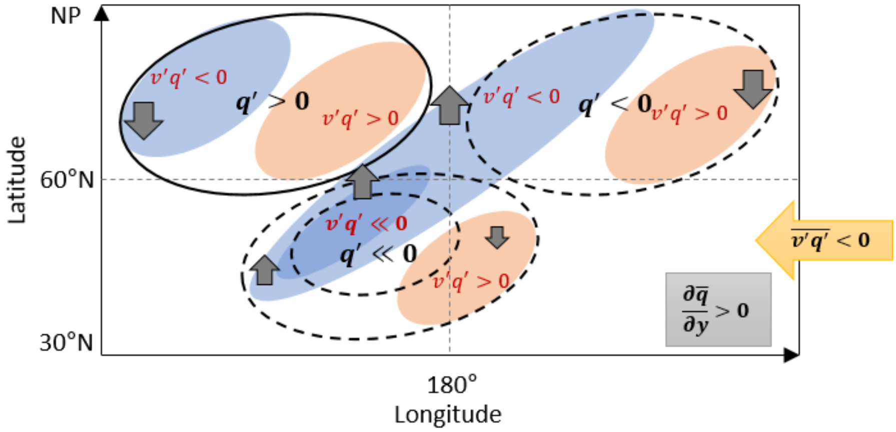

(b) Stage 2

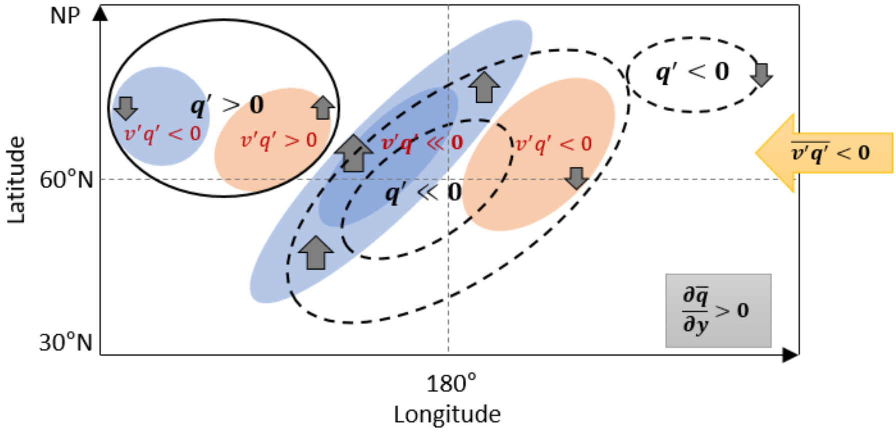

Figure 4.11 Schematic diagrams of the wave-1 amplification process through the wave-mean flow interaction that contributes to the increase in potential enstrophy.

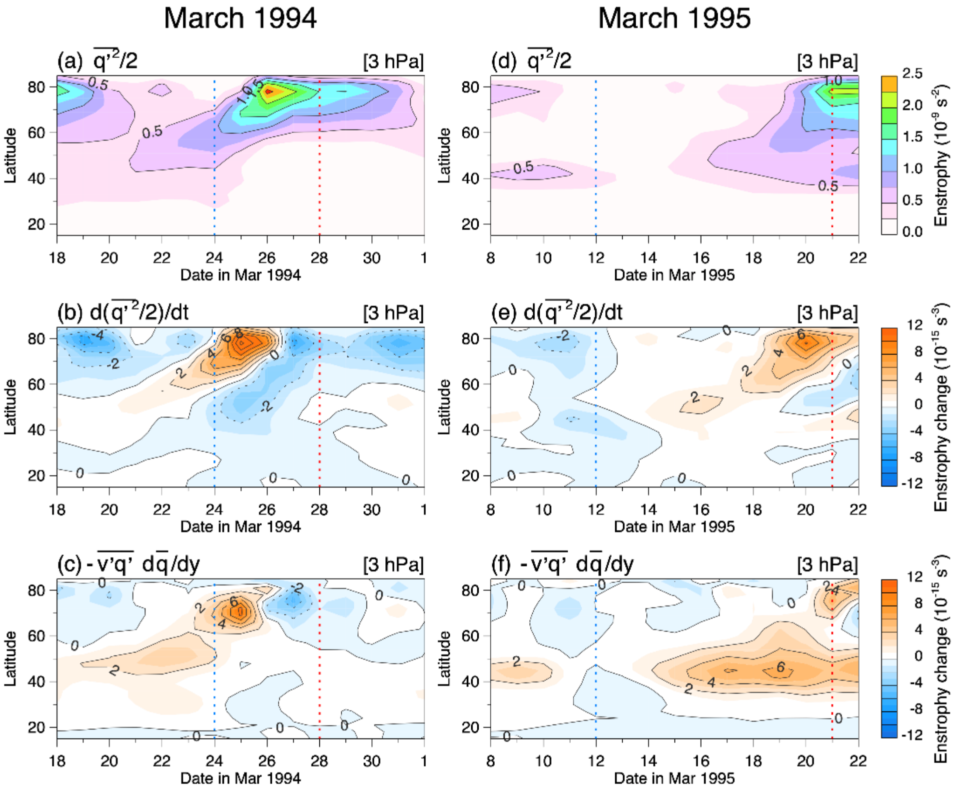

Figure 4.12 Daily evolution of the (a), (d) potential enstrophy (10^{-9} s^{-2}), (b), (e) rate of change in potential enstrophy (10^{-15} s^{-3}), and (c), (f) wave–mean flow interaction term (10^{-15} s^{-3}), in March 1994 (left column) and March 1995 (right column). Blue and red vertical dotted lines denote the days with the minimum and maximum high-latitude amplitude, respectively.

4.2.4. Eddy kinetic energy

As described in the previous section, the propagation of the middle-latitude disturbance into high latitudes with growth during Event 94 seemed to play an important role in the large amplitude observed in March 1994. Here the wave growth is investigated in terms of the wave energy, particularly the EKE. The EKE (K') is defined here as follows:

$$K' \equiv \rho_0 \left(\overline{u'^2} + \overline{v'^2}\right)/2$$

where ρ_0 is the standard density in log-pressure coordinates. To determine if EKE can be regarded as a proxy of the amplitude of the PWs, scatter plots of Z_1 versus the monthly mean EKE at 3 hPa are shown in Figure 4.13. Both variables were averaged over high latitudes (60–80°N). There was a significant correlation between the two variables in all 3 months, and it therefore seemed reasonable to assume that EKE represented the wave amplitude.

Figure 4.14a shows the daily evolution of EKE at 3 hPa during Event 94. The minimum and maximum EKE in at high latitudes (> 70°N) occurred on 24 and 28 March, respectively, and these dates agreed with those of the min/max amplitude of planetary waves. Large values of EKE in the subtropical region (~25°N) during the early stage (20–22 March) moved northward with time, and reached 40°N on 24 March. The northward movement of large EKE with time was consistent with the temporal change in EKE ($\partial K'/\partial t$) shown in Figure 4.14b, starting at 25°N on 30 March and reaching 60°N on 26 March. Another local maximum $\partial K'/\partial t$ started at 60°N on 21 March, and moved northward until reaching the polar region on 25 March. One of the dominant factors determining the rate of change in EKE was the conversion of zonal-mean kinetic energy (ZKE; $\bar{K}$) to EKE, defined as follows:

$$-[K' \cdot \bar{K}] \equiv -\rho_0 \overline{u'v'}(\partial \bar{u}/\partial y)$$

Figure 4.14c shows the energy conversion from the ZKE to EKE, which was essential to produce the rapid increase of the EKE (Figure 4.14b) during the early stage of Event 94 from 18 to 21 March at 30°N. The northward movement of the other local maximum $\partial K'/\partial t$ at 60°N from 21 March agreed with the energy conversion term in Figure 4.14c.

Because eddy momentum flux was generally positive over the extratropical upper stratosphere, the sign of the conversion of ZKE to EKE in the middle latitudes was determined by the meridional shear of the zonal wind ($\partial \bar{u}/\partial y$). Therefore, on 21 March, 1994, the negative meridional shear of the zonal wind ($\partial \bar{u}/\partial y < 0$) at both 30°N and 60°N (Figure 4.14d) produced positive energy conversion (Figure 4.14c) and a positive change in the EKE (Figure 4.14b). The energy conversion from the ZKE to EKE seemed to provide the necessary wave energy for the northward growth of the middle-latitude perturbation seen in the early stage of Event 94 by wave–mean flow interaction. In this case, the sign of $\partial \bar{u}/\partial y$ at middle latitudes was a crucial factor.

During Event 95, EKE reached its a minimum and maximum at high latitudes on 12 and 21 March, respectively (Figure 4.14e). Although there was a local high EKE region between 20°N and 35°N on 10 and 11 March, it did not grow and move northward, unlike in Event 94. On 12 March, $\partial K'/\partial t$ had a negative value over the whole hemisphere (Figure 4.14f). Comparison of the conversion of ZKE to EKE (Figures 4.14c and 4.14g), and the meridional shear of the zonal wind (Figures 4.14d and 4.14h), revealed significant differences between the 2 years. In 1994 the zonal wind, its meridional shear, and the energy conversion from the ZKE to EKE moved northward with time, while these variables mostly remained at the same latitudes in 1995.

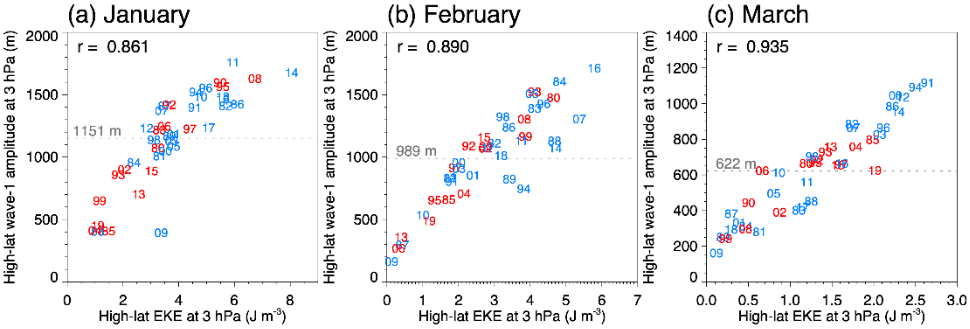

Figure 4.13 Scatter plots of high-latitude Z_1 at 3 hPa versus high-latitude EKE at 3 hPa in (a) January, (b) February, and (c) March; the correlation coefficient r is shown. The blue and red numbers denote years with QBOe and QBOw phases, respectively. The horizontal dotted line represents the climatological mean Z_1 for each month.

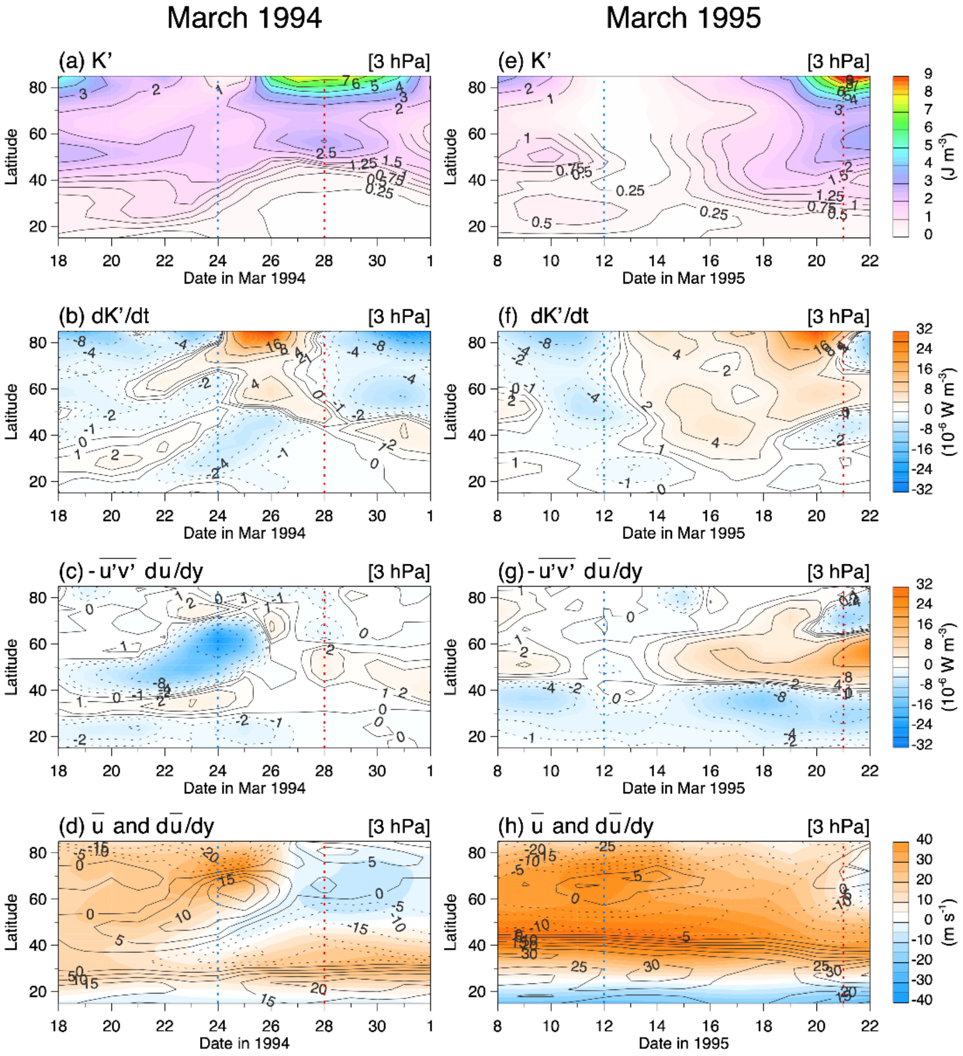

Figure 4.14 Daily evolution of (a), (e) EKE (K') (J m^{-3}); (b), (f) $\partial K'/\partial t$ (10^{-6} W m^{-3}); (c), (g) conversion of ZKE to EKE (10^{-6} W m^{-3}); and (d), (h) $\bar{u}$ (indicated by color shading) and $\partial\bar{u}/\partial y$ (indicated by contours) at intervals of 5×10^{-6} s^{-1} in March 1994 (left column) and March 1995 (right column). Blue and red vertical dotted lines denote the days with the minimum and maximum high-latitude amplitude, respectively.

4.3. Composite Analysis: Daily Evolution of Planetary Waves and QBO

4.3.1. Identification of wave-1 growth events

The previous section discussed the dynamical processes underlying wave-1 development in March 1994 in QBOe and March 1995 in QBOw. Comparison between the two wave-1 events implied that meridional shear of the zonal wind, and therefore the sign of the conversion of ZKE to EKE in the middle latitudes, could provide the dynamic conditions for the growth of middle latitude perturbations with movement into high latitudes. This section will investigate that the characteristics of the wave-1 development cases from March 1994 and 1995 can be extended into the whole period of the ERA-Interim reanalysis data from 1979 to 2019.

To generalize the characteristics of wave-1 growth in Event 94 and Event 95 cases, the wave-1 amplification events should be defined. Based on the daily time series of wave-1 amplitude in high latitudes (averaged over 60–80°N at 3 hPa), a wave-1 growth event was defined as the period of monotonic increase in the wave-1 amplitude, from a negative peak (minimum amplitude) to the following positive peak (maximum amplitude). Total 746 events can be identified for the 40 winter periods from 1979/1980 to 2018/2019. This study used the median value of the amplitude growth for the total wave-1 amplification events ($\Delta Z = 275$ m) as a threshold to exclude minor events in the analysis (Figure 4.15a). Frequency distributions of the wave-1 amplification period (ΔZ) and the average wave-1 amplitude (Z_1) are less skewed for the significant wave-1 amplification events ($\Delta Z > 275$ m) (Figures

4.15b and 4.15c). The total 373 of the significant wave-1 amplification events for the whole analysis period (1979/1980–2018/2019 winter) are shown in Figure 4.16.

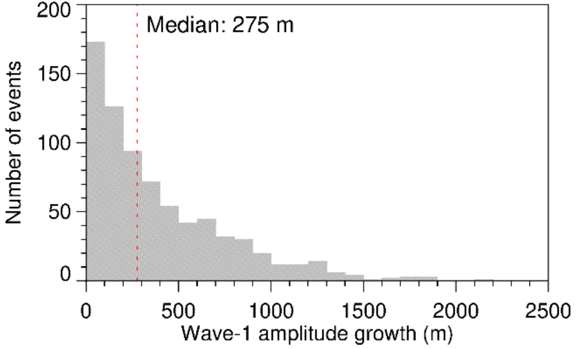
(a) Amplitude growth (ΔZ)

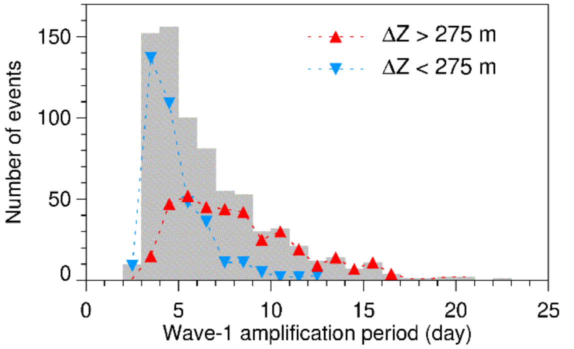
(b) Amplification period (Δt)

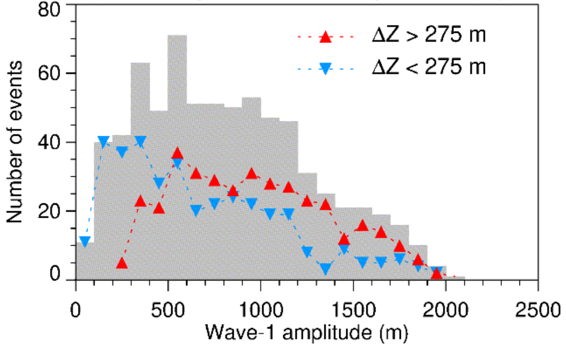
(c) Average wave-1 amplitude (Z_1)

Figure 4.15 Histograms of the (a) amplitude growth (ΔZ), (b) amplification period (Δ*t*), and (c) wave-1 amplitude (Z_1) for a total of 746 events of the high-latitude wave-1 amplification. The red vertical dotted line in (a) denotes the median values of the amplitude growth (275 m). The solid triangles in red and blue with dotted lines in (b) and (c) show distributions of the significant amplification events (ΔZ > 275 m) and the minor events (ΔZ < 275 m), respectively.

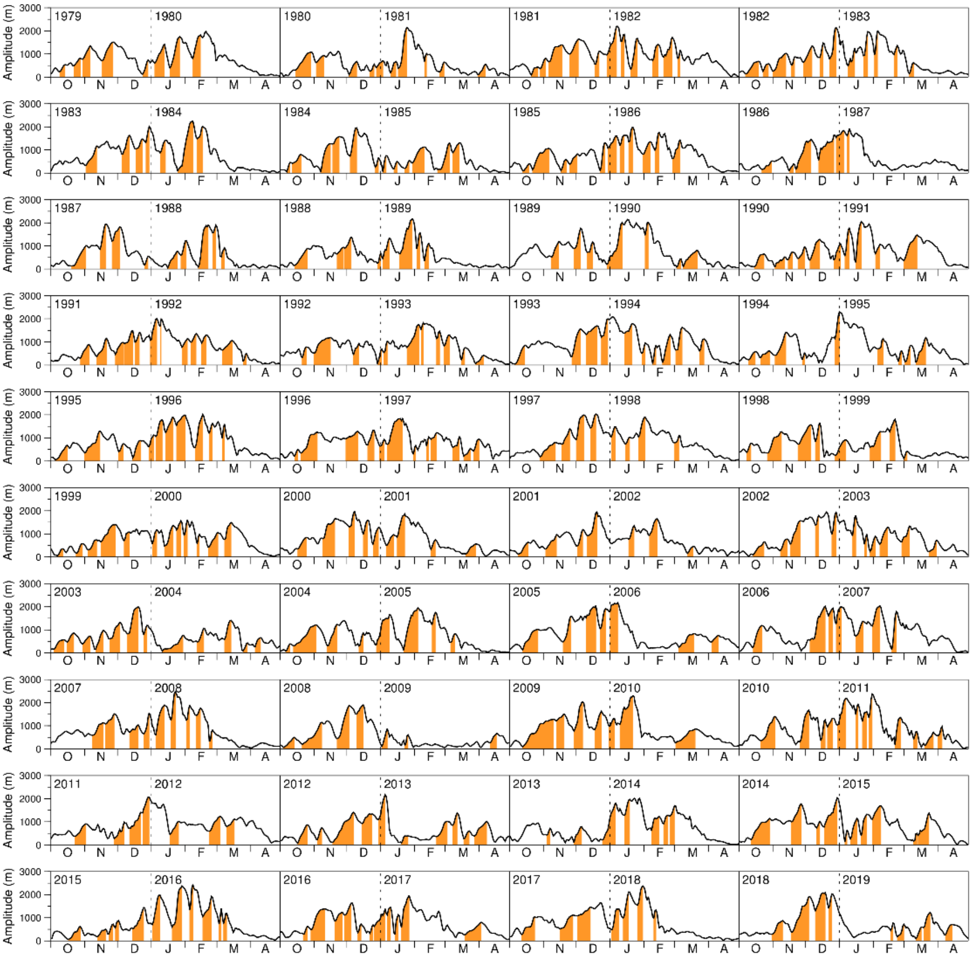

Figure 4.16 Time series of the high-latitude wave-1 amplitude (averaged over 60–80°N) for 40 winter seasons of 1979/1980 to 2018/2019. The periods shaded by orange are the significant amplification events (ΔZ > 275 m).

4.3.2. Response of wave-1 growth to QBO

Statistics of the wave-1 amplification events (ΔZ > 275 m) by the phase of the QBO are summarized in Table 4.2. Statistically significant differences between the QBOe and QBOw composites of the wave-1 amplification events are found in the average wave-1 amplitude for the amplification period only in January and March. Therefore, this chapter focuses on the different responses to the QBO between January and March and its mechanisms.

Figures 4.17 and 4.18 show composite averages of the zonal-mean GPH anomaly for the wave-1 development events (ΔZ > 275 m) in March and January. The notable point is that the QBOe-composite of wave-1 amplification events in March are similar to Event 94 in Figure 4.6a. The midlatitude disturbance appears at 20°–40°N on D−4 (stage 1), grows and moves northeastward at 40°–60°N on D+0 (stage 2), and replaces the high-latitude waves on D+4 at 60°–80°N (stage 3) (Figure 4.17a). This type of wave-1 growth pattern doesn’t occur in the QBOw-composite in March (Figure 4.17b) and QBOe- and QBOw-composites in January (Figure 4.18).

The wave-1 amplitudes in both January and March are larger in QBOe compared to the QBOw (Figures 4.19 and 4.20). However, the amplification mechanism is somewhat different. In March, because of the enhanced northeastward tilting of the wave-1 phase between stages 1 and 2, eddy momentum flux from D−4 to D+0 shows a positive anomaly in Figure 4.21a. The increase in the eddy momentum flux before the central date can be found only in QBOe in March (Figures 4.21 and 4.22). In January, on the other hand, vertically propagated planetary waves are more important for QBOe, as shown by increase of the eddy heat flux after the central date (Figure 4.22a).

Table 4.2 The numbers of the significant wave-1 amplification events (N) and the averages and standard deviations of the wave-1 amplitude growth (ΔZ), wave-1 amplification period (Δ*t*), and high-latitude amplitude (averaged over 60–80°N) of wave-1 (Z_1) and wave-2 (Z_2) for the QBOe and QBOw years for the period of 1979/1980–2018/2019.

Month	QBO phase	N	ΔZ (m)	Δ*t* (day)	Z_1 (m)	Z_2 (m)
Winter	QBOe	196	706 ± 370	7.9 ± 3.9	1002 ± 439	363 ± 191
(Oct. to Apr.)	QBOw	121	640 ± 300	8.2 ± 3.7	874 ± 429	297 ± 172
	p-value [a]		0.085	0.570	0.011	0.002
November	QBOe	30	638 ± 322	9.3 ± 3.6	708 ± 306	287 ± 120
	QBOw	25	763 ± 345	9.8 ± 3.9	925 ± 308	263 ± 110
	p-value [a]		0.173	0.627	0.088	0.444
December	QBOe	37	696 ± 327	7.6 ± 3.0	1126 ± 445	363 ± 181
	QBOw	27	721 ± 313	7.3 ± 2.8	1126 ± 414	371 ± 218
	p-value [a]		0.766	0.683	0.999	0.888
January	QBOe	49	859 ± 477	7.1 ± 2.9	1296 ± 391	487 ± 200
	QBOw	14	686 ± 356	7.4 ± 4.7	903 ± 607	440 ± 204
	p-value [a]		0.149	0.819	0.036	0.456
February	QBOe	33	726 ± 376	5.9 ± 2.3	1124 ± 369	430 ± 203
	QBOw	17	514 ± 147	6.4 ± 3.0	1033 ± 438	345 ± 130
	p-value [a]		0.007	0.618	0.471	0.079
March	QBOe	19	569 ± 225	6.7 ± 3.9	851 ± 269	314 ± 86
	QBOw	18	528 ± 243	7.9 ± 3.5	621 ± 287	221 ± 94
	p-value [a]		0.599	0.328	0.017	0.003

[a] *p*-values provided by the Welch's *t*-test (for the average difference between QBOe and QBOw groups)

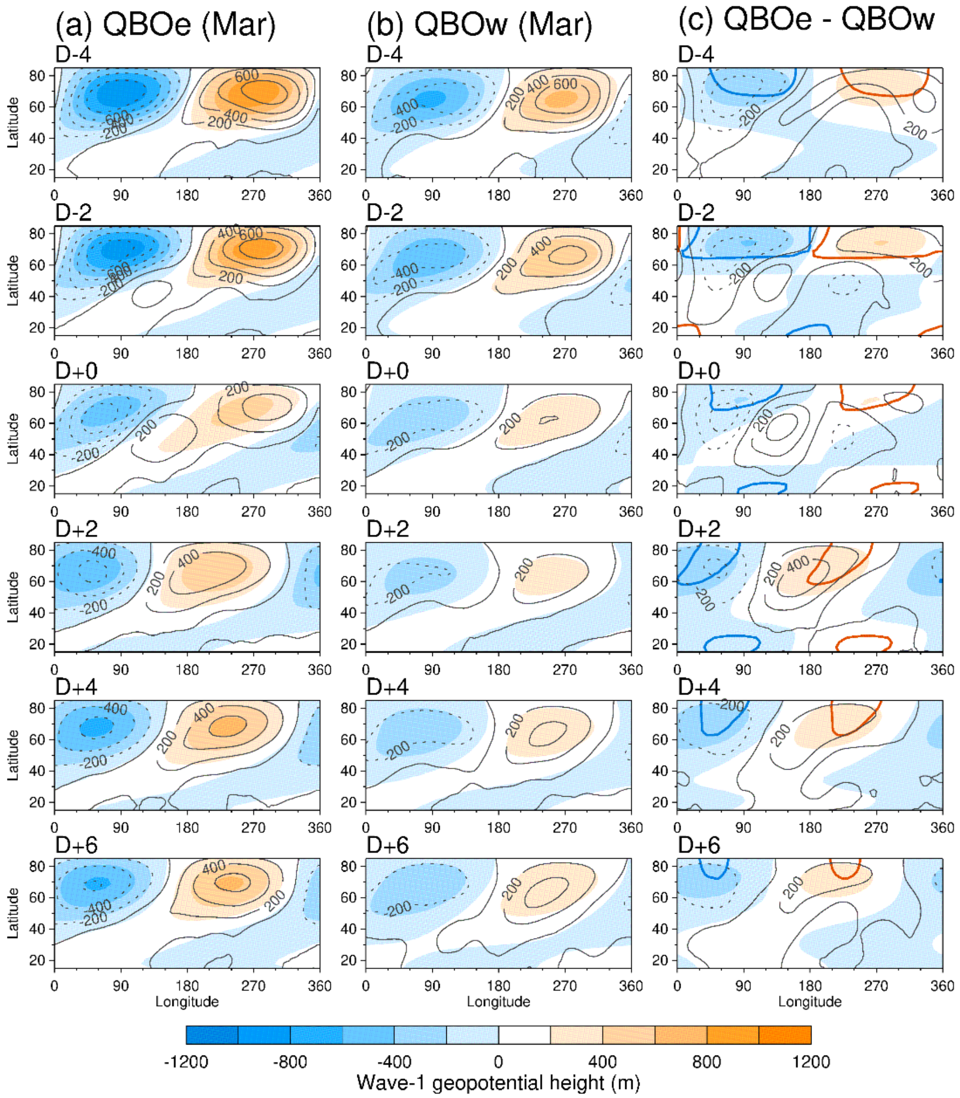

Figure 4.17 Composite averages of the zonal-mean geopotential height anomaly (contours plotted at 200 m intervals) and wave-1 geopotential height (color scale) for the significant wave-1 amplification events (ΔZ > 275 m) in March. (a) QBOe events (N = 19), (b) QBOw events (N = 18), and (c) composite difference between the QBOe and QBOw events. Areas enclosed by red and blue lines represent that the difference is statistically significant at the 95% level.

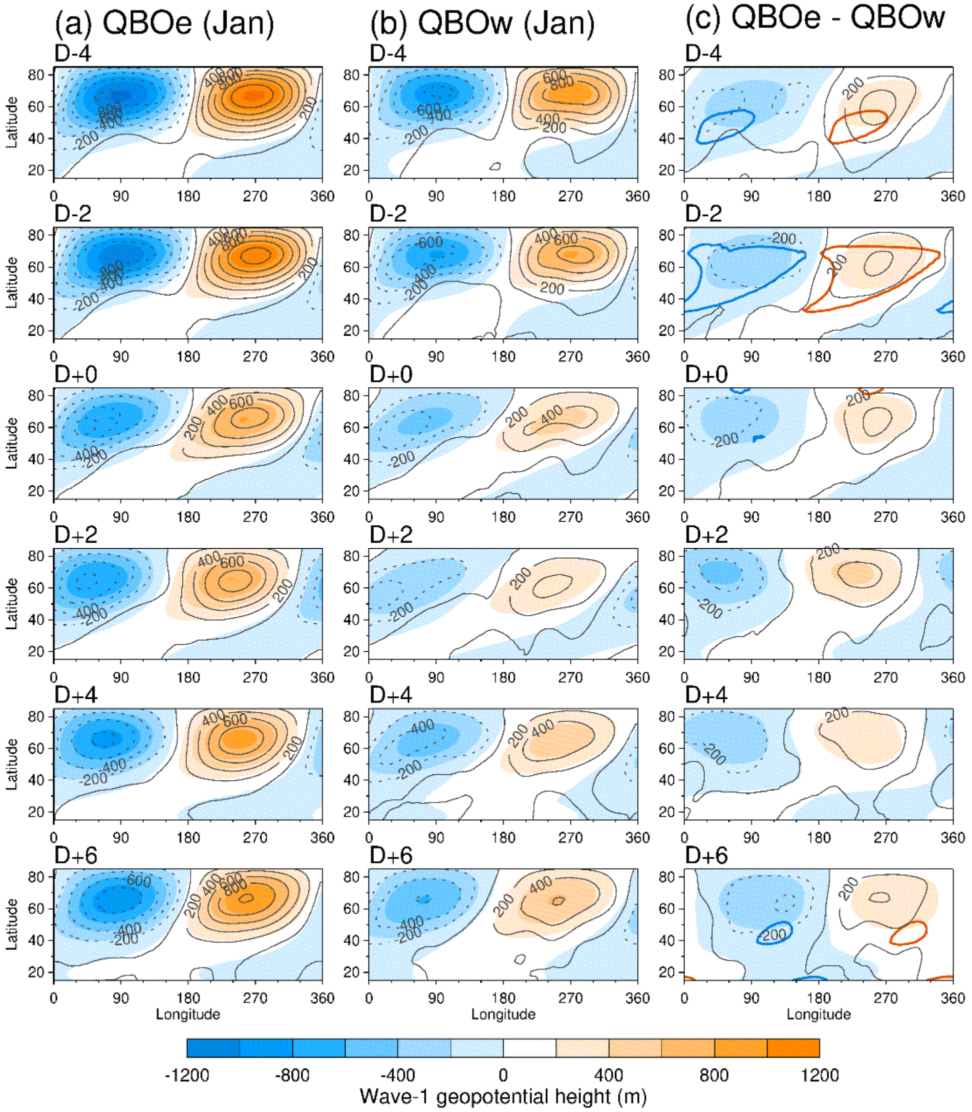

Figure 4.18 The same as in Figure 4.17, but for the QBOe events (N = 49) and QBOw events (N = 14) in January.

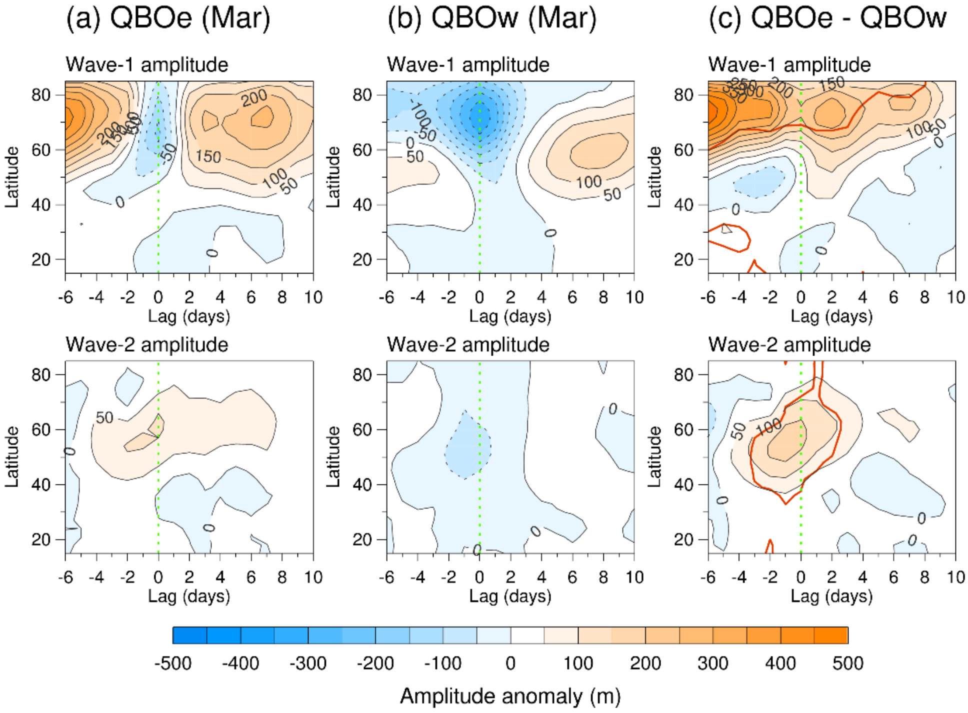

Figure 4.19 Composite averages of the climatological anomalies of geopotential height wave-1 and wave-2 amplitudes at 3 hPa on time-latitude sections for the (a) QBOe events (N = 19) and (b) QBOw events (N = 18) in March. (c) Composite differences between the QBOe and QBOw events. Areas enclosed by red and blue lines represent that the difference is statistically significant at the 95% level.

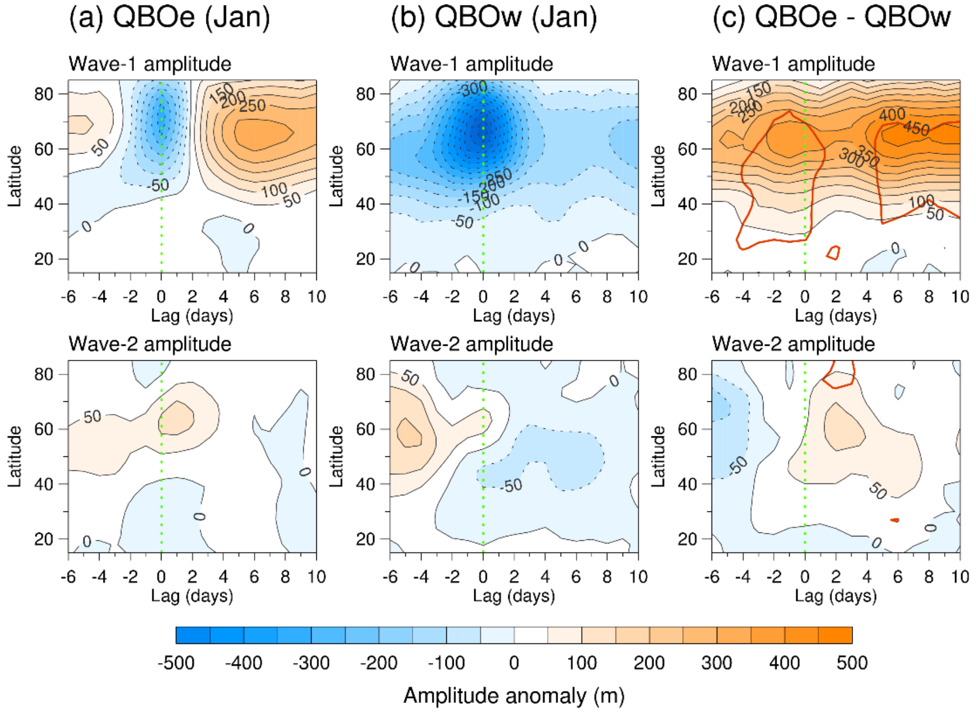

Figure 4.20 The same as in Figure 4.19, but for the QBOe events (N = 49) and QBOw events (N = 14) in January.

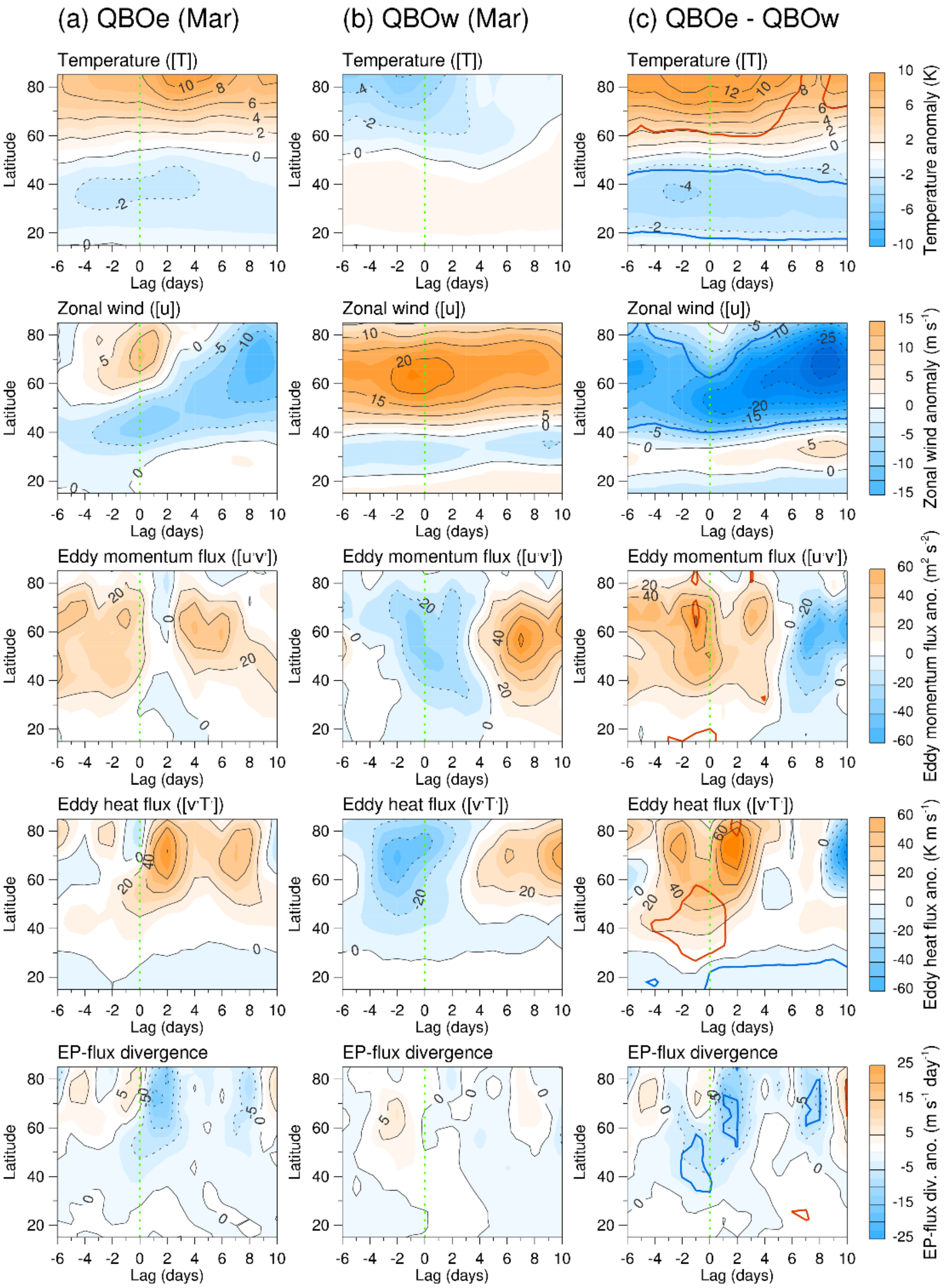

Figure 4.21 The same as in Figures 4.19 and 4.20, but for the climatological anomalies of zonal-mean temperature ($\overline{T}$), zonal-mean zonal wind ($\overline{u}$), eddy momentum flux ($\overline{u'v'}$), eddy heat flux ($\overline{v'T'}$), and divergence of the EP flux ($\boldsymbol{\nabla} \cdot \mathbf{F}$) in March.

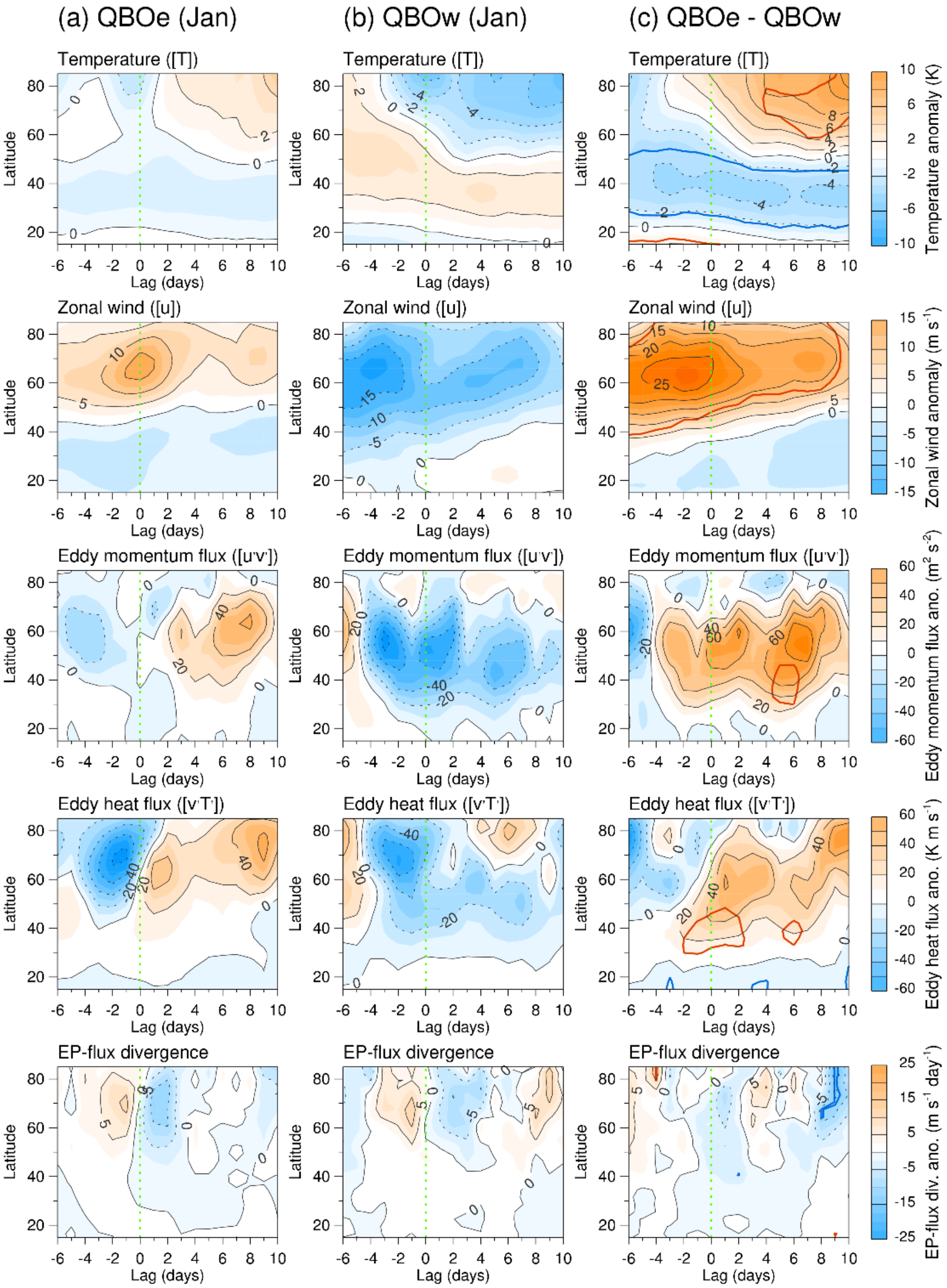

Figure 4.22 The same as in Figure 4.21, but in January.

4.3.3. Kinetic energy conversion

Composite averages of the climatological anomalies of EKE and $\partial K'/\partial t$ for the wave-1 amplification events in March with QBOe show the area of EKE > 0.2 J m^{-3} at 20°–40°N from D−6 to D+0 (Figure 4.23). During the period, the high values of EKE appears at the high-latitudes (> 40°N), but the high EKE decreases rapidly. Only the midlatitude EKE can be maintained by $\partial K'/\partial t \geq 0$ (Figure 4.23). At these latitudes (20°–40°N), $-\overline{u'v'}(\partial\bar{u}/\partial y) > 0$, which is equivalent to the kinetic energy transfer from ZKE to EKE, due to negative zonal wind shear (Figure 4.24). Thus, the midlatitude disturbance persists and can grows by the interaction with high latitudes as previously explained.

On the other hand, the composite averages of EKE and $\partial K'/\partial t$ for the wave-1 amplification events in March (QBOw) and January do not show any area of $\partial K'/\partial t \geq 0$ before the central date (Figure 4.25). In this environment, the middle latitude disturbance tends to decay and doesn't make the planetary wave amplification events.

The sign of the EKE-to-ZKE conversion is dependent on the meridional distribution of the zonal-mean zonal wind because the eddy momentum flux is mostly positive in the winter stratosphere. Composite difference between the wave-1 amplification events in QBOe and QBOw shows the statistically significant difference in $\partial\bar{u}/\partial y$ and $-\overline{u'v'}(\partial\bar{u}/\partial y)$. The middle latitude $\partial\bar{u}/\partial y < 0$ provides an important condition to keep the EKE to grow the small disturbance into the high latitudes.

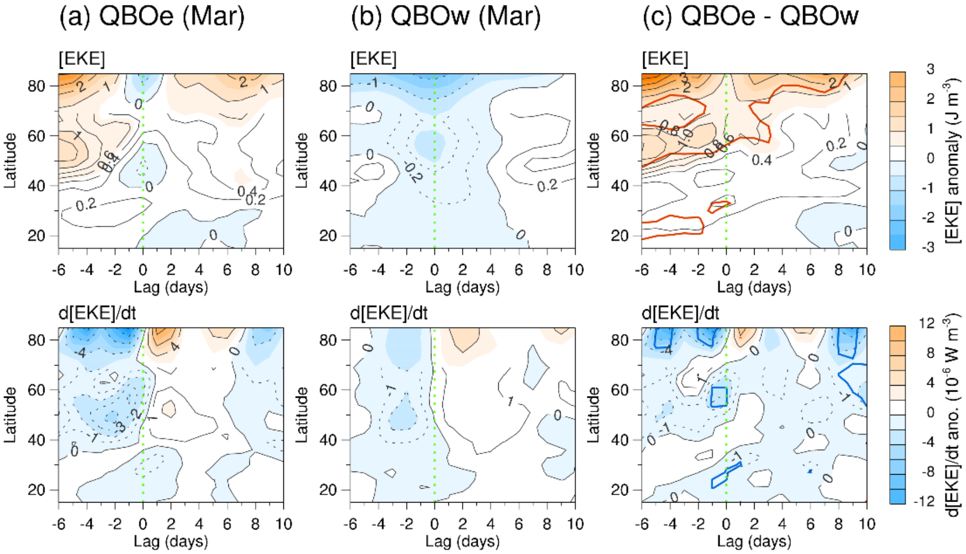

Figure 4.23 Composite averages of the climatological anomalies of eddy kinetic energy (EKE) and rate of change in EKE ($\partial K'/\partial t$) on time-latitude sections at 3 hPa for the (a) QBOe events (N = 19) and (b) QBOw events (N = 18) in March. (c) Composite differences between the QBOe and QBOw events. Areas enclosed by red and blue lines represent that the difference is statistically significant at the 95% level.

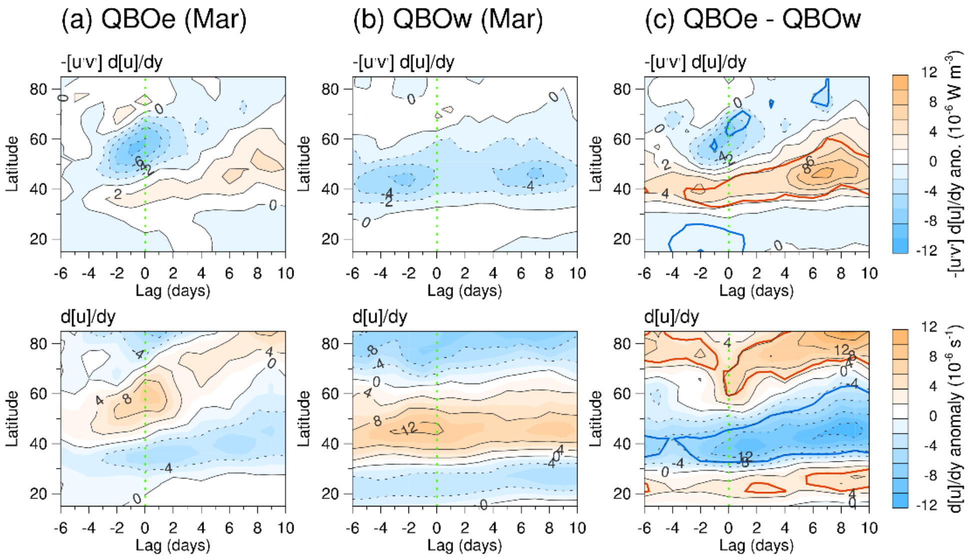

Figure 4.24 Composite averages of the climatological anomalies of zonal-mean kinetic energy (ZKE) to eddy kinetic energy (EKE) conversion ($-\overline{u'v'}(\partial\bar{u}/\partial y)$), and meridonal zonal wind shear ($\partial\bar{u}/\partial y$) on time-latitude sections at 3 hPa for the (a) QBOe events (N = 19) and (b) QBOw events (N = 18) in March. (c) Composite differences between the QBOe and QBOw events. Areas enclosed by red and blue lines represent that the difference is statistically significant at the 95% level.

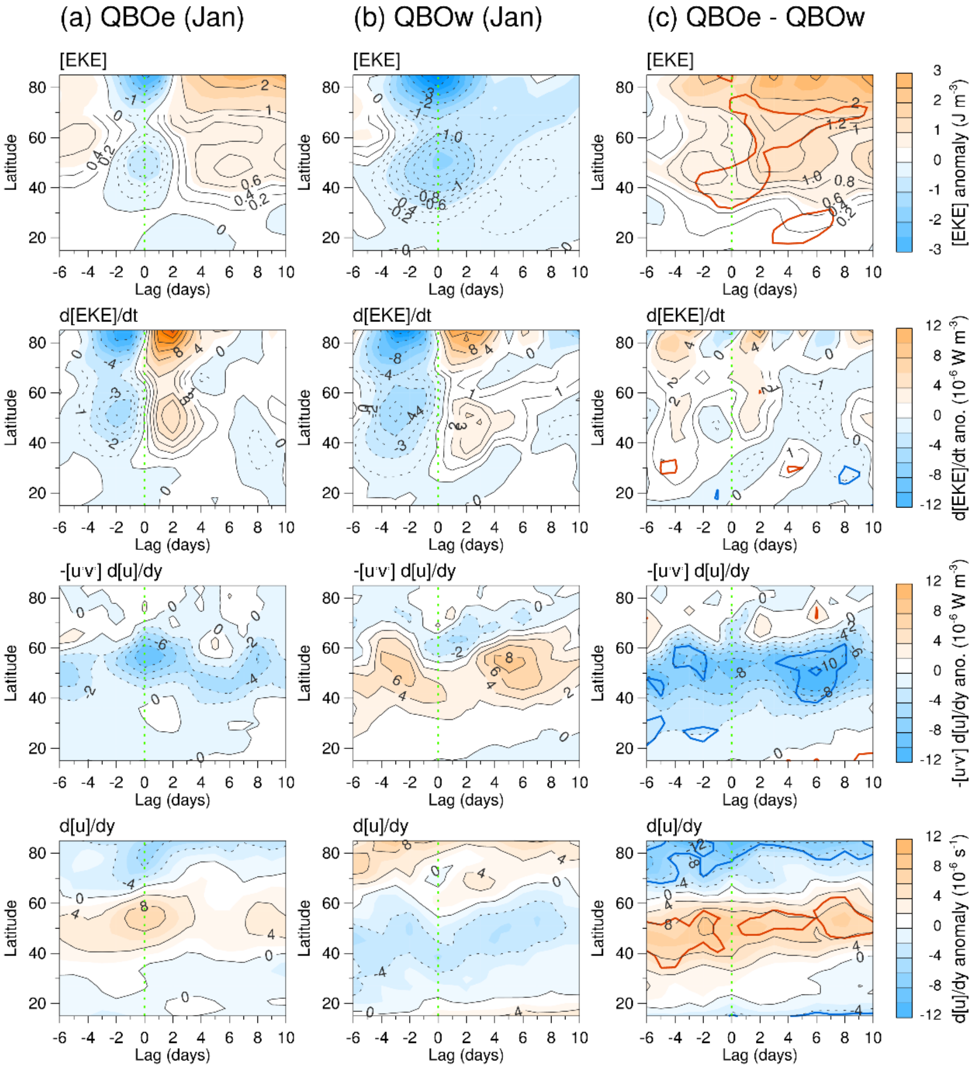

Figure 4.25 The same as in Figures 4.22 and 4.23, but for the QBOe events (N = 49) and QBOw events (N = 14) in January.

4.4. Dynamic Mechanism of QBO Modulation on Planetary Waves in NH Spring

4.4.1. Secondary meridional circulation

In this section, composite mean of the dynamic variables are used to determine if the concept developed in the previous section could be applied to all the QBOe and QBOw years. In Figure 4.26, the composite means of the variables at 3 hPa in January and March, and the large amplitude in March, are shown in both QBOe and QBOw phases. As shown in Figure 4.26, the high-latitude monthly mean wave-1 amplitude was significantly larger during QBOe(L) years than QBOw(L) years in March, with less significant differences being seen in January. These differences were consistent with those in Figure 4.4. Figure 4.26b shows significant differences in EKE at high latitudes in March, and EKE in January at 60°N also had large values in QBOe years.

The composite mean of energy conversion from ZKE to EKE is shown in Figure 4.26c. In January the sign of the energy conversion from ZKE to EKE at middle latitudes, particularly the 40–60°N belt, was negative in both QBOe and QBOw phases. In both QBO phases, the negative energy conversion in the middle latitudes provided unfavorable conditions for the growth of middle latitude perturbations. In March, however, the ZKE-to-EKE conversion had the opposite sign between the two phases of the QBO. The positive energy conversion in the middle latitudes in QBOe increased the eddy wave energy, while negative conversion was seen in QBOw. These energy conversion signs in March (Figure 4.26c) were consistent with the eddy development in 1994 and 1995, which were QBOe(L) and QBOw(L) years, respectively. In QBOe phase, the middle-latitude disturbance grew by obtaining energy from the ZKE through the positive ZKE-to-EKE energy conversion.

The determining factor of the energy conversion was the sign of $\partial\bar{u}/\partial y$, because the eddy momentum flux was mostly positive (Figures 4.8a and 4.8d). To determine the difference in $\partial\bar{u}/\partial y$, the zonal wind and its meridional shear were calculated (Figures 4.26d and 4.26e). For positive energy conversion from ZKE to EKE, a negative $\partial\bar{u}/\partial y$ is required. A decrease in zonal wind with increasing latitude was found from 30°N to 50°N during QBOe in March (Figure 4.26d), which was related to the negative $\partial\bar{u}/\partial y$ around 40°N (Figure 4.26e).

Energy conversion from ZKE to EKE seems essential for a large amplitude in the high-latitude planetary waves. One crucial condition for this is a negative $\partial\bar{u}/\partial y$, which appeared only in QBOe(L) in March. Therefore, the meridional distribution of zonal wind could produce favorable conditions for wave growth. During the different QBO phases, the distributions of the zonal wind in the tropical and middle-latitude regions were influenced by the meridional secondary circulation. The equatorial westerly and easterly shears coincided with warm and cold anomalies, respectively, indicating a thermal wind relationship (Plumb and Bell, 1982; Baldwin et al., 2001; Choi et al., 2002). In the warm and cold anomalies at the equator, a secondary meridional circulation appeared with a sinking and rising motion, respectively.

To examine the relationship between the $\partial\bar{u}/\partial y$ and secondary circulation, the differences in the composite mean of the monthly mean RMC

($\bar{v}^*$, $\bar{w}^*$) and zonal-mean temperature ($\bar{T}$), zonal wind and its meridional shear, EP flux, and EPFD between QBOe and QBOw in January and March were calculated (Figure 4.27). Figure 4.27a shows the differences in zonal-mean zonal wind. The maximum difference occurred at 10 hPa because the phase of the QBO was determined by the zonal wind at 10 hPa. There was an increase in the westerly in the high-latitude region in January. In March, however, the decrease in zonal wind was significant northward of 40°N. At the equator, the westerly shear at 3 hPa and easterly shear at 30 hPa in Figure 4.27a coincided with the warm and cold anomalies at those levels (Figure 4.27b). The equatorial secondary circulation at 3 hPa had a sinking motion, and induced a rising motion at middle latitudes and sinking motion at high latitudes. The sinking motion was particularly strong in the large-amplitude March QBOe, and was associated with high-latitude warming and weakening of the polar jet. In January, however, the high-latitude cooling in the lower and middle stratosphere in QBOe enhanced the polar vortex in the mid-to-upper stratosphere through the thermal wind relationship. The QBO-related changes in temperature, RMC, and zonal wind in January shown in Figures 4.27a and 4.27b were generally consistent with the results from Yamashita et al. (2011), who investigated the effects of the 50 hPa QBOw/10 hPa QBOe for the northern winter (DJF).

Note that the QBO-related changes in RMC in Figure 4.27b is consistent with the SBUV (ver. 8.6) column ozone data (Figure 4.28). The zonal-mean column ozone amounts of the upper-stratospheric layers are lower at the tropics and higher at the subtropics in QBOe compared to QBOw, which is consistent with the QBO-induced meridional transport (Figure 4.27b). The high-latitude column ozone amount is, on the other hand, higher in QBOe at the middle and lower stratospheric layers (below ~6 hPa) (Figure 4.28). This shows that the dynamical response of planetary waves to the QBO in March and its potential influence on the springtime high-latitude ozone in the stratosphere.

The QBO-related changes in $\partial\bar{u}/\partial y$ shown in Figure 4.27c were consistent with the changes in zonal wind. The middle-latitude decrease in $\partial\bar{u}/\partial y$ in QBOe (between 30°N and 50°N) was statistically significant over the upper stratosphere in March (Figure 4.27c). Therefore, the different responses to zonal wind and meridional shear thereof in QBO between January and March at 3 hPa (Figures 4.27d and 4.27e) are likely attributable to the QBO-related changes in RMC and $\bar{T}$ seen in the high latitudes.

To examine QBO-related differences in propagation of the planetary wave, the EP flux and its divergence are shown in Figure 4.27d. In January, the divergence in the EP flux was large. However, considering the average magnitude of the EP flux, which was much larger in January than March, the percentage change in the EP flux in March was larger (Figure 4.29). In January, planetary waves propagated equatorward and upward during the easterly phase of the QBO, as noted in Naoe and Shibata (2010). At high latitudes, there were no statistically significant QBO-related differences in the EPFD. In March, however, QBO-related changes were observed at high latitudes, and statistically significant differences in EP flux convergence in QBOe were observed in the high-latitude upper stratosphere. The convergence anomaly of the EPFD (Figure 4.27d) was balanced by the enhanced northward component of the RMC in the upper stratosphere (Figure

4.27b). The RMC anomaly in the high-latitude upper stratosphere induces stronger sinking and warming anomalies in the high-latitude stratosphere (Figure 4.27b). In March, therefore, the high-latitude temperature, zonal wind, RMC, and EP flux anomalies were consistently maintained by the equatorial QBO through secondary circulation.

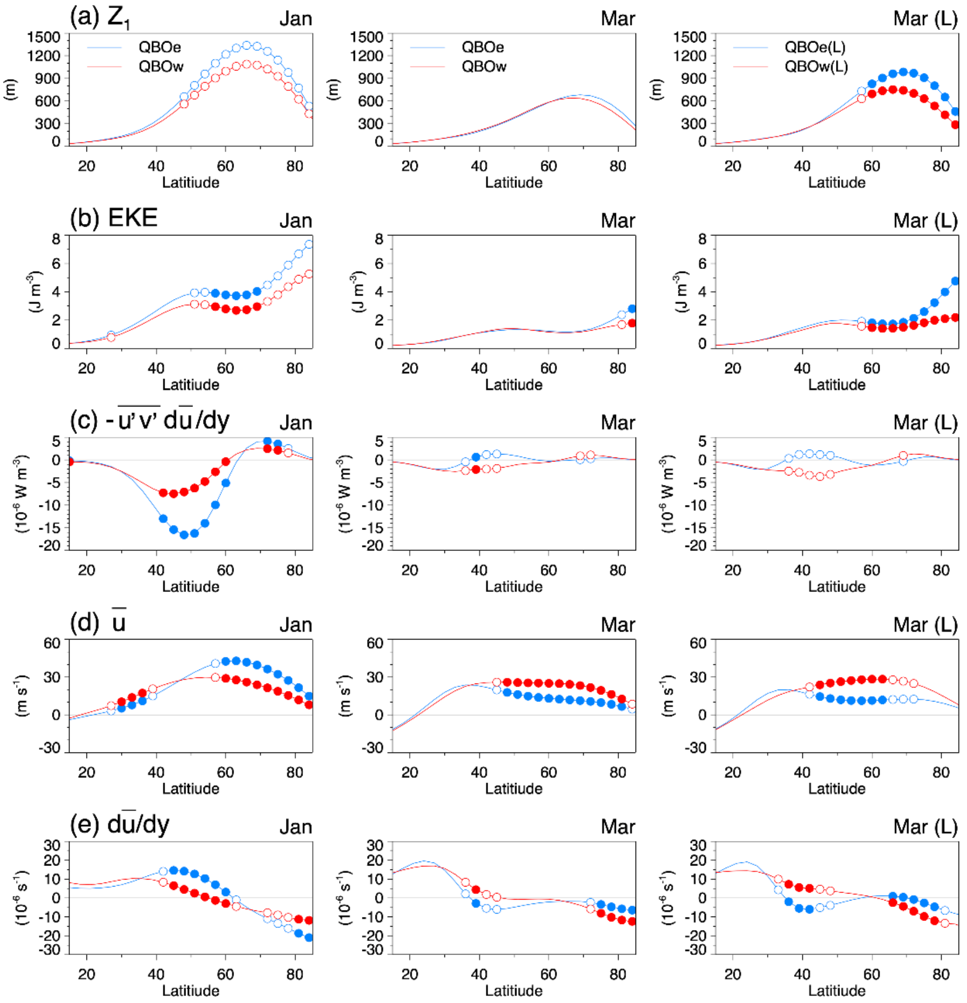

Figure 4.26 Composite mean of monthly (a) wave-1 amplitude, (b) EKE, (c) conversion of ZKE to EKE, (d) $\bar{u}$, and (e) $\partial\bar{u}/\partial y$ for January, March, and large-amplitude March. The blue and red curves denote QBOe and QBOw composites, respectively. Open and solid circles indicate that the difference is statistically significant at the 90% and 95% levels, respectively.

(a) Zonal mean zonal wind

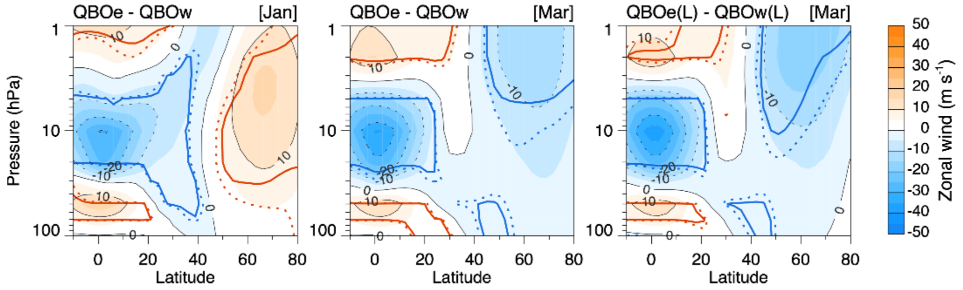

(b) RMC and zonal mean temperature

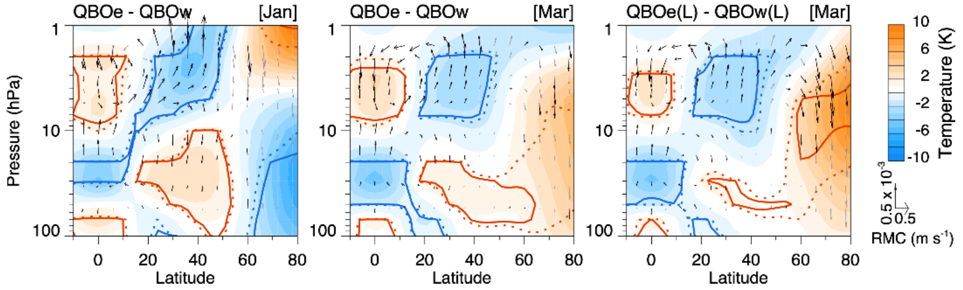

(c) Meridional shear of zonal wind

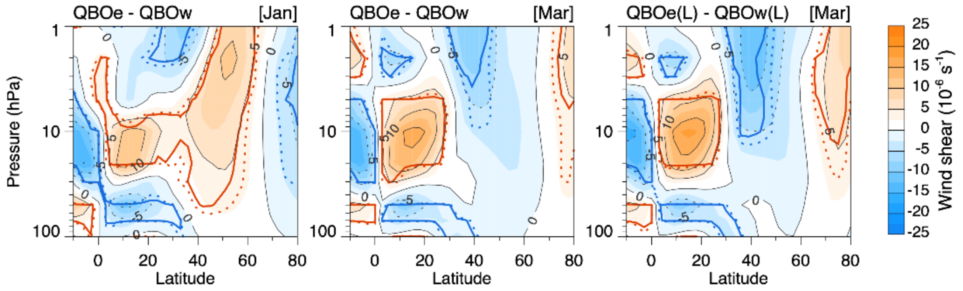

(d) EP-flux and EP-flux divergence

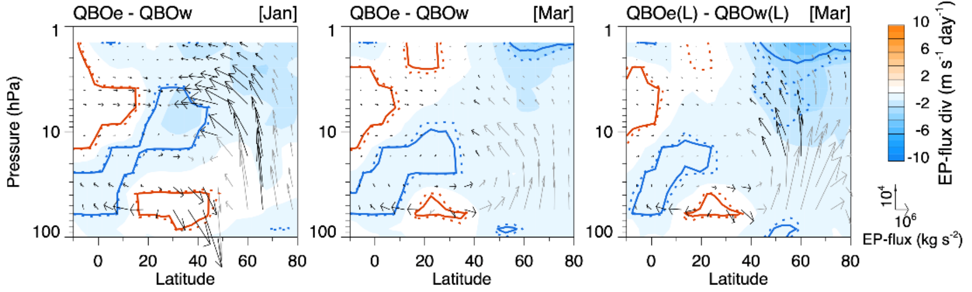

Figure 4.27 Differences in composite monthly means between QBOe and QBOw of (a) zonal wind, (b) RMC (indicated by arrows) and zonal-mean temperature (indicated by shading), (c) meridional shear of zonal-mean zonal wind, and (d) EP flux (indicated by arrows) and EPFD (indicated by shading). The left, center, and right columns are for January, March, and large-amplitude March, respectively. Dotted and solid lines indicate that the differences are statistically significant at the 90% and 95% levels, respectively.

The black arrows indicate a statistical significance at the 95% level; gray arrows indicate significance at 90%. The reference arrow scales are (a) 0.5 m s^{-1} for $\bar{v}^*$ and 0.5×10^{-3} m s^{-1} for $\bar{w}^*$, and (c) 10^6 and 10^4 kg s^{-2} for the meridional and vertical EP flux components, respectively.

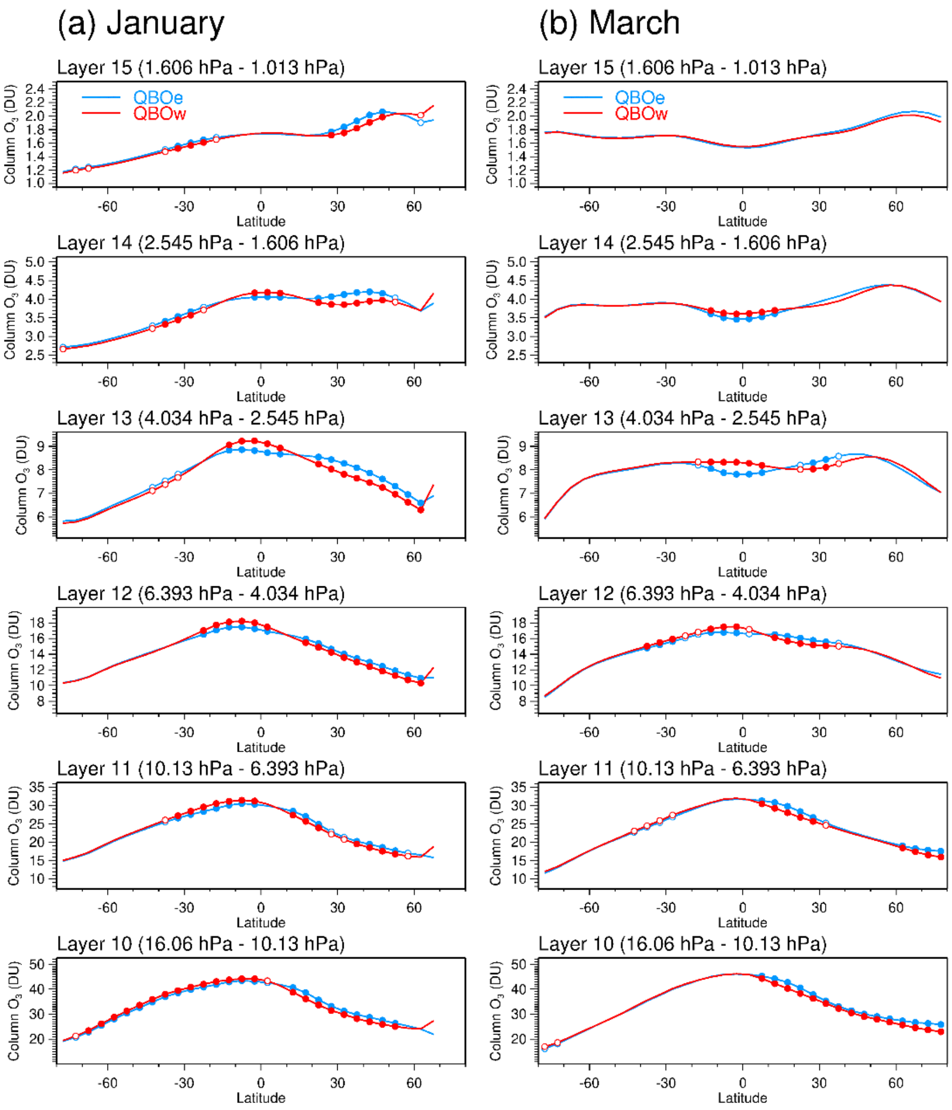

Figure 4.28 Composite averages of the column ozone distribution at each pressure layer derived from the SBUV ozone data sets from 1979 to 2018 for the QBOe and QBOw years in (a) January and (b) March. The filled and open circles represent that the composite difference between QBOe (blue) and QBOw (red) is statistically significant at the 90% and 95% levels, respectively.

(a) Vertical EP flux (F_z)

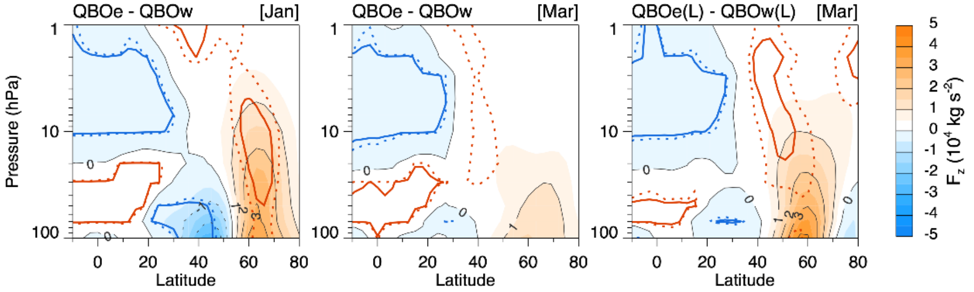

(b) F_z / $F_{z\,CLM}$

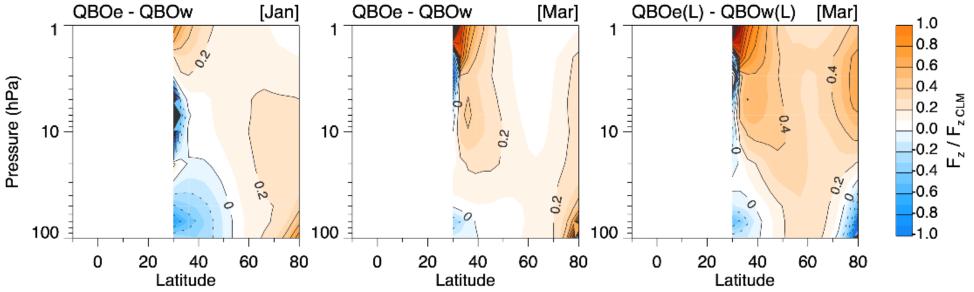

Figure 4.29 Differences in composite monthly means between QBOe and QBOw of the (a) vertical EP flux (F_Z; indicated by shading with an interval of 10^4 kg s^{-2}) and (b) F_Z normalized by the climatological average of the vertical EP flux ($F_{Z\,CLM}$) ($F_Z/F_{Z\,CLM}$). The left, center, and right columns are for January, March, and large-amplitude March, respectively. The dotted and solid lines in (a) indicate that the differences were statistically significant at the 90% and 95% levels, respectively.

4.4.2. General circulation model simulations

To examine the dynamic response of the planetary waves to different QBO profiles, GCM simulations are required. In this study, WACCM4 was employed and run with fixed SST and sea ice data as a lower boundary condition. For chemistry, perpetual AD 2000 emission inventory with specified chemistry (SC) was applied. Considering the probable influence of the upper stratosphere and lower mesosphere wind profiles (e.g., semi-annual oscillation), four equatorial zonal wind profiles were prepared (Table 4.3 and Figure 4.30): the January and March climatology from the SPARC climatology (Figure 4.30a) and the QBOe and QBOw anomalies in the stratosphere from the ERA-Interim reanalysis (Figure 4.30b). The relaxed equatorial zonal wind profiles in the model successfully represent the 10 hPa QBO together with intra-seasonal differences in the upper-stratospheric zonal winds (Figures 4.30c and 4.30d). Each simulation was conducted for 55 years, and this study used 49 winter periods excluding the first five years as a spin-up periods.

The 49-year climatological time series of the polar cap height (GPH averaged over 65–90°N) and the high-latitude wave-1 amplitude for four WACCM experiments show the lower polar cap heights and the larger wave-1 amplitudes compared to those in the ERA-Interim reanalysis data from late winter to early spring (February to April) (Figure 4.31). As inferred from Figure 4.31b, the wave-1 amplitude in March doesn’t show clear difference between QBOe and QBOw experiments. However, the wave-1 amplitudes in QBOe experiments are clearly larger than that in QBOw experiments in April.

Frequency of the monthly mean wave-1 amplitudes for each WACCM experiments shows that there are no significant differences between the QBOe and QBOw experiments in March. In April, however, the larger wave-1 amplitude in the QBOe-M and QBOe-J experiments compared to the QBOw-M and QBOw-J experiments (Figure 4.32). The colder and longer winter in the WACCM experiments may result in the postponed dynamical responses of the upper stratosphere to the QBO. In model simulations, the equator-to-pole interaction in the upper stratosphere can be masked in March due to stronger vertical propagation of the planetary waves but could be revealed in April due to delayed seasonal transition.

The daily evolution of the high-latitude wave-1 growth at 3 hPa is summarized in Table 4.4. The wave-1 growth in March in the ERA-Interim reanalysis data characterized by the middle-to-high-latitude wave growth with northeastward tilting patterns cannot be found in March but occurred in April in the QBOe-M experiment (Figures 4.33 and 4.34). This type of wave-1 growth pattern is somewhat weaker in the QBOe-J composite in April, and this may be due to the different mesospheric profiles of the equatorial zonal winds between the QBOe-M experiment and the QBOe-J experiment (Figure 4.30c). By the semi-annual oscillation, equatorial zonal wind at the stratopause (~1 hPa) shows strong easterly in January but westerly in March and April (Figure 4.30a). Therefore, the equatorial zonal wind profile for the QBOe-M experiment rather than that for the QBOe-J experiment can be more realistic for the model simulation in April.

In terms of the monthly mean dynamic fields, composite differences of zonal-mean temperature and zonal-mean zonal wind between the QBOe and QBOw experiments well represent responses to the QBO-related secondary circulation in the subtropics and middle latitudes (Figures 4.35 and 4.36) similar to the ERA-Interim reanalysis (Figures 4.27a and 4.27b). In the high latitudes, the composite differences of zonal-mean temperature and zonal wind between the QBOe-J and the QBOw-J experiments are similar to those from the ERA-Interim reanalysis: the warm anomaly near the mesopause and cold anomaly in the lower stratosphere and the increase in the zonal-mean zonal wind in the QBOe. These characteristics are weaker in the QBOe-M and the QBOw-M experiments. Interestingly, the high-latitude responses of temperature and zonal wind in March in observation cannot be found in March but can be found in April in the WACCM simulations: the warm anomaly and significant decrease in the zonal wind in the upper stratosphere in the QBOe-M experiment compared to the QBOw-M experiment.

The WACCM simulation results imply that the dynamic response of the upper stratospheric planetary waves to the QBO and mechanisms of the equator-to-pole interaction can be clearly revealed in the seasonal transition period when the influence of the vertically propagated planetary waves is weak.

Table 4.3 Designs of the WACCM experiments.

Case	Experiments	QBO profiles (100 hPa < p < 1 hPa) (ERA-Interim)	Mesosphere (p < 1 hPa) (SPARC climatology)	Run length
Exp. 1	QBOe-M	Easterly QBO	March	55 Yr
Exp. 2	QBOw-M	Westerly QBO	March	55 Yr
Exp. 3	QBOe-J	Easterly QBO	January	55 Yr
Exp. 4	QBOw-J	Westerly QBO	January	55 Yr

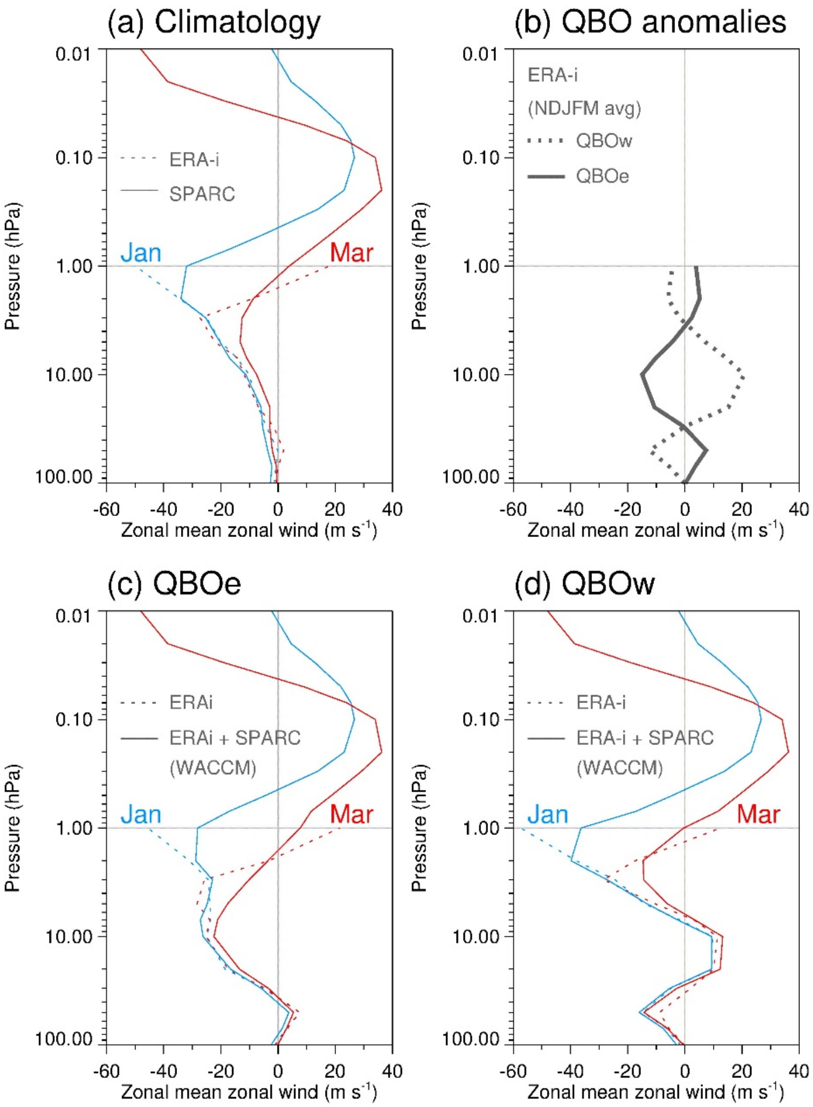

Figure 4.30 (a) Climatological equatorial zonal-mean zonal wind profiles (averaged over 5°S–5°N) in January (blue lines) and March (red lines) derived from the ERA-Interim (dotted lines) and the SPARC climatology (solid lines). (b) Winter-average (November–March) of climatological equatorial zonal wind anomalies for the easterly QBO phase (QBOe) and westerly QBO phase (QBOw) from the ERA-Interim. (c, d) Composite mean of equatorial zonal-mean zonal wind profiles for QBOe and QBOw in ERA-Interim (dotted lines) and zonal-mean zonal wind profiles that relaxed toward in the WACCM experiments (solid lines) for January (blue lines) and March (red lines).

(a) Polar cap height

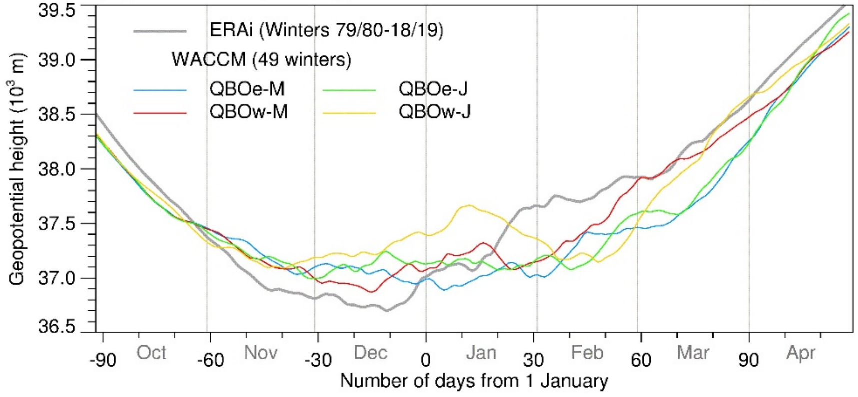

(b) Wave-1 amplitude

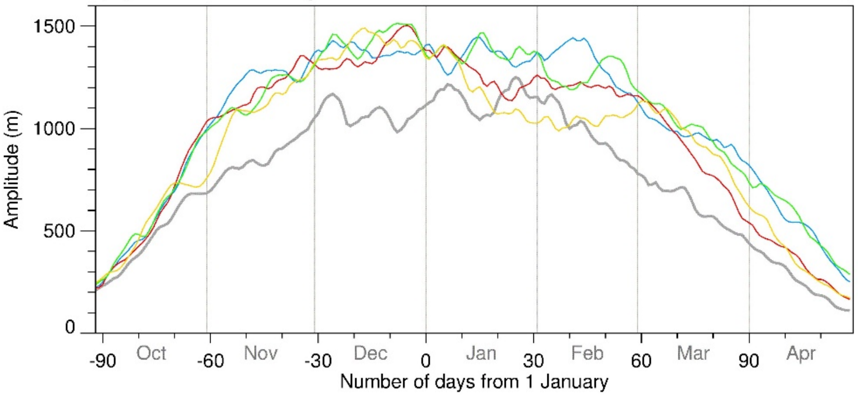

Figure 4.31 Comparisons of climatological time series of (a) polar cap height (GPH averaged over 65–90°N) and (b) high-latitude wave-1 amplitude (averaged over 60–80°N) at 3 hPa from the ERA-Interim reanalysis (1979/1980–2018/2019) and the SC-WACCM simulation results with four different QBO profiles (49 winters).

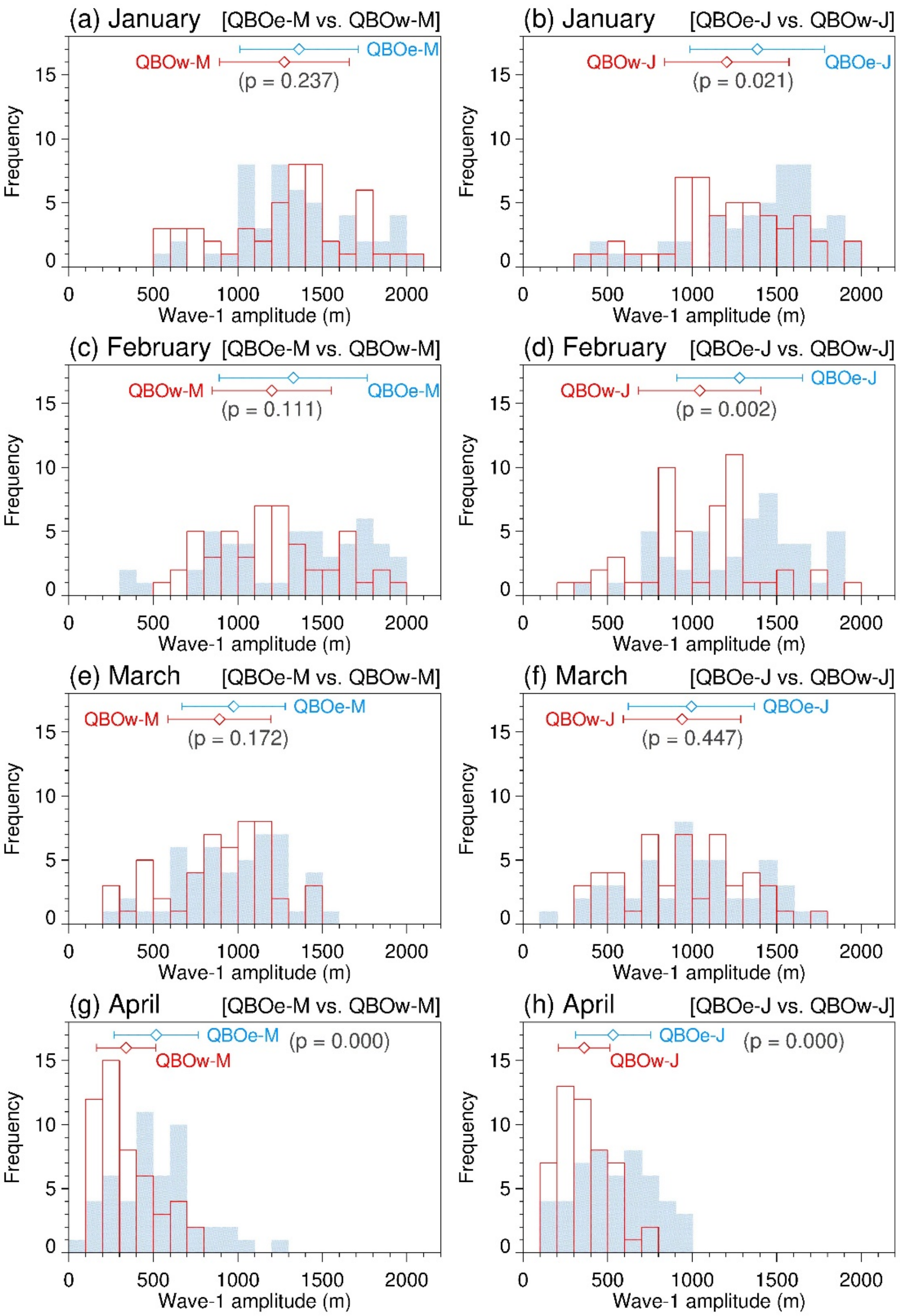

Figure 4.32 Distribution of the monthly mean high-latitude wave-1 amplitudes at 3 hPa from the SC-WACCM experiments.

Table 4.4 Number of the significant wave-1 amplification events (N), that wave-1 amplitude growths are larger than median value from the ERA-Interim reanalysis ($\Delta Z > 275$ m), and the average and standard deviation of wave-1 amplitude growth (ΔZ), wave-1 amplification period (Δt), high-latitude (averaged over 60–80°N) wave-1 and -2 amplitudes (Z_1 and Z_2) for the 49-year WACCM simulations with 4 scenarios of the QBOe-M, QBOw-M, QBOe-J, and QBOw-J.

Month	Scenario	N	ΔZ (m)	Δt (day)	Z_1 (m)	Z_2 (m)
Winter (Oct. to Apr.)	QBOe-M	486	711 ± 373	8.0 ± 4.0	1177 ± 474	273 ± 141
	QBOw-M	496	687 ± 346	8.1 ± 3.9	1127 ± 474	276 ± 135
	p-value [a]		0.283	0.870	0.101	0.736
	QBOe-J	512	720 ± 361	8.0 ± 3.7	1181 ± 485	274 ± 136
	QBOw-J	489	724 ± 358	7.9 ± 3.5	1125 ± 476	275 ± 130
	p-value [b]		0.877	0.588	0.067	0.852
November	QBOe-M	82	704 ± 343	9.4 ± 4.6	1212 ± 333	240 ± 108
	QBOw-M	80	678 ± 275	6.5 ± 3.2	1180 ± 309	234 ± 101
	p-value [a]		0.590	0.254	0.530	0.706
	QBOe-J	85	714 ± 324	8.9 ± 3.9	1208 ± 323	241 ± 99
	QBOw-J	94	719 ± 283	8.0 ± 2.8	1097 ± 348	241 ± 96
	p-value [b]		0.924	0.107	0.029	0.974
December	QBOe-M	87	780 ± 427	7.8 ± 3.9	1412 ± 360	322 ± 137
	QBOw-M	100	756 ± 383	6.7 ± 4.4	1418 ± 408	320 ± 108
	p-value [a]		0.686	0.715	0.921	0.916
	QBOe-J	92	772 ± 380	7.7 ± 3.6	1421 ± 395	339 ± 148
	QBOw-J	99	790 ± 332	6.8 ± 2.7	1439 ± 434	320 ± 124
	p-value [b]		0.723	0.058	0.764	0.319
January	QBOe-M	90	832 ± 438	7.3 ± 3.7	1420 ± 443	331 ± 135
	QBOw-M	96	676 ± 313	6.6 ± 4.0	1293 ± 472	347 ± 153
	p-value [a]		0.006	0.379	0.060	0.457
	QBOe-J	98	778 ± 403	7.6 ± 3.8	1419 ± 510	335 ± 137
	QBOw-J	87	750 ± 436	7.3 ± 3.1	1334 ± 503	354 ± 143
	p-value [b]		0.650	0.470	0.260	0.345
February	QBOe-M	72	685 ± 359	6.8 ± 3.8	1355 ± 497	342 ± 164
	QBOw-M	81	715 ± 443	6.5 ± 4.2	1172 ± 488	316 ± 146
	p-value [a]		0.641	0.307	0.023	0.295
	QBOe-J	73	847 ± 408	7.5 ± 3.1	1324 ± 446	320 ± 128
	QBOw-J	77	785 ± 427	8.0 ± 4.0	1091 ± 424	293 ± 115
	p-value [b]		0.363	0.388	0.001	0.183
March	QBOe-M	70	638 ± 316	7.0 ± 3.3	966 ± 370	253 ± 127
	QBOw-M	52	620 ± 336	5.5 ± 3.0	932 ± 382	249 ± 112
	p-value [a]		0.762	0.865	0.627	0.873
	QBOe-J	70	625 ± 300	6.7 ± 3.1	1056 ± 418	234 ± 120
	QBOw-J	56	675 ± 377	7.5 ± 3.2	1021 ± 378	258 ± 128
	p-value [b]		0.414	0.185	0.618	0.297
April	QBOe-M	21	498 ± 180	7.3 ± 2.8	613 ± 250	156 ± 69
	QBOw-M	14	531 ± 302	6.1 ± 2.8	564 ± 251	193 ± 64
	p-value [a]		0.716	0.784	0.579	0.120
	QBOe-J	28	508 ± 254	7.5 ± 3.5	668 ± 243	186 ± 68
	QBOw-J	11	422 ± 118	8.0 ± 3.9	557 ± 268	156 ± 63
	p-value [b]		0.156	0.719	0.250	0.210

[a] p-values provided by the Welch's t-test for the average difference between QBOe-M and QBOw-M groups

[b] p-values provided by the Welch's t-test for the average difference between QBOe-J and QBOw-J groups

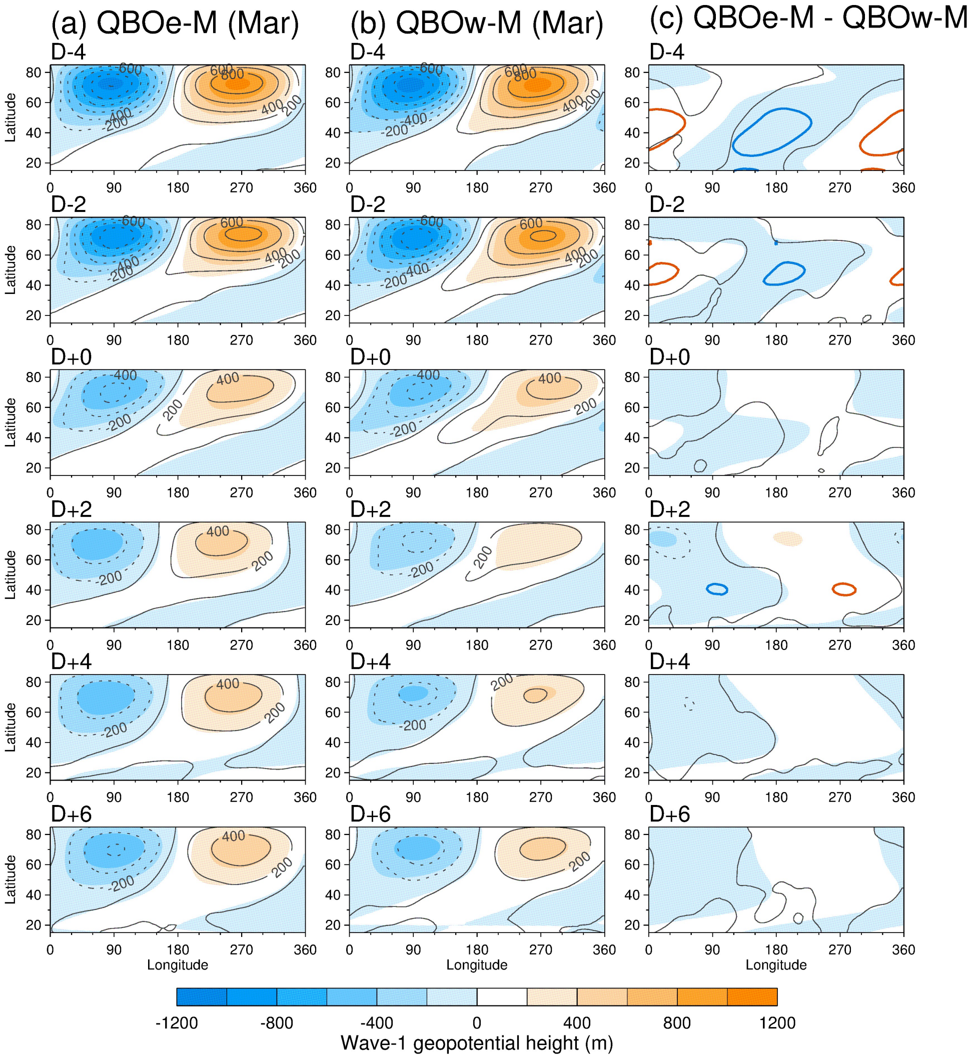

Figure 4.33 Composite averages of the zonal-mean geopotential height anomaly (contours plotted at 200 m intervals) and wave-1 geopotential height (color scale) for the significant wave-1 amplification events (ΔZ > 275 m) in March from the SC-WACCM experiments. (a) QBOe-M profile (N = 70), (b) QBOw-M profile (N = 52), and (c) composite difference between the QBOe-M and QBOw-M events. Areas enclosed by red and blue lines represent that the difference is statistically significant at the 95% level.

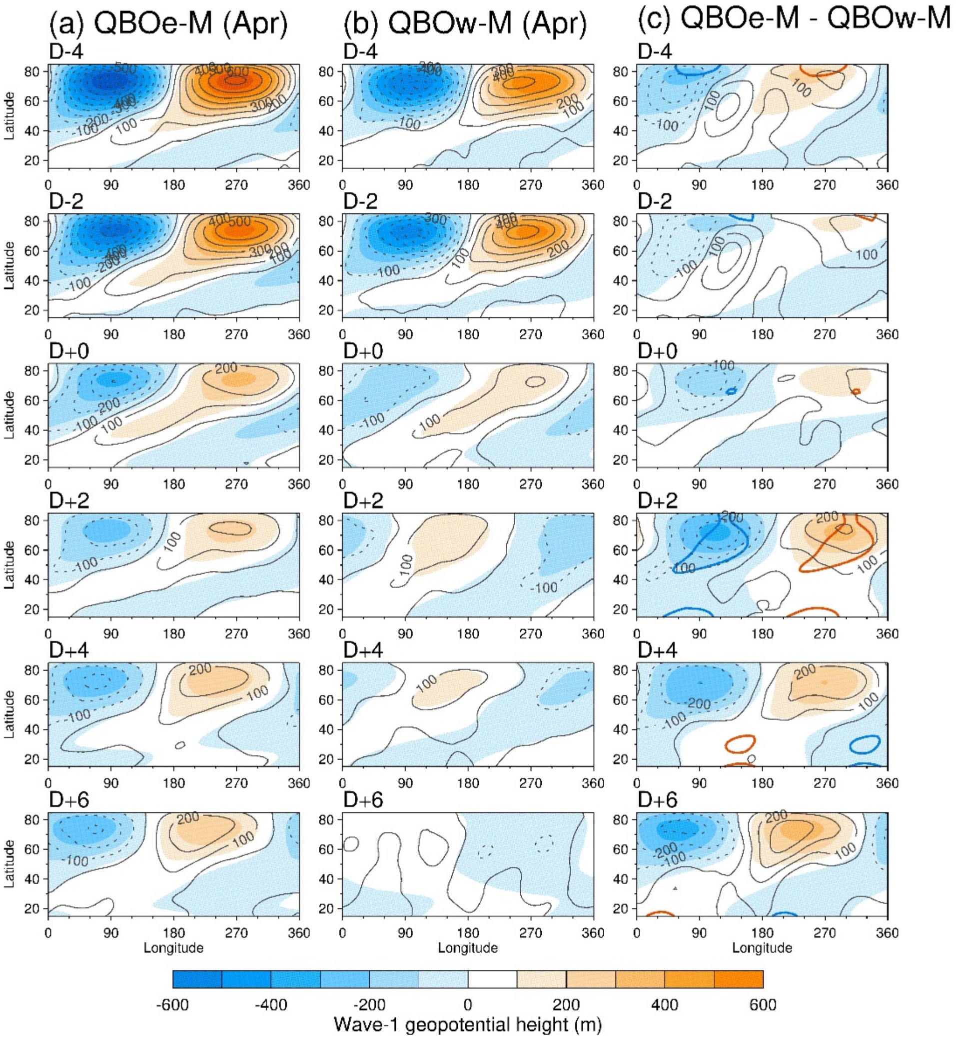

Figure 4.34 Composite averages of the zonal-mean geopotential height anomaly (contours plotted at 100 m intervals) and wave-1 geopotential height (color scale) for the significant wave-1 amplification events ($\Delta Z > 275$ m) in April from the SC-WACCM experiments. (a) QBOe-M profile (N = 21), (b) QBOw-M profile (N = 14), and (c) composite difference between the QBOe-M and QBOw-M events. Areas enclosed by red and blue lines represent that the difference is statistically significant at the 95% level.

(a) QBOe-M minus QBOw-M

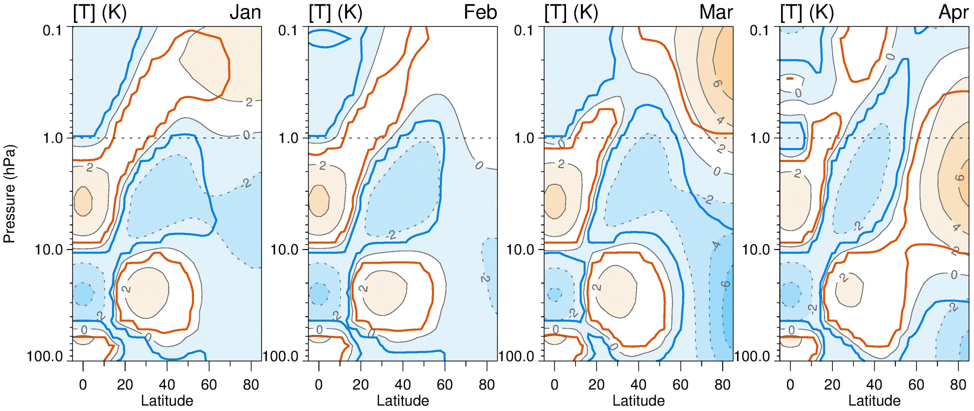

(b) QBOe-J minus QBOw-J

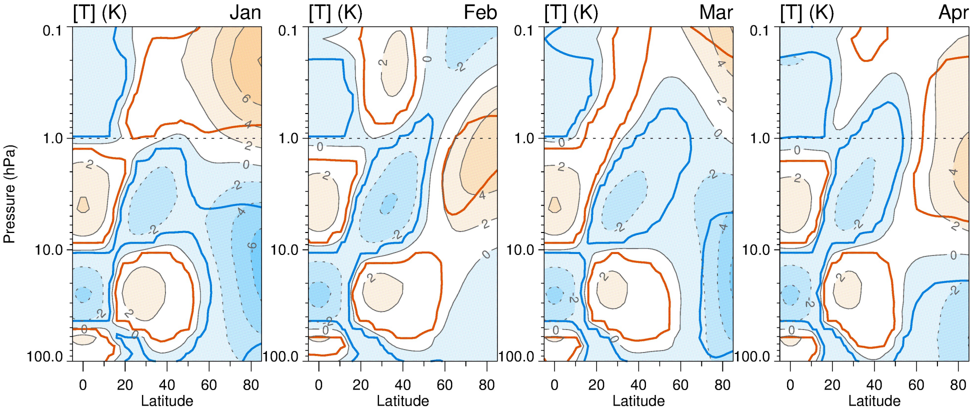

Figure 4.35 Differences in composite monthly mean temperature between (a) QBOe-M and QBOw-M experiments and (b) QBOe-J and QBOw-J experiments. Areas enclosed by red and blue lines represent that the difference is statistically significant at the 95% level.

(a) QBOe-M minus QBOw-M

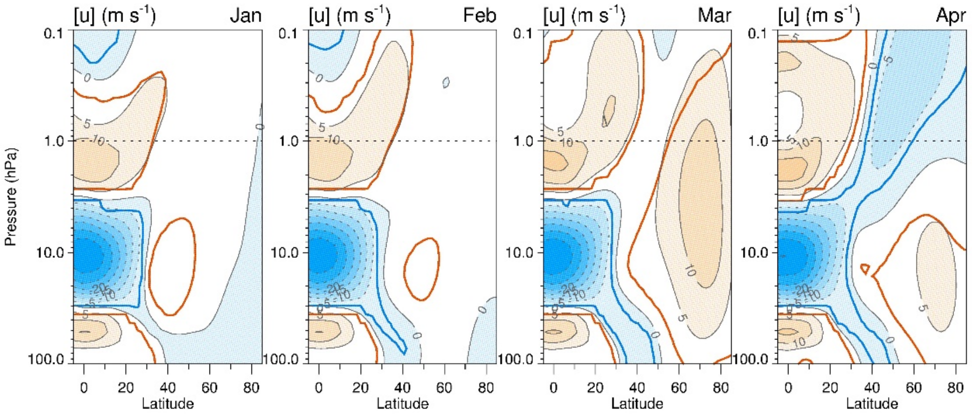

(b) QBOe-J minus QBOw-J

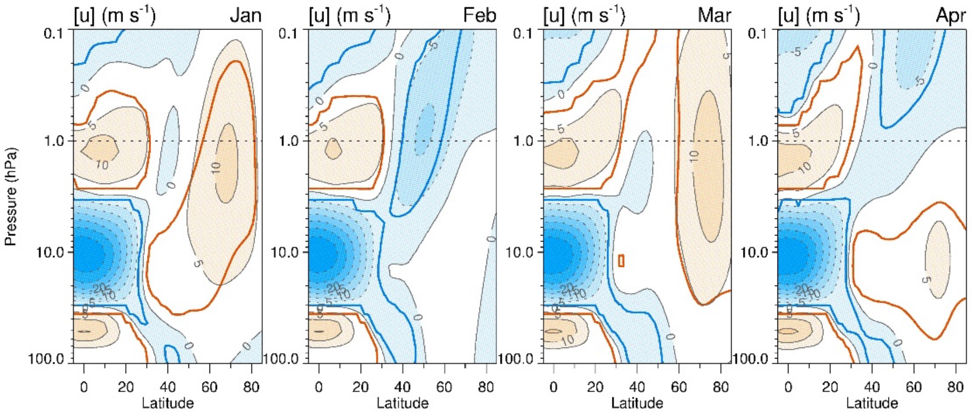

Figure 4.36 The same as Figure 4.35, but for the monthly mean zonal wind.

5. Summary and Conclusions

The evolution and interannual variability of the polar vortex and planetary waves on the upper stratosphere in NH spring were investigated. Breakup of the polar vortex in the stratosphere is an important dynamical phenomenon in seasonal transition from winter to spring, and determining its date has significant potential for understanding climate change. In previous studies the date of vortex breakup has been diagnosed using three methods: "PV area", "PV and U", and "U area". All of these methods were used successfully for the lower stratosphere near the 450–500 K isentropic levels following some "tuning" of key parameters (Waugh et al., 1999). In the upper stratosphere, however, subjectively choosing the parameters is more difficult due to the complex features in the vortex evolution.

In alternative manner, the temporal change of the EL, MPV, and zonal wind at the vortex edge are focused because those are observed to change significantly at the time of vortex breakup and formation. Based on these observations, the dates of the formation and breakup of the polar vortex are defined by finding the maximum peaks in the averaged rates of change in EL, MPV, and wind speed at the vortex edge. The “edge-change” method was applied to 22 isentropic levels in both the NH and SH from 380 K (~ 15 km) to 1260 K (~41 km) for the period 1979–2018, using the ERA-Interim reanalysis data. The onset and breakup dates of the polar vortices generally start from the upper stratosphere and propagate downwards to the lower stratosphere. For the lower stratosphere, the “edge-change” method shows similar results to those obtained by the other three diagnostic methods from previous studies.

The newly-defined vortex breakup dates are compared with the SFW, which is another diagnostic for the end of the stratospheric vortex. The dates of the SFW are close in both the lower and upper stratosphere, while the vortex breakup dates mostly appear later in the lower stratosphere. Usually the SFW date is not very sensitive to the choice of threshold value. In some cases, however, the SFW date can be different by up to two months when the midwinter SSW occurs. Therefore, the vortex breakup date seems to be dynamically consistent throughout the stratosphere and could be more useful for observing interannual changes in the polar vortex.

The polar vortex plays as a transport barrier for stratospheric trace gases, and thus, analysing tracer concentrations along with the evolution of the vortex is useful in understanding the stratospheric transport. Comparison between the dates of polar vortex breakup and the evolution of the CH_4 and O_3 mixing ratios show that discontinuities of tracer concentrations through the EL became much smaller just after the breakup date. Furthermore, zonal standard deviation of the tracer mixing ratio following the latitude circle decreases significantly after the dynamically obtained vortex breakup date. These observations apply to both the upper and lower stratosphere, and in both the NH and SH. Using these observations, determining the date of the vortex breakup by the "edge-change" method seems to be supported by transport of tracers. Therefore, the newly-defined vortex breakup dates based on the “edge-change” metric could be an acceptable diagnostic for the polar vortex in both the lower and upper stratosphere.

In terms of interannual variability in the stratospheric planetary waves, dynamical responses of upper-stratospheric planetary waves to the equatorial QBO in NH spring was investigated.

The wave-1 amplitude at 3 hPa at high latitudes is larger in March during QBOe than during QBOw. The phase of the QBO was determined by the 10 hPa zonal wind at the equator. The differences observed in March were not observed in January or February. Case studies were conducted for two wave growth events in March in 1994 and 1995. Various dynamical variables were analyzed in association these two events, including the eddy flux, EP flux and its divergence, QGPV and QG potential enstrophy, EKE, and RMC. An important factor determining the high-latitude wave growth in March 1994 seems to be the low-latitude zonal-mean-to-eddy kinetic energy conversion seen in the early stage and is characterized by the middle-to-high-latitude wave growth.

A schematic diagram of the changes in dynamic variables at each latitude band during the wave-1 growth in March 1994 is represented in Figure 5.1. At first, in the low latitudes (20–30°N), EKE increased with time and reached a maximum on 21 March, consistent with the continuous kinetic energy conversion from 18 March. In the middle latitudes (30–40°N), the energy conversion reached a maximum on 23 March. The wave started to develop in the 30–40°N region as it moved northeastward during 18–26 March, consistent with a middle latitude negative $\overline{v'q'}$. In the 40–60°N latitude band, the negative $\overline{v'q'}$ gradually increased until 25 March. At high latitudes (60–80°N), $\overline{v'q'}$ rapidly increased to a maximum on 26 March. Finally, the maximum wave-1 amplitude appeared on 28 March.

Based on the observation of these variables, a dynamical mechanism drove the amplification of high-latitude planetary waves during the easterly QBO in March. During QBOe, the secondary meridional circulation produced the westerly anomaly at 30°N and 3 hPa, which is associated with vertical wind shear at the equator. This type of zonal wind distribution yielded the negative $\partial\bar{u}/\partial y$ anomaly, and subsequently enhanced conversion from ZKE to EKE in the middle latitudes. The wave energy of the middle-latitude waves that grew via this energy conversion was transported to the high-latitude region by the PV flux. The middle-to-high-latitude wave development occurring with eastward movement during the wave-1 growth in March 1994 was also reflected in the evolution of potential enstrophy. The wave-1 development was consistent with the northeastward tilt of the perturbation. Such wave growth in a short period may result in a larger monthly mean planetary wave amplitude.

The dynamical mechanism suggested by the case study on wave-1 events in March 1994 and 1995 was generalized by the composite analyses for the QBOe and QBOw years in March. However, the dynamic characteristics of the wave-1 growth in the QBOe-composite in March do not appear in January. Figure 5.2 represents the schematic diagram of the dynamical mechanism of equator-to-pole interaction in March. The QBO-related changes in RMC and middle latitude zonal-mean zonal wind induce the changes in the meridional gradient of zonal wind and affect the EKE-to-ZKE conversion in the middle latitudes. The middle latitude eddy can grow through the wave–mean flow interaction and induce the interannual variability in the high-latitude planetary waves.

In GCM model experiments using the WACCM4 with different QBO profiles, the wave-1 growth pattern similar to that in March QBOe years occurred in April instead of March. The monthly mean wave-1 amplitude at 3 hPa was also significantly larger in the QBOe simulation compared to the QBOw simulation in April. The delayed response of the planetary waves to the QBO may be related to the colder and longer winter bias in the WACCM climate. The influence of the QBO in the tropical to the high-latitude region during winter was masked by the large planetary wave activity. Under the same amount of forcing, the effect could be revealed in March, when there is a lack of strong planetary wave propagation. Accordingly, a larger amplitude was only associated with the equatorial QBOe in March.

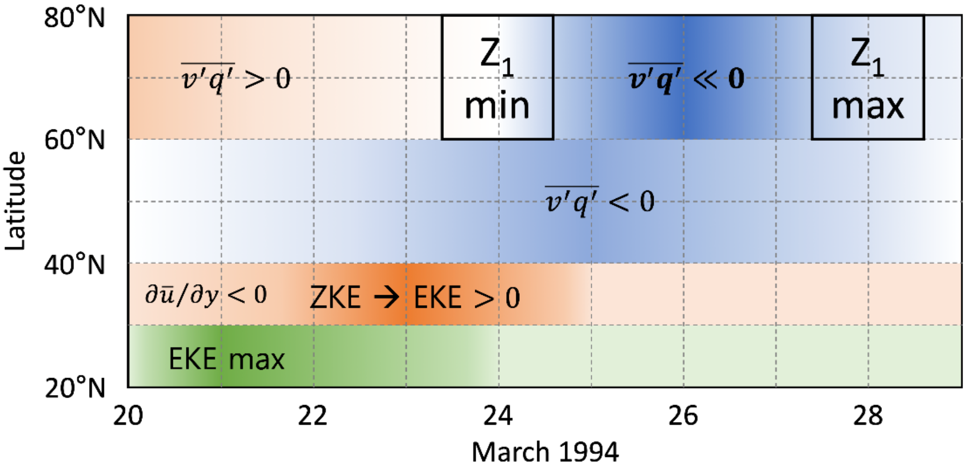

Figure 5.1 Schematic diagram representing changes in dynamic variables in each latitude band during Event 94. In the low latitudes (20–30°N), the maximum EKE occurred on 21 March. In the middle latitudes (30–40°N), the energy conversion reached a maximum on 23 March. In the 40–60°N latitude band, the negative $\overline{v'q'}$ had gradually increased by 25 March, 1994. In the high latitudes (60–80°N), the sign of $\overline{v'q'}$ changed from positive to negative on the minimum Z_1 day (24 March, 1994) and reached its negative maximum on 26 March, 1994. Finally, the maximum Z_1 appeared on 28 March, 1994.

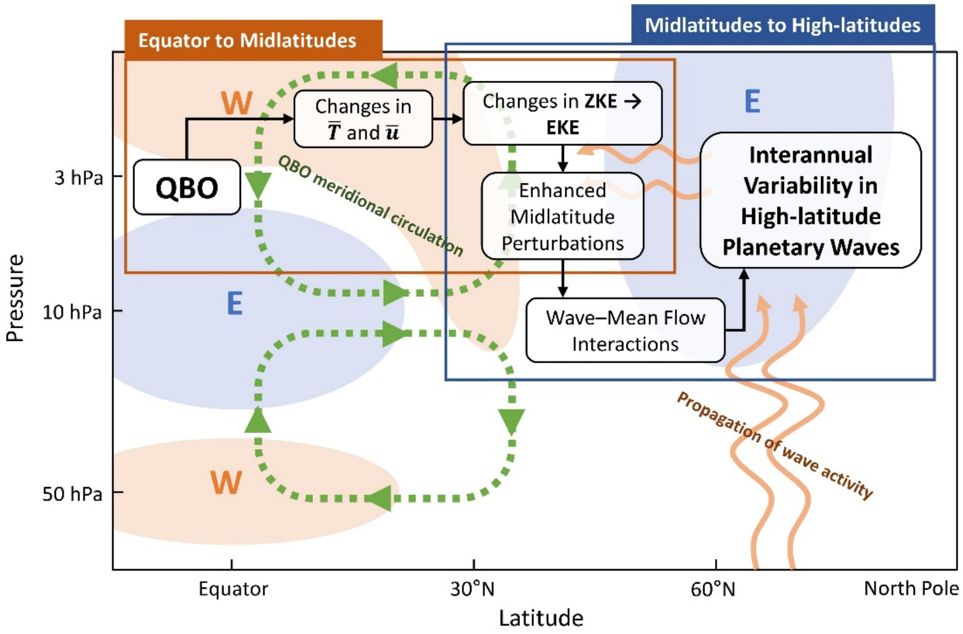

Figure 5.2 Schematic diagram of the equator-to-pole interaction between the QBO and interannual variability of the high-latitude planetary waves in the upper stratosphere in March.

References

Andrews, D. G., J. R. Holton, and C. B. Leovy, 1987: Middle Atmosphere Dynamics. Int. Geophys., No. 40. Academic Press, New York, 489 pp.

Andrews, D. G., and M. E. McIntyre, 1976: Planetary waves in horizontal and vertical shear: The generalized Eliassen-Palm relation and the mean zonal acceleration. J. Atmos. Sci., 33, 2031–2048.

Baldwin, M. P., and T. J. Dunkerton, 2001: Stratospheric harbingers of anomalous weather regimes. Science, 294, 581–584.

Baldwin, M. P., L. J. Gray, T. J. Dunkerton, K. Hamilton, P. H. Haynes, W. J. Randel, J. R. Holton, M. J. Alexander, I. Hirota, T. Horinouchi, D. B. A. Jones, J. S. Kinnersley, C. Marquardt, K. Sato, and M. Takahashi, 2001: The quasi-biennial oscillation. Rev. Geophys., 39, 179–229.

Baldwin, M. P., D. B. Stephenson, D. W. J. Thompson, T. J. Dunkerton, A. J. Charlton, and A. O'Neill, 2003: Stratospheric memory and skill of extended-range weather forecasts. Science, 301, 636–640.

Baldwin, M. P., and L. J. Gray, 2005: Tropical stratospheric zonal winds in ECMWF ERA-40 reanalysis, rocketsonde data, and rawinsonde data. Geophys. Res. Lett., 32, L09806.

Black, R. X., B. A. McDaniel, and W. A. Robinson, 2006: Stratosphere–troposphere coupling during spring onset. J. Climate, 19, 4891–4901.

Black, R. X., and B. A. McDaniel, 2007: The dynamics of Northern Hemisphere stratospheric final warming events. J. Atmos. Sci., 64, 2932–2946.

Butchart, N., and E. E. Remsberg, 1986: The area of the stratospheric polar vortex as a diagnostic for tracer transport on an isentropic surface. J. Atmos. Sci., 43, 1319–1339.

Charney, J. G. and P. G. Drazin, 1961: Propagation of planetary-scale disturbances from the lower into the upper atmosphere. J. Geophys. Res., 66, 83–110.

Choi, H., B.-M. Kim, and W. Choi, 2019: Type classification of sudden stratospheric warming based on pre- and postwarming periods. J. Climate, 32, 2349–2367.

Choi, W., S. Kim, W. B. Grant, M. Shiotani, Y. Sasano, and M. R. Schoeberl, 2002a: Transport of methane in the stratosphere associated with the breakdown of the Antarctic polar vortex. J. Geophys. Res., 107, 8209.

Choi, W., H. Lee, W. B. Grant, J. H. Park, J. R. Holton, K.-M. Lee, and B. Naujokat, 2002b: On the secondary meridional circulation associated with the quasi-biennial oscillation. Tellus, 54B, 395–406.

Crooks, S. A., and L. J. Gray, 2005: Characterization of the 11-year solar signal using a multiple regression analysis of the ERA-40 dataset. J. Clim., 18, 996–1015.

Dee, D. P., S. M. Uppala, A. J. Simmons, P. Berrisford, P. Poli, S. Kobayashi, U. Andrae, M. A. Balmaseda, G. Balsamo, P. Bauer, P. Bechtold, A. C. M. Beljaars, L. van de Berg, J. Bidlot, N. Bormann, C. Delsol, R. Dragani, M. Fuentes, A. J. Geer, L. Haimberger, S. B. Healy, H. Hersbach, E. V. Hólm, L. Isaksen, P. Kållberg, M. Köhler, M. Matricardi, A. P. McNally, B. M. Monge-Sanz, J.-J. Morcrette, B.-K. Park, C. Peubey, P. de Rosnay, C. Tavolato, J.-N. Thépaut, and F. Vitart, 2011: The ERA-Interim reanalysis: Configuration and performance of the data assimilation system. Quart. J. Roy. Meteor. Soc., 137, 553–597.

Dunkerton, T. J., and M. P. Baldwin, 1991: Quasi-biennial modulation of planetary-wave fluxes in the northern hemisphere winter. J. Atmos. Sci., 48, 1043–1061.

Edmon, H. J., B. J. Hoskins, and M. E. McIntyre, 1980: Eliassen–Palm cross-sections for the troposphere. J. Atmos. Sci., 37, 2600–2616.

Firth, S. M., N. A. Kramarova, R. S. Stolarski, R. D. McPeters, P. K. Bhartia, and G. J. Labow, 2014: Recent changes in total column ozone based on the SBUV Version 8.6 Merged Ozone Data Set. J. Geophys. Res., 119, 9735–9751.

Garfinkel, C. I., and D. L. Hartmann, 2007: Effects of the El Niño–Southern Oscillation and the Quasi-Biennial Oscillation on polar temperatures in the stratosphere. J. Geophys. Res., 112, D19112.

Garfinkel, C. I., T. A. Shaw, D. L. Hartmann, and D. W. Waugh, 2012: Does the Holton–Tan mechanism explain how the quasi-biennial oscillation modulates the Arctic polar vortex? J. Atmos. Sci., 69, 1713–1733.

Glaccum, W., R. L. Lucke, R. M. Bevilacqua, E. P. Shettle, J. S. Hornstein, D. T. Chen, J. D. Lumpe, S. S. Krigman, D. J. Debrestian, M. D. Fromm, F. Dalaudier, E. Chassefière, C. Deniel, C. E. Randall, D. W. Rusch, J. J. Olivero, C. Brogniez, J. Lenoble, and R. Kremer, 1996: The Polar Ozone and Aerosol Measurement instrument. J. Geophys. Res., 101, 14479–14487.

Gray, L. J., S. J. Phipps, T. J. Dunkerton, M. P. Baldwin, E. F. Drysdale, and M. R. Allen, 2001: A data study of the influence of the equatorial upper stratosphere on northern-hemisphere stratospheric sudden warmings. Quart. J. Roy. Meteor. Soc., 127, 1985–2003.

Gray, L. J., 2003: The influence of the equatorial upper stratosphere on stratospheric sudden warmings. Geophys. Res. Lett., 30, 1166.

Hansen, F., K. Matthes, and L. J. Gray, 2013: Sensitivity of stratospheric dynamics and chemistry to QBO nudging width in the chemistry-climate model WACCM. J. Geophys. Res., 118, 10,464–10,474.

Harada, Y., A. Goto, H. Hasegawa, N. Fujikawa, H. Naoe, and T. Hirooka, 2010: A major stratospheric sudden warming event in January 2009. J. Atmos. Sci., 67, 2052–2069.

Hardiman, S. C., N. Butchart, A. J. Charlton-Perez, T. A. Shaw, H. Akiyoshi, A. Baumgaertner, S. Bekki, P. Braesicke, M. Chipperfield, M. Dameris, R. R. Garcia, M. Michou, S. Pawson, E. Rozanov, and K. Shibata, 2011: Improved predictability of the troposphere using stratospheric final warmings. J. Geophys. Res., 116, D18113.

Hartmann, D. L., L. E. Heidt, M. Loewenstein, J. R. Podelske, J. Vedder, W. L. Starr, and S. E. Strahan, 1989: Transport into the south polar vortex in early spring. J. Geophys. Res., 94, 16779–16795.

Haynes, P., and E. Shuckburgh, 2000: Effective diffusivity as a diagnostic of atmospheric transport 1. Stratosphere. J. Geophys. Res., 105, 22777–22794.

Holton, J. R., and J. Austin, 1991: The influence of the equatorial QBO on sudden stratospheric warmings. J. Atmos. Sci., 48, 607–618.

Holton, J. R., and H.-C. Tan, 1980: The influence of the equatorial quasi-biennial oscillation on the global circulation at 50 mb. J. Atmos. Sci., 37, 2200–2208.

Hu, J., R. Ren, and H. Xu, 2014: Occurrence of winter stratospheric sudden warming events and the seasonal timing of spring stratospheric final warming. J. Atmos. Sci., 71, 2319–2334.

Karpetchko, A., E. Kyrö, and B. M. Knudsen, 2005: Arctic and Antarctic polar vortices 1957–2002 as seen from the ERA-40 reanalyses. J. Geophys. Res., 110, D21109.

Lait, L. R., 1994: An alternative form for potential vorticity. J. Atmos. Sci., 51, 1754–1759.

Langematz, U., and M. Kunze, 2006: An update on dynamical changes in the Arctic and Antarctic stratospheric polar vortices. Climate Dyn., 27, 647–660.

Lee, H., 1999: The interannual variation of the stratospheric dynamic fields in the northern hemisphere in spring. Ph.D. Thesis, Seoul National University, 241 pp.

Lu, H., T. J. Bracegirdle, T. Phillips, A. Bushell, and L. Gray, 2014: Mechanisms for the Holton-Tan relationship and its decadal variation. J. Geophys. Res., 119, 2811–2830.

Lucke, R. L., D. R. Korwan, R. M. Bevilacqua, J. S. Hornstein, E. P. Shettle, D. T. Chen, M. Daehler, J. D. Lumpe, M. D. Fromm, D. Debrestian, B. Neff, M. Squire, G. König-Langlo, and J. Davies, 1999: The Polar Ozone and Aerosol Measurement (POAM) III instrument and early validation results. J. Geophys. Res., 104, 18785–18799.

Manney, G. L., R. W. Zurek, M. E. Gelman, A. J. Miller, and R. Nagatani, 1994: The anomalous Arctic lower stratospheric polar vortex of 1992–

1993. Geophys. Res. Lett., 21, 2405–2408.

Manney, G. L., and J. L. Sabutis, 2000: Development of the polar vortex in the 1999-2000 Arctic winter stratosphere. Geophys. Res. Lett., 27, 2589–2592.

Marsh, D. R., M. J. Mills, D. E. Kinnison, J.-F. Lamarque, N. Calvo, and L. M. Polvani, 2013: Climate change from 1850 to 2005 simulated in CESM1(WACCM). J. Clim., 26, 7372–7391.

Marlton, G., A. Charlton-Perez, G. Harrison, I. Polichtchouk, A. Hauchecorne, P. Keckhut, R. Wing, T. Leblanc, and W. Steinbrecht, 2021: Using a network of temperature lidars to identify temperature biases in the upper stratosphere in ECMWF reanalyses. Atmos. Chem. Phys., 21, 6079–6092.

Nakamura, N., and J. Ma, 1997: Modified Lagrangian-mean diagnostics of the stratospheric polar vortices: 2. Nitrous oxide and seasonal barrier migration in the cryogenic limb array etalon spectrometer and SKYHI general circulation model. J. Geophys. Res., 102, 25721–25735.

Naoe, H., and K. Shibata, 2010: Equatorial quasi-biennial oscillation influence on northern winter extratropical circulation. J. Geophys. Res., 115, D19102.

Nash, E. R., P. A. Newman, J. E. Rosenfield, and M. R. Schoeberl, 1996: An objective determination of the polar vortex using Ertel's potential vorticity. J. Geophys. Res., 101, 9471–9478.

Nath, D., W. Chen, C. Zelin, A. I. Pogoreltsev, and K. Wei, 2016: Dynamics of 2013 Sudden Stratospheric Warming event and its impact on cold weather over Eurasia: Role of planetary wave reflection. Sci. Rep., 6, 24174.

Naujokat, B., 1986: An update of the observed quasi-biennial oscillation of the stratospheric winds over the tropics. J. Atmos. Sci., 43, 1873–1877.

Neal, R. B., J. Richter, S. Park, P. H. Lauritzen, S. J. Vavrus, P. J. Rasch, and M. Zhang, 2013: The mean climate of the Community Atmosphere Model (CAM4) in forced SST and fully coupled experiments. J. Clim., 26, 5150–5168.

Neu, J. L., L. C. Sparling, and R. A. Plumb, 2003: Variability of the subtropical “edges” in the stratosphere. J. Geophys. Res., 108, 4482.

O’Sullivan, D., and R. E. Young, 1992: Modeling the quasi-biennial oscillation’s effect on the winter stratospheric circulation. J. Atmos. Sci., 49, 2437–2448.

Plumb, R. A., and R. C. Bell, 1982: A model of the quasi-biennial oscillation on an equatorial beta-plane. Quart. J. Roy. Meteor. Soc., 108, 335–352.

Plumb, R. A., 2010: Planetary waves and extratropical winter stratosphere. The Stratosphere: Dynamics, Transport, and Chemistry, Geophysical Monograph Series, Polvani, L. M., Sobel, A. H., Waugh, D. W. (eds.), Wiley, Hoboken, NJ, USA, 23–42.

Polvani, L. M., D. W. Waugh, and R. A. Plumb, 1995: On the subtropical edge of the stratospheric surf zone. J. Atmos. Sci., 52, 1288–1309.

Rao, J., C. I. Garfinkel, and I. P. White, 2021: Development of the extratropical response to the stratospheric quasi-biennial oscillation. J. Clim., 34, 7239–7255.

Ruzmaikin, A., J. Feynman, X. Jiang, Y. L. Yung, 2005: Extratropical signature of the quasi-biennial oscillation. J. Geophys. Res., 110, D11111.

Sasano, Y., M. Suzuki, T. Yokota, and H. Kanzawa, 1999: Improved Limb Atmospheric Spectrometer (ILAS) for stratospheric ozone layer measurements by solar occultation technique. Geophys. Res. Lett., 26, 197–200.

Schoeberl, M. R., L. R. Lait, P. A. Newman, and J. E. Rosenfield, 1992: The structure of the polar vortex. J. Geophys. Res., 97, 7859–7882.

Smith, A. K., J. C. Gille, L. V. Lyjak, 1984: Wave-wave interaction in the stratosphere: Observations during quiet and active wintertime periods. J. Atmos. Sci., 41, 363–373.

Smith, K. L., R. R. Neely, D. R. Marsh, and L. M. Polvani, 2014: The Specified Chemistry Whole Atmosphere Community Climate Model (SC-WACCM). J. Adv. Model. Earth Syst., 6, 883–901.

Solomon, S., 1999: Stratospheric ozone depletion: A review of concepts and history. Rev. Geophys., 37, 275–316.

Thompson, D. W. J., M. P. Baldwin, and J. M. Wallace, 2002: Stratospheric connection to Northern Hemisphere wintertime weather: Implications for prediction. J. Clim., 15, 1421–1428.

Wang, T., Q. Zhang, A. Hannachi, Y. Lin, and T. Hirooka, 2019: On the dynamics of the spring seasonal transition in the two hemispheric high-latitude stratosphere. Tellus, 71, 1634949.

Watson, P. A. G., and L. J. Gray, 2014: How does the quasi-biennial oscillation affect the stratospheric polar vortex? J. Atmos. Sci., 71, 391–409.

Waugh, D. W., and W. J. Randel, 1999: Climatology of Arctic and Antarctic polar vortices using elliptical diagnostics. J. Atmos. Sci., 56, 1594–1613.

Waugh, D. W., W. J. Randel, S. Pawson, P. A. Newman, and E. R. Nash, 1999: Persistence of the lower stratospheric polar vortices. J. Geophys. Res., 104, 27191–27201.

Waugh, D. W., and L. M. Polvani, 2010: Stratospheric polar vortices. The Stratosphere: Dynamics, Transport, and Chemistry, Geophysical Monograph Series, Polvani, L. M., Sobel, A. H., Waugh, D. W. (eds.), Wiley, Hoboken, NJ, USA, 43–57.

Wei, K., W. Chen, and R. Huang, 2007: Association of tropical Pacific sea surface temperatures with the stratospheric Holton-Tan Oscillation in the Northern Hemisphere winter. Geophys. Res. Lett., 34, L16814.

Yamashita, Y., H. Akiyoshi, and M. Takahashi, 2011: Dynamical response in the Northern Hemisphere midlatitude and high-latitude winter to the QBO simulated by CCSR/NIES CCM. J. Geophys. Res., 116, D06118.

Yokota, T., H. Nakajima, T. Sugita, H. Tsubaki, Y. Itou, M. Kaji, M. Suzuki, H. Kanzawa, J. H. Park, and Y. Sasano, 2002: Improved Limb Atmospheric Spectrometer (ILAS) data retrieval algorithm for version 5.20 gas profile products. J. Geophys. Res., 107, 8216.

Zambri, B., S. Solomon, D. W. J. Thompson, and Q. Fu, 2021: Emergence of Southern Hemisphere stratospheric circulation changes in response to ozone recovery. Nat. Geosci., 14, 638–644.

국문초록

극와동과 행성파는 대규모순환, 미량기체의 분포 및 오존감소, 성층권-대류권 상호작용에 영향을 미치는 겨울철 성층권의 대표적인 역학적 현상이다. 본 연구에서는 1979년부터 2018년까지의 ERA-Interim 재분석 자료를 이용해 북반구 봄철 계절변화 시기의 극와동과 행성파의 변화 및 경년변동을 분석하였다.

북반구의 겨울에서 봄으로의 전환기의 극와동 및 극와동 붕괴에 대한 기존의 진단법들은 주로 하부성층권 극와동의 특성에 기반한 와도 또는 동서풍속의 특정 임계값을 사용하여, 극와동의 변화 양상이 복잡하고 동서풍속이 훨씬 큰 상부성층권에는 적용하기 어려웠다. 본 연구에서는 극와동의 생성 및 붕괴 시기를 미리 정의한 특정 임계값을 사용하지 않고, 극와동의 경계에서의 상당위도, 와도, 동서풍속의 시간변화율의 평균인 “edge-change” 메트릭의 변동을 통해 정의하였다.

새 진단법을 적용하여, 성층권 전체에 대한 극와동의 형성 및 붕괴 시기를 구하고, 이를 최종승온과 비교하였다. 새로운 진단법이 극와동 경계에서의 미량기체 수송 양상과 일치하는지 확인하기 위해 극와동의 생성 및 붕괴 시기를 미량기체 혼합비의 동서표준편차와 비교한 결과, 새로 정의된 극와동 붕괴 시기가 성층권 미량기체 혼합비의 변화와 잘 일치함을 확인하였다. 이러한 관찰로부터, 극와동 생성 및 붕괴에 대한 새 진단법은 하부성층권과 상부성층권을 포함한 성층권 전체에 적용 가능한 것으로 보인다.

북반구 봄철 성층권 행성파의 경년변동 측면에서 3월 상부성층권의 행성파 발달을 조사한 결과, 3 hPa의 파수 1 행성파는 그 진폭이 큰 해들 중 적도 성층권 준2년주기진동 위상이 10 hPa에서 동풍인 경우 서풍인 경우에 비해 유의미하게 큰 진폭이 나타났다. 준2년주기진동의 위상이 동풍이었던 1994년 3월과 서풍이었던 1995년 3월에 대해 실시한 파수 1 행성파 발달 사례연구에서, 1994년 3월 사례에는

중위도의 섭동이 북동쪽으로 빠르게 이동하여 발달하여 고위도의 파동을 대체하였다. 행성파 발달 초기단계에서 아열대의 동서평균운동에너지의 에디운동에너지로의 변환이 중위도 섭동의 발달에 있어 중요하며, 이러한 에너지변환은 중위도의 음의 동서풍 남북경도와 관련이 있다. 음의 동서풍 남북경도는 준2년주기진동에 의한 자오면 2차순환에 의해 생성된다. 중위도로부터 발달하기 시작한 섭동은 잠재와도속에 의해 수일에 걸쳐 북동쪽으로 이동하며 고위도 행성파의 성장을 더욱 강화시킨다.

합성분석은 1994년 3월의 파수 1 행성파 성장의 역학적 특성이 준2년주기진동의 동풍인 해들의 3월에 공통적으로 나타남을 보여주며, 음의 동서풍 남북경도가 고위도 파수 1 행성파의 발달에 중요함을 보여준다. 준2년주기진동의 적도 동서풍 프로파일에 따른 행성파의 역학적 반응을 대기대순환모형을 통해 조사한 결과, 4월에 준2년주기진동의 동풍 프로파일을 이용한 실험의 파수 1 행성파의 진폭이 서풍 프로파일을 이용한 실험에 비해 유의미하게 컸으며, 행성파의 발달 패턴 역시 재분석자료의 3월 패턴과 유사하였다. 이는 대기대순환모형의 겨울이 관측에 비해 더 길고 추운 것에 기인한 것으로 보인다. 본 연구는 행성파의 연직전파가 상대적으로 약한 계절전환기의 행성파 발달에 있어 적도성층권 준2년주기진동과 관련된 내부역학의 중요한 역할을 시사한다.

주요어: 북반구 봄철 성층권, 극와동 진단, 행성파 발달, 준2년주기진동, 에디운동에너지, 자오면 2차순환

학 번: 2008-20403